VISUALIZATION AND QUANTIFICATION OF HYDRODYNAMICS AND DOSE IN UV REACTORS BY 3D LASER-INDUCED FLUORESCENCE

A Dissertation
Presented to
The Academic Faculty

By

VARUN GANDHI

In Partial Fulfillment
of the Requirements for the Degree
of Doctor of Philosophy in Environmental Engineering in the
School of Civil and Environmental Engineering

Georgia Institute of Technology

December 2012

VISUALIZATION AND QUANTIFICATION OF HYDRODYNAMICS AND DOSE IN UV REACTORS BY 3D LASER-INDUCED FLUORESCENCE

Approved by:

Dr. Jae-Hong Kim, Advisor
School of Civil and Environmental Engineering
Georgia Institute of Technology

Dr. Spyros Pavlostathis
School of Civil and Environmental Engineering
Georgia Institute of Technology

Dr. Philip J. Roberts
School of Civil and Environmental Engineering
Georgia Institute of Technology

Dr. Minami Yoda
School of Mechanical Engineering
Georgia Institute of Technology

Dr. Thorsten Stoesser
School of Civil and Environmental Engineering
Georgia Institute of Technology

Dr. Karl Linden
School of Civil and Environmental Engineering
University of Colorado at Boulder

Date Approved: August 2, 2012

To my beloved parents:

NITIN AND MILAN GANDHI

without whom I would not be here

and…

ACKNOWLEDGEMENTS

I am very grateful to all members of Ph.D. committee, Dr. Jaehong Kim, Dr. Philip J. W. Roberts, Dr. Thorsten Stoesser, Dr. Spyros Pavlosthathis, Dr. Karl Linden and Dr. Minami Yoda for their support and advice throughout this research. I would like to extend my special gratitude to Dr. Jaehong Kim, my advisor, for all his effort to help me succeed both academically and personally. He has been the best advisor one could ask for and has always been there in terms of emotional support through my hard times. His infinite wisdom, positive attitude, unparalleled advice and understanding nature have provided me with tremendous faith and courage. I would like to thank Dr. Philip J. W. Roberts and Dr. Thorsten Stoesser for their help in bouncing off ideas and supporting my research.

I thank colleagues who contributed to this work: Dr. Min Cho, Dr. Dooil Kim, Dr. Duncan Bryant, Dr. Scott Socolofsky, Harold Wright, Andy Udell and Zachariah Worley. I especially would like to thank Dr. Min Cho, who with his great thirst for knowledge helped me start my research career on the right path, Dr. Dooil Kim who guided me into 3DLIF and Dr. Duncan Bryant who spent his valuable time teaching research and data analysis skills.

I would also like to thank colleagues in my research group, Dr. Hyung Hoon, Dr. Jae-Sang Lee, Dr. Lokesh Padhye, Seung-Jin Lee, Dr. Dongjin Kim, the current members of

the Kim research group and faculty and peers in Environmental Engineering at Georgia Institute of Technology. I specially thank Dr. Ozeair Abessi, who in the past 5 months has been more of an older brother, bringing about a calming influence with all the "turbulence" in my life and spending special moments with me. I would like to acknowledge all the amazing friends I have made over the years in Atlanta; however, I would like to specially mention my close friends, Pritesh Patel, Vineet Jain and Nirmal Sahadev for always being available to share my sorrows and spread laughter.

Greatest thanks go to my family. I am also greatly indebted to my parents, my mother, Milan Gandhi, and my father, Nitin Gandhi, my brother, Chirag Gandhi and sister-in law, Paridhi Badjatiya Gandhi. I would not have become what I am today without their unconditional love and sacrifice. Lastly, I would like to thank my uncle, Girish Patel and his family for their support and love when we first moved to the U.S.

This research was partially funded by Water Research Foundation; K-water, Korea Water Resources Corporation and Carollo Engineers.

TABLE OF CONTENTS

LIST OF TABLES

LIST OF FIGURES

LIST OF ABBREVIATIONS

2D	Two-dimensional
3D	Three-dimensional
3DLIF	Three-dimensional laser induced fluorescence
AOP	Advanced oxidation process
B. subtilis	*Bacillus subtilis*
CCD	Charge coupled device
CFD	Computational fluid dynamics
COV	Coefficient of variation
C. parvum	*Cryptosporidium parvum*
DBP	Disinfection by-product
DNA	Deoxyribonucleic acid
LDV	Laser doppler velocimetry
LES	Large eddy simulation
LIF	Laser-induced fluorescence
LP	Low-pressure
LPHO	Low-pressure high-output
LSI	Line source integration
MP	Medium-pressure
MPSS	Multiple point source summation
MSSS	Multi-segment source summation
NOM	Natural organic matter

POD	Proper orthogonal decomposition
PIV	Particle image velocimetry
PLIF	Planar laser-induced fluorescence
R6G	Rhodamine 6G
RANS	Reynolds-Averaged Navier Stokes equations
RED	Reduction equivalent dose
RNA	Ribonucleic acid
RTD	Residence time distribution
THM	trihalomethane
TR-PIV	Time-resolved PIV
USEPA	United States Environmental Protection Agency
UV	Ultraviolet
UVT	ultraviolet transmittance
WaterRF	Water Research Foundation

LIST OF SYMBOLS

a = angle between UV lamp normal and line from the point source to location of interest

a_w = attenuation coefficient of water

a_i = expansion coefficients for each mode i

A_n^i = nth component of the eigenvector corresponding to the ith eigenvalue λ_i

Av = Avogadro's number, 6.023×10^{23} [photons/einstein]

C = concentration of Rhodamine 6G [M L^{-3}]

c = speed of light, 3×10^8 [L T^{-1}]

d_1 = path length through air [L]

d_2 = path length through the quartz sleeve [L]

d_3 = path length through water [L]

D = diameter of cylinder [L]

E_λ = radiant energy at a given wavelength λ_w [kJ/einstein]

E = irradiances with absorption [mW/cm^2]

E_0 = irradiances without absorption [mW/cm^2]

f = vortex shedding frequency [T^{-1}]

Focus = represents the concentrating effect caused by refraction [dimensionless]

h = Planck's constant, 6.626×10^{-34} [J·s]

I_A = fluence rate at point A [mW/cm^2]

I = UV-fluence rate [mW/cm^2]

$I(r)$ = lamp intensity at point located at distance r away from the lamp [mW/cm^2]

$I_b(i,k)$ = pixels of black images at the i_{th} and j_{th} pixel indices [dimensionless]

$I_c(i,k)$ = pixels of corrected images at the i_{th} and j_{th} pixel indices [dimensionless]

$I_{cc}(i,k)$ = corrected pixel value at the i_{th} and j_{th} pixel indices [dimensionless]

$I_r(i,k)$ = pixels of raw images at the i_{th} and j_{th} pixel indices [dimensionless]

$I_s(i,k)$ = pixels of standard white images at the i_{th} and j_{th} pixel indices [dimensionless]

IT = product of UV intensity and contact time [mJ/cm^2]

K = average pixel value of the standard white image [dimensionless]

k = inactivation rate constant [cm^2/mJ]

l = arc length of the UV lamp [L]

L = characteristic length [L]

n = number of points lamp is modeled as [dimensionless]

n_1 or n_2 = refractive indices of two different media [dimensionless]

n_q = refractive index for quartz [dimensionless]

n_w = refractive index for water [dimensionless]

N = organism concentration after UV exposure at respective times t [PFU/mL]

N_0 = initial organism concentration [PFU/mL]

P_i = Laser intensity at x [mJ/cm^2]

P = Power output from the UV lamp [W]

P_0 = Laser intensity at x_0 [mW/cm^2]

R = Reflectance Factors [dimensionless]

Re = Reynolds number [dimensionless]

St = Strouhal number [dimensionless]

t = exposure time [T]

T = thickness of UV lamp sleeve [L]

T_w = 10 mm path length transmittance of water [dimensionless]

T_q = 10 mm path length transmittance of quartz [dimensionless]

u = velocity in the x-direction [L T^{-1}]

U = attenuation factor due to absorption

UV_{abs} = UV absorbance of the water [dimensionless]

W = characteristic length [L]

v = velocity in the y-direction [L T^{-1}]

Δx = distance between two pixels [L]

$\alpha(\lambda)$ = napierian absorption coefficient at wavelength λ

λ = eigenvalue [dimensionless]

λ_w = wavelength [L]

θ_1 = refraction angle at the air-quartz interface

ϕ^i = POD modes [dimensionless]

σ = standard deviation [L T^{-3}]

ν = kinematic viscosity [L^2T^{-1}]

SUMMARY

A novel technique for the spatial and temporal assessment of the hydrodynamics and the UV dose delivered and the link between these two factors in a lab-scale UV reactor using three dimensional laser induced fluorescence (3DLIF) is developed in this study. This tool can also be utilized for the optimization of UV reactors and to provide data for validation of CFD-based simulation techniques.

3DLIF allows real time characterization of mixing conditions in a small-scale UV disinfection reactor by capturing fluorescence images emitted from a laser dye, Rhodamine 6G, using a high speed CCD camera. The 3DLIF system analyzed the hydrodynamics and dose delivery in a single lamp UV reactor placed perpendicular to flow. In addition to three-dimensional mixing, the technique successfully visualized the two-dimensional, transient mixing behaviors and dose delivery within the reactor, which has not been possible with traditional tracer test techniques.

Conservative tracer tests revealed unsteady turbulent flow characteristics such as the recirculation zone and the von Karman vortex street that are normally observed in flows around cylinders. Paths above the cylinder center, characterized by higher velocities and less influence of the cylinder, were also analyzed. The results demonstrated that a major difference between the paths at and above the cylinder center was the decreasing amount of dye entering the recirculation zone, which has a higher residence time, as the injection height increased. The results also suggested that a longer approach length was beneficial

to increase the probability of microbes entering the region around the lamp sleeve irrespective of their entrance height into the reactor. This is especially important when elbows are placed upstream of the UV reactor. Lastly, the length of the outlet i.e., distance from the last lamp array to the reactor exit, was examined as mixing at the outlet was determined to drastically vary over time with an increase in injection height. A well-mixed outlet, i.e., when the concentration profile across the reactor height is within 10% as in the center injection case, would be desirable to improve the accuracy of the biodosimetry results. These inlet and outlet analyses were the first of its kind and aid in the optimization of the reactor design.

Furthermore, evaluating the performance of typical water treatment UV reactors is challenging due to the complexity in assessing spatial and temporal variation of UV fluence, resulting from highly unsteady, turbulent nature of flow and variation in UV intensity. Mapping the spatial and temporal fluence delivery and MS2 inactivation revealed the highest local fluence in the wake zone due to longer residence time and higher UV exposure while the lowest local fluence in a region near the walls due to short-circuiting flow and lower UV fluence rate. The location of tracer injection, varying the height and upstream distance from the lamp center, was found to significantly affect the UV fluence received by the tracer. A Lagrangian-based analysis was also employed to predict the fluence along specific paths of travel, which agreed with the experiments. The 3DLIF technique developed in this study provides new insight on dose delivery that fluctuates both spatially and temporally and is expected to aid design and optimization of

UV reactors as well as validate computational fluid dynamics models that are widely used to simulate UV reactor performances.

Finally, the correlation between the hydrodynamics and cumulative local fluence delivery in the reactor was determined using a technique called the proper orthogonal decomposition (POD). Since this method is mainly applied to velocity and vorticity fields, the decomposition of the spatial concentration data, obtained using laser-induced fluorescence (LIF), for the flow around a confined circular cylinder (Re = 4,900) was compared with their corresponding velocity and vorticity decompositions to validate the use of POD on concentration data. The velocity, vorticity and concentration modes identify the dominating coherent structures, i.e. shear layer roll-up, instantaneous recirculation and von Karman vortex shedding. In the velocity and vorticity decomposition, instantaneous recirculation and von Karman vortex shedding are represented in the highest energy modes, modes 1 and 2. However, in the concentration decomposition, mode 1 represents regions with strong concentration intermittency, i.e., where no dye was present in alternative cycles, while mode 2 represents the coherent structures, which are identified in modes 1 and 2 in the velocity and vorticity decomposition. The concentration based decomposition identifies the shear layer around the cylinder that was only partially captured by their vorticity counterpart. This validated decomposition method was then applied to the fluence results revealing similar coherent structures showing the dependency of fluence delivery on the reactor flow.

CHAPTER 1.
INTRODUCTION

1.1. Statement of the Problem

The application of UV light as a disinfectant has been gaining popularity (Ho et al., 1998) because it effectively inactivates pathogens such as *Cryptosporidium parvum* (*C. parvum*) oocyst (Abbaszadegan et al., 1997; Clancy et al., 1998; Dyksen et al., 1998; Huffman et al., 2000), a protozoan parasite that has shown strong resistance to common water disinfectants such as free chlorine and monochloramine (Gyürék *et al.*, 1997; Rennecker *et al.*, 2000; Driedger *et al.*, 2000, 2001a). In addition, due to the formation of trihalomethanes, bromates and other halogenated disinfection by-products (DBPs) during chemical disinfection, UV light has been identified as an effective alternative with much less concern on DBP formation (Bellar et al., 1974; Glaze et al., 1993; Oppenheimer et al., 1997). However, a spatial and temporal assessment of the UV dose delivered and the reactor performance has been severely limited for utilities practicing UV disinfection.

Biodosimetry (Qualls and Johnson 1983; Qualls et al., 1989), the widely used validation method, treats the UV reactor as a "black-box" and hence cannot account for the dependence of the dose delivery on the complex hydrodynamics and the spatial variation in UV intensity. Alternative methods such as fluorescent microspheres as non-biological surrogates (Bohrerova at al., 2005; Blatchley et al., 2006) and computational fluid dynamics (CFD) simulations (Elyasi and Taghipour, 2010; Sozzi and Taghipour, 2007; Sozzi and Taghipour, 2006; Elyasi and Taghipour, 2006; Lyn and Blatchley, 2005; Lyn et

al., 1999) have been developed. While the fluorescent microspheres predict the cumulative UV fluence each particle is exposed to, measures the UV dose distribution and provides reduction equivalent dose (RED) estimates for microbes with different inactivation kinetics, it does not provide spatial information on dose delivery within the reactor, similar to biodosimetry. On the other hand, CFD models provide spatial information, estimates of the dose distribution, and RED for different microorganisms through modeling of each process. However, these models have not been validated against experimental results for accuracy.

Development of proper reactor design would be ideally pursued through an understanding of the fluid behavior that determines how microorganisms accumulate UV dose as they spend varying amounts of time in regions of fluctuating light intensity (Lawryshyn et al., 2003). There have been a few published studies focused on improving the understanding of steady-state hydrodynamics in parallel to flow UV reactors experimentally using planar laser induced fluorescence (Elyasi and Taghipour, 2010; Elyasi and Taghipour, 2011). However, no such experimental work has been published on the most common type of reactor used in water treatment plants, a reactor with UV lamps placed perpendicular to flow. Mixing characteristics using residence time distributions (RTD) and velocity profiles in various regions of the reactor (Wols et al., 2010) was the closest attempt to experimentally examine this reactor configuration.

Furthermore, the turbulence and complexity in the flow, brought about by the placement of cylindrical UV lamps perpendicular to flow, leads to separation forming unsteady

large-scale vortices and consequently significant fluid mixing (Williamson, 1996; Zdravkovich, 1997). These so called von-Karman vortices (repeating pattern of alternating vortices produced downstream of a bluff body) compound the complexity and unsteadiness in the flow region behind the lamp, as they involve the interactions of three shear layers, i.e., a boundary layer around the sleeve, a separating free shear layer, and a highly turbulent wake (Williamson, 1996). The presence of multiple lamps in a staggered configuration further complicates the flow, rendering the prediction of unsteady hydrodynamics significantly difficult. Furthermore, inlet configuration (Sozzi et al., 2006), upstream pipe bends (Zhao et al., 2009), and the presence of modifications such as baffles (Blatchley et al., 1998; Wols et al., 2010a), rings (Janex et al., 1998), or "wave-like" walls (Chiu et al., 1999a) have been found to significantly affect the hydrodynamics and reactor performance.

Due to the complexity of the flow, computational fluid dynamics (CFD) has been increasingly used to model the hydrodynamics in UV reactors based on the time-averaged Reynolds Averaged Navier Stokes (RANS) approaches (Sozzi et al., 2006; Alpert et al., 2010; Wols et al., 2010b). However, the velocity distributions in the RANS simulations have been found to differ from the experimental results typically obtained using particle image velocimetry (PIV). Alpert et al. (2010) and Wols et al. (2010b) determined that RANS simulations under-predicted the flow complexity in dynamic wake regions and dead zones due to the poor capture of large vortices and turbulent motions. These studies concluded that resolving the unsteady turbulent motions is essential to provide an

accurate representation of the microorganism trajectories and more significantly the UV dose received by each microbe.

UV fluence (*IT*, mJ/cm^2), the product of the cumulative UV fluence rate (*I*, mW/cm^2) and its residence time (*T*, s) through the reactor, consists of both spatial and temporal components. Predicting the spatial variations of factors that determine UV reactor performance, namely the fluid mixing and the fluence rate, is complex, and, therefore, computational fluid dynamics (CFD), more commonly Reynolds-Averaged Navier-Stokes (RANS) using a standard k - ε turbulence model (Wols et al., 2011; Younis and Yang, 2010; Wols et al., 2010a; Santoro et al., 2010; Elyasi and Taghipour, 2010; Wols et al., 2010b; Alpert et al., 2010; Sozzi and Taghipour, 2006; Lyn and Blatchley, 2005; Lyn et al., 1999; Blatchley et al., 1998; Janex et al., 1998) have been widely employed to simulate hydrodynamics. Velocity fields obtained using particle image velocimetry (PIV) (Sozzi and Taghipour, 2006) and laser Doppler anemometry (LDA) (Wols et al., 2010b) have been used to calibrate RANS simulations. When coupled with models for UV intensity and microorganism inactivation, time-averaged fluence delivery and reactor performance can be predicted.

Temporal variation of fluence, which results from highly unsteady, turbulent nature of flow in typical UV reactors used for drinking water treatment, adds complexity to the prediction. Of particular concern is the occurrence of large-scale eddy structures called von Karman vortices downstream of the cylindrical UV lamp sleeves. It is well understood that temporal variation must be accounted for to accurately predict dose

delivery and hence microbial inactivation (Wols et al., 2010a; Wols et al., 2010b; Younis and Yang, 2011). For example, Younis and Yang (2011) found as much as 50% error in the residence time of particles released at various heights in a UV reactor where a lamp was placed perpendicular to the flow by comparing RANS simulations with standard and modified k - ε models. This error essentially carries over to the prediction of reactor performance. In addition, the velocity profile in the wake region between experiments and RANS simulations varied by more than 30%, measured by the root mean squared deviations, further emphasizing the importance of incorporating the unsteady turbulent motion to accurately predict reactor performance (Wols et al., 2010). Since temporal variations are not resolved using RANS models, a more sophisticated large-eddy simulation (LES) that takes into consideration the large turbulent eddies has been employed to provide fluence models (Wols et al., 2010; Younis and Yang, 2011). These results have yet to be validated against experimental data to ensure applicability to actual reactor design (Elyasi and Taghipour, 2010). Unfortunately, experimental studies that verify these temporal mixing and fluence fluctuations are severely limited.

Finally, the relationship between the hydrodynamics and the local cumulative fluence has not been studied. The existence of coherent structures in turbulent shear flows has been acknowledged in numerous publications devoted to revealing their mechanisms of generation and quantification of their effects on the turbulence statistics of the flow (Hussain, 1983; Robinson, 1991). Hussain (1986) describes a coherent structure as "a connected turbulent fluid mass with instantaneously phase-correlated vorticity over its spatial extent". Though the definition is straightforward, extraction of coherent structures

that lie amongst incoherent and smaller scale turbulent motions is often not. Proper orthogonal decomposition (POD) offers an effective method to isolate the dominant characteristics and events in turbulent flows from vast volumes of experimental data with relative ease (Berkooz et al., 1993). Using mathematical analysis, this statistical technique helps identify a set of modes that represent spatially averaged structures arranged in descending order of energy contribution to the flow. The structure of each mode is of particular interest; however, it should be noted that individual modes do not fully describe an eddy or an instantaneous event.

POD analyses, more often than not, use data from multi-point measurement techniques, the most common being particle image velocimetry (PIV). Since it was first introduced, POD based on the vector velocity field has been applied to a wide variety of flows such as in turbulent pipes (Bakewell and Lumley, 1967), in channels (Moin and Moser, 1989; Ball et al., 1991; Sirovich et al., 1990), turbulent jets in crossflow (Meyer et al., 2007), in the wake behind a square cylinder (Shi et al., 2010), and in an isolated circular cylinder (Venturi, 2006; Perrin et al., 2007; Feng et al., 2011) amongst others. POD analyses was also applied on the scalar vorticity field, calculated as the derivative of the velocity field, obtained for the flow around a backward-facing step (Kostas et al., 2005), a fully developed turbulent boundary layer in a flume (Gurka et al., 2006) and the wake of an isolated circular cylinder (Ma et al., 2000). In these studies, the authors mentioned that the POD analysis on vorticity captured the coherent structures with the added benefit of lower computational time and cost since there is only one component of vorticity as opposed to two velocity components (i.e. for planar PIV data). However, the schemes for

calculating vorticity lead to unpredictable errors as the accuracy is highly dependent on the mean spatial resolution of the velocity sampling and the precision of the velocity measurement (Ruan et al., 2001). .

POD analyses also have been applied on concentration data that was obtained using either planar laser induced fluorescence (PLIF) to study the turbulent flow and mixing in counter-flow type T-junctions (Hirota et al., 2008) or Mie scattering in a gas-turbine combustor (Gnirss and Tropea, 2008) to analyze mixing conditions. Concentration based POD facilitates the identification of coherent structures without information on the velocity field, which may not always be available. Concentration images can be captured in a myriad of situations such as field and lab experiments, flow in major water bodies like seas and oceans, satellite imagery of chlorophyll concentration, amongst others.

1.2. Research Objectives

The primary objective of this research is to develop a method to visualize and analyze the hydrodynamics and fluence delivery in UV reactors using the 3DLIF system and relate them to each other using a technique called proper orthogonal decomposition (POD). Previously, the 3DLIF system has been used to visualize the flow in ozone contactors and diffusers that discharge wastewater or brine into oceans, while the POD technique has previously been applied to reveal complex but coherent structures in a variety of turbulent flows. This thesis describes the LIF, POD and other quantification techniques used to analyze UV reactors and indicate areas of the reactor that require improvement.

More specific objectives of this study are:

1. Develop a LIF method to visualize the hydrodynamics in a lab-scale UV reactor with one lamp placed perpendicular to flow in real-time and in three dimensions (Chapter 3)
2. Visualize the turbulent structures such as recirculation zone and von Karman vortex shedding generated downstream of the UV lamp (Chapter 3)
3. Analyze multiple paths based on vertical height from the lamp center and determine a critical distance away from the lamp that causes short-circuiting (Chapter 3)
4. Identify regions (i.e. around the lamp and at the inlet and outlet) that require improvement to enhance reactor performance (Chapter 3)
5. Analyze the flow structures downstream of a cylinder using proper orthogonal decomposition (POD) of the velocity vectors, which is most commonly used in a POD analysis (Chapter 4)
6. Compare the POD analysis using velocity vectors, obtained using particle image velocimetry (PIV), and the tracer transport from LIF (Chapter 4)
7. Develop a LIF-based method to measure the fluence delivery in the lab-scale UV reactor (Chapter 5)
8. Visualize and quantitatively analyze the spatial and temporal distribution of dose delivery around and downstream of the lamp (Chapter 5)

9. Compare the coherent structures obtained from the concentration based decomposition on the instantaneous hydrodynamics with that of the fluence delivery downstream of the lamp (Chapter 5)
10. Quantitatively analyze path specific dose delivery within the lab-scale UV reactor to discern specific pathways that receive lower doses as the particles traverse through the reactor (Chapter 5)
11. Compare the path specific dose delivery from experiments with those obtained from a Lagrangian-based analysis using velocity vectors and an intensity model (Chapter 5)

CHAPTER 2.

BACKGROUND

2.1. ULTRAVIOLET DISINFECTION

2.1.1. Disinfection Methods

Disinfection is a process by which pathogenic microorganisms are inactivated or killed to provide safe water for drinking and thus prevent harmful diseases in humans. There are two common types of methods to achieve disinfection: (1) Chemical disinfection such as chlorine and ozone and (2) Physical disinfection such as pasteurization and ultraviolet (UV) disinfection. Historically, chemical disinfection methods have been effective in treating microorganisms, however, with the negative impacts of generating harmful disinfection by-products (DBPs) such as trihalomethanes (THMs) (Krasner et al., 2006; Krasner et al., 2009) and bromate (Kurokawa et al., 1983; Kurokawa et al., 1990; Ono et al., 1994).

Recently, UV disinfection has been increasingly used in water treatment (Ho et al., 1998) due to its cost effectiveness, small footprint and no addition of chemicals that can be difficult to transport. Compared to chemical disinfection, UV disinfection creates minimal DBPs (Oppenheimer et al., 1997; Sharpless and Linden, 2001) and is highly effective against most pathogens including protozoan parasites such as *Cryptosporidium parvum* (Abbaszadegan et al., 1997; Clancy et al., 1998; Dyksen et al., 1998; Huffman et

al., 2000) and *Giardia lamblia* (Campbell and Wallis, 2002; Linden et al., 2002) which have been of concern lately (Lisle and Rose, 1995; Craun et al., 1998; Hancock et al., 1998). However, UV disinfection has no chemical residual that is required to provide additional disinfection during transport of water in pipelines, the treatment effectiveness depends on water quality (Sommer et al., 1997; Janex et al., 1998; Batch et al., 2004) and accurately measuring the delivered dose is difficult (Qualls and Johnson, 1985; Qualls et al., 1989).

2.1.2. UV light as a Disinfectant

Ultraviolet (UV) light is the region in the electromagnetic spectrum that lie between wavelengths of 100 and 400 nm. This spectrum is divided into four regions: vacuum UV (100 – 200 nm), UV-C (200 – 280 nm), UV-B (280 – 315 nm) and UV-A (315 – 400 nm) (Meulemans, 1986). Primarily, UV disinfection occurs in the UV-C and UV-B regions due to the greater germicidal action on microorganisms, while the UV-A region has a comparatively negligible activity and the light in the vacuum region rapidly dissipates over short distances in water.

UV light is typically generated by applying a voltage across a gas mixture, resulting in a discharge of photons and consequently the emission of light. The wavelengths of light emitted depend on the elemental composition of the gas and the power level of the lamp. Most UV lamps currently employed in water treatment use a gas mixture containing mercury vapor since it emits light in the germicidal wavelength range.

Currently, water treatment facilities generally use low-pressure (LP), low-pressure high-output (LPHO) and medium-pressure (MP) lamps. In LP and LPHO lamps, mercury at low vapor pressures (10^{-4} psi and 10^{-5} – 10^{-4} psi, respectively) and moderate operating temperatures (40 °C and 60 – 100 °C, respectively) produce monochromatic UV light at 253.7 nm. In MP lamps, a higher vapor pressure (5.8 – 580 psi) and higher operating temperature (600 – 900 °C) is used to increase the collision frequency between mercury atoms, thus producing UV light over a broad spectrum between 200 and 300 nm with a higher intensity.

2.1.3. Advanced Oxidation Processes (AOPs)

The use of UV/H_2O_2 AOP is rapidly becoming an attractive alternative for the degradation of emerging contaminants such as acetaminophen and diclofenac (Snyder et al., 2007), endocrine disruptors such as bisphenol A, ethinyl estradiol and estradiol (Rosenfeldt and Linden, 2004) and taste and odor causing compounds (Rosenfeldt et al., 2005). In addition, UV/H_2O_2 AOP, followed by chlorine, has been shown to provide a synergistic effect in inactivating MS2 phage and *B. subtilis* spores (Cho et al., 2011). In this process, the contaminant oxidation occurs via a highly reactive intermediate, the hydroxyl radical (·OH) (Hunt and Taube, 1952; Baxendale and Wilson, 1957; Volman and Chen, 1959). When UV radiation is absorbed by H_2O_2, the molecule splits apart into two ·OH radicals as in reaction R1.

R1 $H_2O_2 + h\nu \rightarrow 2 \cdot OH$

The reaction mechanisms typically consist of a complex chain of fast chemical reactions. Once the hydroxyl radical is formed, it will rapidly undergo reactions non-selectively with water constituents including natural organic matter (NOM), organic compounds present and H_2O_2. The overall quantum yield (Φ_T) of hydrogen peroxide in the chain reaction is unity at the monochromatic UV wavelength of 254 nm (Crittenden et al., 1999).

2.1.4. Propagation of UV light

Similar to chemical disinfectants, like chlorine and ozone, that undergoes decomposition under certain conditions, the intensity of UV light changes depending on the materials it encounters. This occurs due to the absorption, refraction, reflection and scattering of light by the UV reactor components such as lamp envelopes, lamp sleeves and reactor walls and the water being treated. Absorption occurs when the energy of a photon is taken up by matter, causing the transformation of light to other forms of energy. When UV light is absorbed, it is no longer available for disinfection. The other phenomena, however, change the direction of UV light. Refraction occurs when the direction of the light changes due to propagation through the interface between two mediums with different refractive index such as air, quartz and water. Reflection occurs when light is deflected of a surface such as the reactor surface. Scattering occurs when light interacts with a particle present in the water being treated.

2.1.5. Mechanism of UV Disinfection

Approximately 85% of the output from low-pressure mercury arc lamps is monochromatic at a wavelength of 254 nm (Water Environment Federation, 1996). According to equation (2.1),

$$E_\lambda = \frac{hC}{\lambda_w} Av \tag{2.1}$$

where E_λ = radiant energy at a given wavelength λ_w, kJ/einstein

C = speed of light, 3×10^8 m/s

h = Planck's constant, 6.626×10^{-34} J·s

λ_w = wavelength, m

Av = Avogadro's number, 6.023×10^{23} photons/einstein.

Radiant energy at λ_w = 254 nm has 472 kJ/einstein. Since in a photochemical reaction, one einstein represents one "mole", 472 kJ/mole is greater than the bond energies of several important bonds in microbial systems. For example, the C-H bond is about 401 – 414 kJ/mole and the C-C bond is about 347 – 355 kJ/mole (March, 1985). In addition, protein and nucleic acids, which is responsible for defining metabolic functions and reproduction of life, effectively absorb UVC, thus damaging the genetic material and causing inactivation of microbes.

The two types of nucleic acids, Deoxyribonucleic acid (DNA) and Ribonucleic acid (RNA) consist of single- or double-stranded polymers comprising of four constituent bases known as purines and pyrimidines. When UVC radiation is absorbed by the pyrimidine bases, mainly thymine, dimerization, i.e. formation of a chemical bond, between adjacent pyrimidines occurs as shown in Figure 2.1 (Jagger, 1967). Pyrimidine dimer damage prevents the replication of microorganisms when the cell undergoes mitosis, thus rendering them ineffective in infecting the host. However, this damage does not prevent metabolic functions in the microorganism such as respiration (Jagger, 1967).

2.2. UV REACTOR

2.2.1. Configuration

UV reactors typically are classified as either open or closed channel. Open channel reactors are mainly used in wastewater treatment applications. On the other hand, drinking water treatment has used closed, high pressure reactors. These reactors can be divided into two groups based on the configuration of lamp as shown in Figure 2.2:

(a) Horizontal configuration (Figure 2.2a): Lamp is placed parallel to flow direction.

(b) Vertical configuration (Figure 2.2b): Lamp is placed perpendicular to flow direction and could be placed in a staggered configuration.

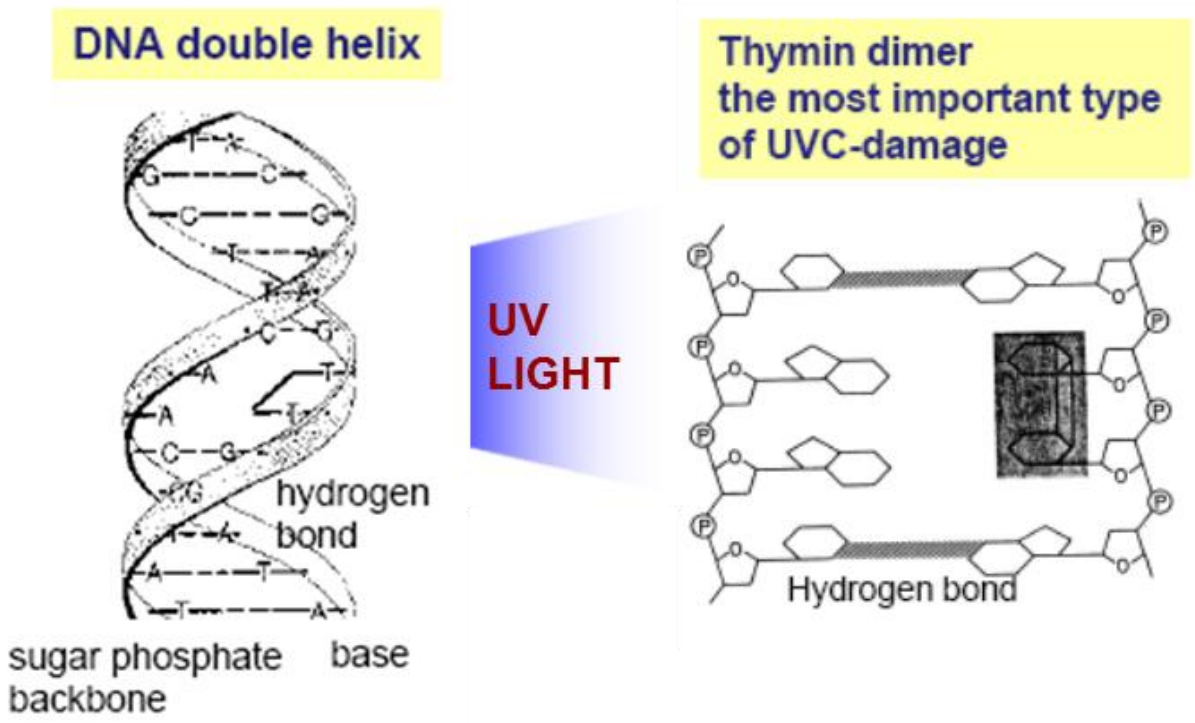

Figure 2.1: Formation of the thymin dimer, the most important type of UVC-damage, in the DNA double helix upon exposure to UV light

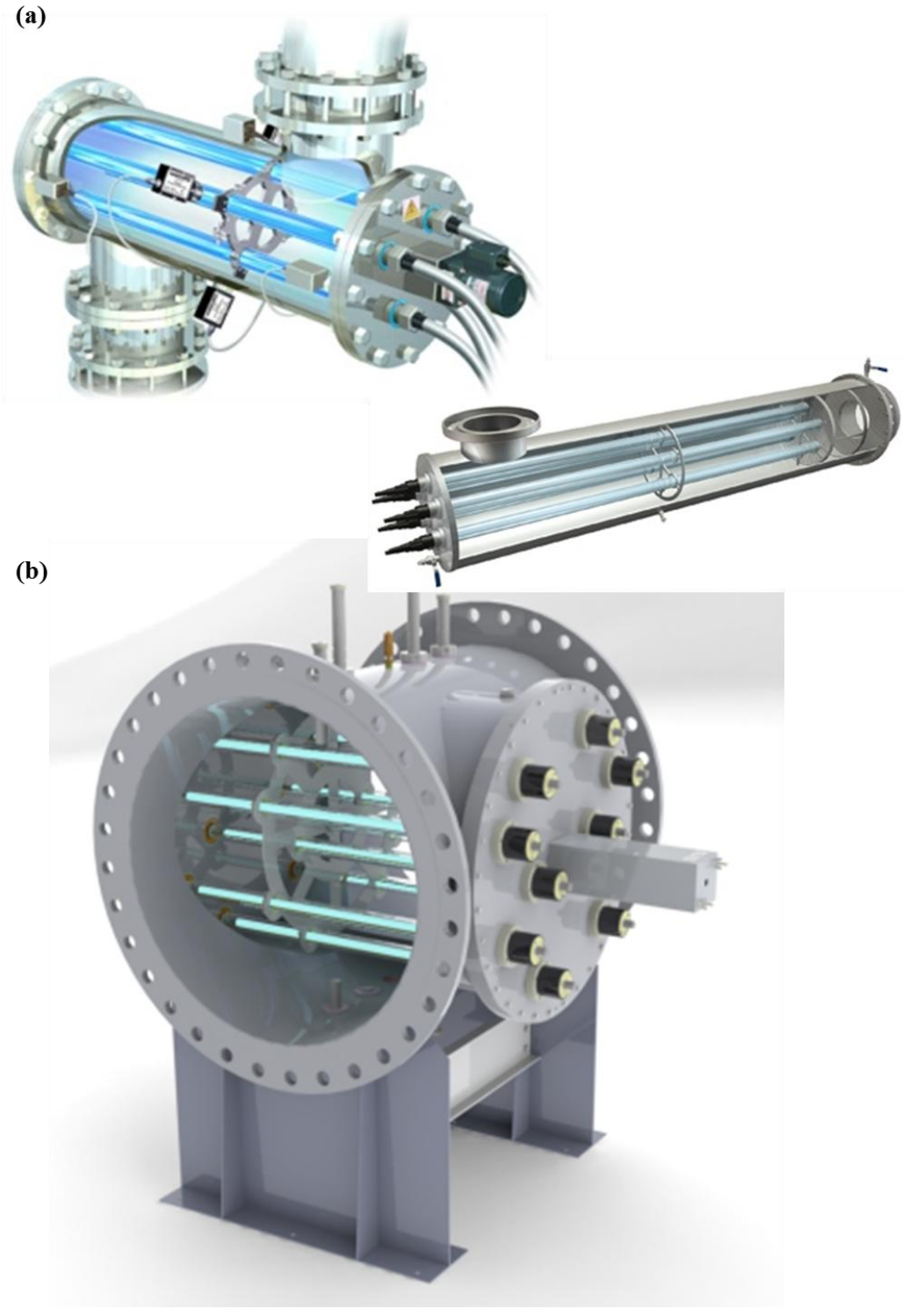

Figure 2.2: Configurations of the UV reactor (a) Horizontal, (b) Vertical

2.2.2. Reactor Validation

UV reactor validation is currently accomplished using the biodosimetry method (Qualls and Johnson, 1983; Qualls et al., 1989). Prior to a description of the method, a collimated beam reactor that is required in biodosimetry is introduced.

2.2.2.1. Collimated beam apparatus

A collimated beam apparatus is used to determine the dose response of a given microorganism that is spiked in water. The function of the apparatus is to direct the output of a UV lamp onto a horizontal surface using a long cylindrical tube known as the "collimator". This tube aids the incoming light to enter the batch reactor perpendicular to the water surface. The cell suspension is placed on the horizontal surface below the bottom of the collimator. Figure 2.3 depicts the collimated beam apparatus constructed in the laboratory that was used for batch scale experiments. The collimated beam apparatus was equipped with 15-W low-pressure mercury lamps (Philips Co., Amsterdam, Netherlands). This equipment produced parallel UV irradiation through a 60 × 50 cm long collimating tube placed below the UV lamps.

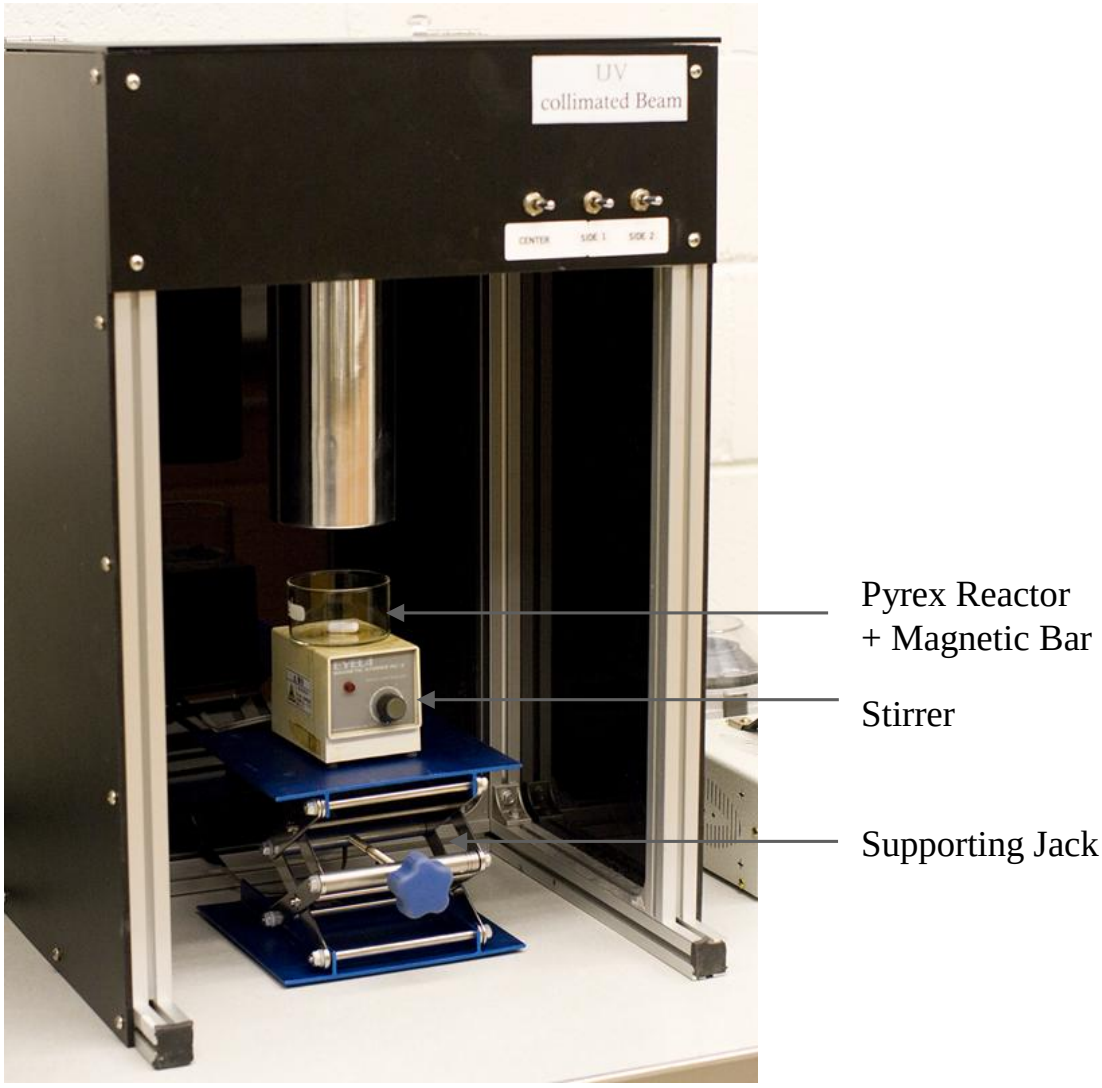

Figure 2.3: Collimated beam apparatus

2.2.2.2. Biodosimetry

This method requires two steps as follows:

Step 1a: Experimental tests using challenge microorganism:

In collimated beam bench scale tests, the UV dose-response relationship of the challenge microorganism, whose sensitivity to UV light is similar to the target pathogen, is characterized. In these experiments, UV light is directed down a collimated tube to dose a sample of challenge microorganisms of a known concentration. After a specified exposure time, the sample is analyzed to determine the log inactivation, i.e. the log of the ratio of concentration after UV light exposure with the concentration prior to UV exposure) as a function of UV dose. Testing at a variety of range of doses is performed to generate the UV dose-response curve.

Step 1b: Full-scale reactor testing:

The aforementioned challenge microorganisms are then injected upstream of the UV reactor. Samples at the outlet are analyzed to determine log inactivation changing a variety of conditions such as flow rates, UV transmittance (UVT) and lamp status.

Step 2: Estimate the Reduction Equivalent Dose (RED)

The results from Step 1a and 1b, i.e. the dose-response curve and the log inactivation in the full-scale reactor, respectively, are used to calculate the RED. The RED obtained are

always specific to the strain of challenge microorganism used during experimental testing and the range of conditions tested during the full-scale reactor tests.

The biodosimetry method has several limitations. First, it does not provide a direct measure of the UV dose distribution within the reactor. It is based on a "black box" approach whereby no information can be obtained on how the spatial relationship between hydrodynamics and UV intensity affects the delivered dose. This approach only provides an average dose for each set of flow conditions. However, microbes are exposed to a range of fluences depending on the path traveled (Chiu et al. 1999a, 1999b; Bohrerova et al., 2005; Lyn and Blatchley, 2005; Sozzi and Taghipour, 2006). Second, the non-pathogenic challenge microorganisms like MS-2 phage or *B. subtilis* spore, which are used in biodosimetry, are typically more resistant to the inactivation by UV light than the target microorganisms. The REDs of different microorganisms, either the target or the challenge, which have different microbial dose response curves, will not be the same (Wright and Lawryshyn, 2000). As a result, a RED bias factor has to be introduced to account for these issues (USEPA, 2006). Finally, biodosimetry is relatively expensive and does not provide real-time measurement of dose delivery, as the results are obtained 24 to 48 hours after microbiological assays (Linden and Darby, 1997).

2.2.3. Alternative Methods of Validation

In order to account for the shortcomings of biodosimetry, two alternative methods of reactor validation have been developed, namely fluorescent microspheres as non-biological surrogates (Bohrerova et al., 2005; Blatchley et al., 2006) and Computational Fluid Dynamics (CFD) (Lyn et al., 1999; Lyn and Blatchley, 2005). However, it should be pointed out that even though these methods are superior to biodosimetry using microbes, these methods are not currently in use.

2.2.3.1. Fluorescent microspheres as non-biological surrogates

Microspheres are spherical micro-particles that are similar in size (1 to 5 μm) and density characteristics to those of the target microorganisms; hence would have similar flow characteristics and dose exposures in reactors (Tang et al., 2005). Bohrerova et al. (2005) reported a method using polystyrene microspheres that are coated with a fluorescent dye. The fluorescence intensity of the dye reduces upon reaction with photons emitted from the UV lamp. The particle's fluorescence intensity is directly proportional to its dye content and inversely proportional to the UV fluence accumulated by the particle.

Another method developed by Blatchley et al. (2006) uses microspheres that contain a chemical actinometer, which are normally used for the measurement of radiation. The chemical actinometer employed in this study, (*E*)-5-[2-(methoxycarbonyl) ethenyl] cytidine is non-fluorescent and transforms to a bright violet fluorescent product (3-β-D-

ribofuranosyl-2,7-dioxopyrido[2,3-*d*]pyrimidine) when subjected to UV irradiation. The products' fluorescence intensity can be directly measured as it can be excited at 330 nm and emits photons at 385 nm. The extent of transformation is proportional to the dose of radiation delivered to the actinometer.

Hence, in flow-through UV reactors, the non-biological surrogates help to predict the cumulative UV fluence each particle is exposed to and thus can monitor the full distribution of doses that a pathogen may experience. In addition, non-biological surrogates can overcome issues related to different sensitivities of surrogate and target microorganisms thus providing RED estimates for microbes with different inactivation kinetics. However, this technique does not provide spatial or temporal information on dose delivery within the reactor; also a shortcoming of biodosimetry.

2.2.3.2. Computational Fluid Dynamics (CFD)

The other alternative method to biodosimetry is computational fluid dynamics (CFD) simulations, which models hydrodynamics using the Navier-Stokes equations (Versteeg and Malalasekera, 2007). Two types of simulations have been used to simulate the hydrodynamics in UV reactors namely: Reynolds-averaged Navier Stokes (RANS) and Large Eddy Simluations (LES). The RANS approach is based on a time average of the N-S equations and is therefore computationally inexpensive and requires less time. In RANS, the velocity and pressure, u_i and p, respectively, are averaged over time, so that the mean components $\overline{u}_i$ and $\overline{p}$ and the fluctuating components u_i' and p' describe the

flow. However, a closure problem still exists after simplifying to time-averaged equations. In order to overcome this problem, the Reynolds stress, τ_{ij}, has to be estimated using turbulence models, among which $k - \varepsilon$ turbulence model is the most popular.

However, limited results obtained with RANS models have led to an increased interest in Large Eddy Simulation (LES) as a tool to predict turbulent flows with unsteady structures. LES accounts for the larger, more energetic scales and uses a model for the small scales. According to Ferziger and Perić (2002), the objective of LES is to explicitly simulate large scale eddies, which are responsible for the majority of the momentum transport and turbulent diffusion. The smaller scale eddies are modeled by a sub-grid scale model. However, these models do not affect the results in LES significantly.

In order to numerically validate UV reactors, apart from flow simulations, UV intensity field models and microbial inactivation models have to be integrated. Various approaches have been developed to generate an UV intensity field map, such as multi-point source summation (MPSS, Jacob and Dranoff, 1970; Scheible et al., 1985; Suidan and Severin, 1986), line-source-integration (LSI) (Blatchley, 1997) and multi-segment source summation (MSSS) methods (Bolton, 2000). Section 2.2.5 describes these UV intensity models in further detail. The microbial inactivation model was integrated into the transport equation as the sink term. For example, the inactivation of MS2 bacteriophage was simulated using log-linear Chick-Watson kinetics whereas *Bacillus subtilis* was approximated with the series event model (Severin et al., 1983) due to the presence of a lag phase (Ducoste et al., 2005) further described in Section 2.2.6.

Even though CFD models (Lyn et al., 1999; Lyn and Blatchley, 2005; Sozzi and Taghipour, 2006; Elyasi and Taghipour, 2006; Sozzi and Taghipour, 2007) provide spatial dose delivery information, estimates of the dose distribution, and RED for different microorganisms, the experimental validation of the simulation accuracy has been severely limited. Lyn et al. (1999) compared the Eulerian approach with laboratory measurements of the flow field using laser Doppler velocimetry (LDV), a non-intrusive method to measure the mean flow and turbulence characteristics and concluded that good agreement was found between the model and experiments only upstream of the lamp region. Lyn and Blatchley (2005) reported that the Eulerian and Lagrangian approach underestimated the measured extent of disinfection by approximately 0.3 – 0.5 logs.

2.2.4. Hydrodynamics in UV reactors

The flow in UV reactors is highly turbulent with Reynolds number, *Re*, greater than 5000 typically observed in full-scale treatment plants. Due to the typically relatively brief contact time, the efficacy of practical UV systems depends strongly on the hydrodynamic transport processes that influence the spatial distribution of microorganisms (Lyn et al., 1999). The hydrodynamics in UV reactors mainly depend on the configuration of the lamp, placement of baffles and the inlet and outlet conditions.

2.2.4.1. Lamp configuration

A. Horizontal configuration

Systems with a lamp placed parallel to flow mainly exist as annular reactors, where the lamp axis is placed concentric to the reactor axis. In this type of reactor, mixing is caused by a shear layer along the surface of the lamps (Blatchley et al., 1995). A number of studies published have focused on simulating the flow in this reactor using RANS based CFD (Wols et al., 2011; Alpert et al., 2010; Santoro et al., 2010; Sozzi and Taghipour, 2007; Sozzi and Taghipour, 2006; Elyasi and Taghipour, 2006), one has compared the velocity field obtained from simulations with that obtained from experimental PIV measurements (Sozzi and Taghipour, 2006) and yet another study that compared steady-state experimental concentration degradation measurements with those obtained from CFD (Elyasi and Taghipour, 2010). Elyasi and Taghipour (2011), using planar laser-induced fluorescence (PLIF), experimentally observed the steady-state concentration and UV fluence profile for the first time while Sozzi and Taghipour (2005) experimentally compared velocity fields in annular reactors with inlets concentric (L-shaped) and normal (U-shaped).

The CFD simulations tended to under-predict the percent removal of a contaminant compared to corresponding pilot reactor trials, when incorporating AOPs as the oxidant (Alpert et al., 2010). Additionally, the authors observed that increasing flow rates caused an increase in the percent difference between pilot and CFD results (Alpert et al., 2010). Using PLIF, Elyasi and Taghipour (2010) compared steady-state concentration profiles between a model reactor and its corresponding CFD simulation. Overall, they determined close agreement between results. However, in some regions of the reactor such as a small zone at the end of the reactor and near the UV lamp, disagreement between the results was observed and was attributed to errors in the PLIF and numerical method (Elyasi and Taghipour, 2010). Finally, Elyasi and Taghipour (2011) determined the steady-state fluence in an annular reactor for the first time at various flow rates. They concluded that the method is a useful tool to provide information about the performance of the reactor and aid in optimizing it.

Generally, the simulation studies commonly used two modeling approaches: the Eulerian and the Lagrangian approach. In the Eulerian approach, a continuum model described by the advection-diffusion equation and the conservation equation of species is solved where the time-dependent flow of fluid entities in a specific location is of interest. On the other hand, in the Lagrangian approach, organisms are treated as discrete particles where the trajectory is predicted by integrating the force balance on the particle based on the velocity field. Effects of turbulence on each particle are accounted for by random walk described in Section 2.5. The fluence is determined from the time history of each particle as it traverses through the reactor.

Sozzi and Taghipour (2006) applied the Eulerian and Lagrangian methods to annular reactors with different inlets using RANS simulations. Even though the predicted inactivation between the approaches differed, the information obtained from each modeling technique is complimentary to the other. The Lagrangian method provides estimates of the UV dose distribution and particle tracks to visualize the flow patterns while the Eulerian method shows the concentration distribution and local reaction rates. Combining the information from the methods, predicting and monitoring reactor performance levels and enhancing reactor designs can be achieved.

B. Vertical configuration

This lamp configuration causes the formation of a vortex in the wake region of the cylinder. The two main characteristics of the flow around a cylinder: the recirculation region and the von Karman vortex shedding (Williamson, 1996; Zdravkovich, 1997). This phenomenon occurs when the presence of the sleeve creates a low pressure zone in the wake region, causing water, for example, from the top of the cylinder to rotate clockwise and fill up this region. At the next instant, a vortex on the opposite side of the lamp was formed which rotated counter-clockwise into the wake region that caused a release of the first vortex, hence vortex shedding occurred. Immediately, the

released vortex began to grow in size while simultaneously, a new vortex, on the same side of the cylinder, was created and the cycle continued (Zdravkovich, 1997). This phenomenon has been extensively studied in fluid mechanics as it has direct engineering significance. The fluctuating pressure forces in the transverse direction cause structural vibrations or resonance, which can trigger failure (Williamson, 1996).

The complex turbulent motion of the fluid results in a wide range of residence times inside the UV reactor as a result of the vortex shedding. Due to the complex nature of the flow in this configuration, CFD has been employed to simulate the hydrodynamics and serve as a powerful design tool. Numerous studies have investigated the flow around lamps placed perpendicular to flow using RANS-based CFD simulations (Younis and Yang, 2011; Wols et al., 2011; Younis and Yang, 2010; Santoro et al., 2010; Wols et al., 2010; Lyn and Blatchley, 2005; Lyn, 2004; Lyn et al., 1999; Janex et al., 1998) and LES-based simulations (Younis and Yang, 2011; Younis and Yang, 2010; Wols et al., 2010; Lyn, 2004).

Combining a UV intensity field and microorganism inactivation model with the steady-state RANS simulations, a prediction of the time-averaged dose distribution and log inactivation was achieved, upon comparing velocity profiles obtained from experiments and simulations. This prediction was compared with similar inactivation experimental results. Lyn et al., (1999) observed good agreement in the predictions of mean velocities and predictions of disinfection levels at higher flow rates, where the difference was less than 0.5 log units. However, at lower flow rates the differences were greater, 0.5 – 1.5 log units, thus an improvement was required.

Lyn and Blatchley (2005) applied the Eulerian and Lagrangian approaches described above in CFD simulations to analyze a UV reactor with 25 lamps in a staggered configuration. The continuum model results showed the importance of the wall region in determining performance of the reactor as relatively high viable microorganism concentration was observed extending to the outlet. From the Lagrangian results, a multimodal distribution, comprising of a main central mode and smaller modes at small doses, was found. The smaller doses corresponded to the microbes travelling along the wall of the reactor, thus the high concentrations along the sidewalls. These two methods were shown to complimentary to each other, however, the predictions of the extent of disinfection tended to be lower by about 0.5 log compared to measurements at a pilot scale facility.

Recently, a modified version of the standard k-ε model (Younis and Yang, 2010; Younis and Yang, 2011) and LES (Wols et al., 2010) has been applied to UV

disinfection reactors. Younis and Yang (2010, 2011) observed that the unsteady and complex flow played an important role in determining the efficiency of disinfection. The standard k - ε model, most commonly used in water treatment applications, fails to capture the strength of the vortex shedding and consequently the total residence time. The modified k-ε model (Younis et al., 2005) was shown to provide a substantial improvement in the prediction of the vortex shedding. In their reactor with four UV lamps placed in a diamond configuration, a Lagrangian analysis showed significant differences in dose estimation depending on whether the particles travelled the unsteady paths. The authors highlighted the importance of the vortex shedding phenomenon and its role on reactor performance.

Wols et al. (2010) applied RANS and LES to a reactor with a single lamp. Comparing velocity profiles from LES and RANS with PIV measurements, the flow fields were better described using the LES model. In the wake region downstream of the cylinder, the RANS model predicted the velocities to be positive, whereas a clear flow reversal

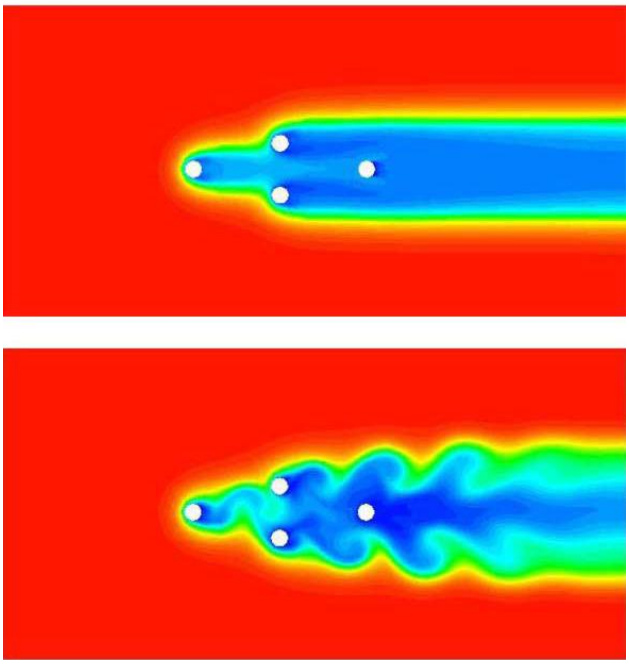

Figure 2.4. Standard RANS (above) vs. modified RANS (below) CFD simulation showing the turbulence in the flow downstream of the cylinder (Younis and Yang, 2010)

occurred in the measurements. The residence time distribution and dose distribution showed marked differences, related to the prediction of the wake region. The k-ε model predicted a small wake, whereas the LES model predicted a very large wake. The local geometry governs the effect of the flow on the disinfection efficacy.

In a reactor with a vertical configuration, experiments to determine the hydrodynamics and dose distribution are very limited. Wols et al., (2010a) performed an RTD analysis for a reactor with four lamps in a staggered configuration. The authors found that a dead zone exists along the walls of the circular reactor due to the long tail observed in the RTD. This confirms the low degree of lateral mixing occurring in UV reactors. Therefore, the measured hydraulic residence time will deviate from the theoretical time for low flow rates. At higher flow rates corresponding to the turbulent range, the concentrations were more uniformly spread over the cross-section.

2.2.4.2. Inlet condition

Inlet conditions can also drastically alter the flow within reactors. The configuration of the inlet determines the structure of the flow in the reactor. Sozzi and Taghipour (2005) used PIV, a non-intrusive measurement of the instantaneous planar velocities to track the movements of small tracer particles over time and to ultimately characterize the flow in annular reactors. The reactor consisted of a cylindrical body with a concentric lamp placed parallel to it. The flow was compared in two types of annular reactors differing in the inlet position: a U-shaped reactor where the inlet is perpendicular to the lamp axis and an L-shaped reactor where the inlet is parallel to the lamp axis.

In the L-shaped reactor, an expanding jet effect along with recirculation and lower velocity zones was found at the inlet region; however, the flow structures were more stable and hence better predictability over a range of flow rates as compared to the U-shaped reactor. In addition, the higher velocity zones coincided with areas of higher fluence rate (i.e. close to the lamp) in the L-shaped reactor, whereas the higher velocity zones overlapped with areas of lower fluence rate (i.e. close to the walls) in the U-shaped reactor. Hence, the L-shaped reactor was found to perform much better just based on its inlet position. From the results of this study, it was found that changes in the reactor geometry, such as rearrangement of the inlet position, has a significant impact on the local flow field, affecting the UV dose distribution as well as the reactor performance (Sozzi and Taghipour, 2005).

Moreira et al. (2007) further examined a reactor with three inlets placed perpendicular to the lamp axis and found that when operated simultaneously, they behaved like a plug flow with limited axial dispersion and was more efficient than a reactor with a single

perpendicular to lamp inlet. In addition, the reactor with three lateral inlets was found to have a lower percent stagnation zone than a reactor with one or two operational inlets. Zhao et al. (2009) compared three inlet configurations, A with a straight pipe placed perpendicular to an annular reactor, B and C with a U-shaped section rotated 90 degrees using fluorescent microspheres and CFD. They showed that configuration A shifted the peak of the dose distribution to higher values and increased the reduction equivalent dose (RED) predicted using microspheres. In addition, the velocity profile at the outlet and thus particle residence time was found to be varying drastically in each configuration.

2.2.4.3. Placement of baffles

Baffles are normally introduced into UV reactors to force the main flow to move closer to the lamp and increases mixing. Within any cross-section, the regions of highest velocity were coincident with the areas furthest from the boundary layers (i.e., areas adjacent to channel walls and lamp jackets) (Blatchley et al., 1998). These baffles are placed along the walls of the reactor to alter the short circuitous, high velocity path travelled by microbes therefore limiting the performance of the reactor. Cortelyou *et al.* (1954a) found an increase in disinfection efficiency in one unit as baffles were added to increase mixing across intensity gradients. Wols et al. (2011) observed a dose distribution peak that was shifted towards higher values using RANS-based CFD simulations in a reactor with three lamps placed perpendicular to flow with baffles placed upstream of each lamp at the top and bottom walls. In addition, the long tail in the dose distribution that existed in the

reactor without the baffles was not observed in the modified reactor. Finally, disinfection efficiency of *B. subtilis* increased by two fold in the reactor modified using baffles.

In a reactor with a single lamp placed perpendicular to flow, Wols et al. (2010) compared the performance of a reference reactor, i.e. no modifications, with those containing baffles placed immediately upstream, at the lamp center and immediately downstream of the UV lamp. In the reactor simulations performed using LES, a range of mean doses (0.54 – 0.63 mJ/cm^2) and disinfection levels (1.45 – 2.11 log units) were predicted for the various scenarios. This occurred due to the velocity profiles that were significantly different from each other in all four cases. The placement of the baffle narrowed the channel through which the water travelled through, thus increasing velocities. However, when the baffle was placed immediately downstream of the lamp, the increased velocity zones around the lamp travelled towards the wake region of the lamp, thus having the best performance of the reactors tested. Furthermore, modifying the walls of the reactor in a wave-like shape forces the particles to travel closer to the lamps and thus improving the performance of the reactor.

Baffles have also been observed to improve the performance of annular type UV reactors by increasing transverse mixing. In an annular reactor with four lamps, Blatchley et al. (1998) incorporated baffles on the walls of the channel and mounted rings on the quartz sleeves that surrounded the lamps. The authors observed better MS2 coliphage inactivation in the modified system at all flow rates. However, at the higher flow rates, a more drastic improvement in the performance was observed, almost two fold. The effects

of the modification lessened at lower flow rates. Thus in these studies, the inclusion of modifications such as baffles, rings or wave-like reactor walls, was shown to improve reactor performance.

2.2.5. UV Intensity models

The UV intensity models take into account certain phenomena in optics such as refraction, reflection and absorption described earlier. Snell's Law provides the relationship between incident angle ($\sin\theta_1$), refractive angle ($\sin\theta_2$) and the refractive indices of two media (n_1 and n_2). Snell's law is described as:

$$n_1 \sin\theta_1 = n_2 \sin\theta_2 \tag{2.2}$$

Reflection of light is governed by Fresnel's Law (Meyer-Arendt, 1984), the reflectance (*R)* is:

$$R = \frac{1}{2}[r_{\parallel}^2 + r_{\perp}^2] \tag{2.3}$$

where $r_{\parallel}$ = amplitude of the radiant energy parallel to the plane of incidence

$r_{\perp}$ = amplitude of the radiant energy perpendicular to the plane of incidence

The irradiance in an absorbing medium can be calculated as:

$$E = E_0 U \tag{2.4}$$

where E and E_0 = irradiances with and without absorption

U = attenuation factor due to absorption

Finally, the attenuation factor is based on Beer-Lambert law:

$$U = exp[-\alpha(\lambda)l] \tag{2.5}$$

where $\alpha(\lambda)$ = napierian absorption coefficient at wavelength λ

l = path length (cm)

The various fluence rate models that exist are the multiple point source summation (MPSS) developed by Jacob and Dranoff (1970), the multiple segment source summation (MSSS) developed by Bolton (2000) and the line source intensity (LSI) introduced by Blatchley (1997).

2.2.5.1. Multiple Point Source Summation (MPSS)

The MPSS approach (Jacob and Dranoff, 1970; Scheible et al., 1985; Suidan and Severin, 1986) is based on dividing the linear lamp into a series of *n* equally spaced point sources

in an absorbing media. In this approach, the fluence rate from a specific point emanates uniformly in all directions. The power output for each point source is *P/n*, where *P* is the total UV power output of the lamp in the wavelength band of interest. The calculation of the fluence rate from point source A to point B with reflection and absorption is as follows:

$$I_A = (1 - R_1)(1 - R_2)\frac{\frac{P}{n}}{4\pi(d_1 + d_2 + d_3)^2} T_w^{d_3/0.01} T_q^{d_2/0.01} Focus \tag{2.6}$$

where I_A = fluence rate at point A

R = reflectance factor

d_1 = path length through air

d_2 = path length through the quartz sleeve

d_3 = path length through water

T_w = 10 mm path length transmittance of water

T_q = 10 mm path length transmittance of quartz

Focus = represents the concentrating effect caused by refraction

2.2.5.2. Multi Segment Source Summation (MSSS)

The MSSS model (Bolton, 2000) incorporates much of the MPSS model including reflection, refraction and absorption. However, to correct the over-prediction of the MPSS model, the lamp was simulated as a series of differential cylindrical segments, where light is emitted normal to the cylinder surface and decreases with the cosine of the

refraction angle, θ_1. The fluence rate at point B caused by the UV light emitted from segment source A can be written as:

$$I_A = (1 - R_1)(1 - R_2)\frac{\frac{P}{n}}{4\pi(d_1 + d_2 + d_3)^2} T_w^{d_3/0.01} T_q^{d_2/0.01} Focus \cos\theta_1 \tag{2.7}$$

where I_A = fluence rate at point A

R = reflectance factor

d_1 = path length through air

d_2 = path length through the quartz sleeve

d_3 = path length through water

T_w = 10 mm path length transmittance of water

T_q = 10 mm path length transmittance of quartz

Focus = represents the concentrating effect caused by refraction

θ_1 = refraction angle at the air-quartz interface

2.2.5.3. Line Source Intensity (LSI)

The LSI model (Blatchley, 1997) is the continuous (integral) version of the MPSS model, in which the number of point sources, *n*, approaches ∞. The LSI fluence rate at a point with a normal distance *R* from the lamp and a longitudinal distance *H* from the center of the lamp with length *L* is given as:

$$I = \frac{P}{4\pi LR}\left[arctan\left(\frac{\frac{L}{2}+H}{R}\right)+arctan\left(\frac{\frac{L}{2}-H}{R}\right)\right] \quad (2.8)$$

2.2.6. Microbial inactivation models

The two microorganisms normally used for validation are MS2 bacteriophage and *B. subtilis*. The inactivation of MS2 phage is simulated using Chick-Watson kinetics as described by equation 2.9:

$$N = N_0 e^{-kIt} \quad (2.9)$$

where N = organism concentration after UV exposure at respective times t [PFU/mL or CFU/mL]

N_0 = initial organism concentration [PFU/mL or CFU/mL]

k = inactivation rate constant [cm^2/mJ]

I = UV-fluence rate [mW/cm^2]

t = exposure time [s]

In order to simplify this second order equation, the terms E and t can be combined into a single term, fluence (or dose, D, mJ/cm^2):

$$D = I \times t \tag{2.10}$$

On the other hand, the inactivation of *B. subtilis* is simulated using the series event model (Severin et al., 1983) due to the presence of a lag phase. In this model, events, assumed to be a unit of damage, occur in stepwise and is assumed to be an integer function. The rate at which an organism accumulates damage is linear with respect to the UV fluence rate. An organism continues to collect damage as long as it is exposed to UV radiation and is said to be inactivated when it passes a certain threshold (Severin et al., 1983). The concentration of viable organisms, those having reached level $n - 1$ or lower is given by equation 2.11 as follows:

$$N = \sum_{i=0}^{n-1} N_i = N_0 e^{-kIt} \sum_{i=0}^{n-1} \frac{(kIt)^i}{i!} \tag{2.11}$$

When $n = 1$, the series-event model reduces to the conventional Chick-Watson kinetics.

2.3. FLOW AROUND A CIRCULAR CYLINDER

2.3.1. Unconfined cylinder

By virtue of its common occurrence in many different applications and forms, the flow of a fluid around a circular cylinder has been well studied, and is one of the classical

problems of fluid dynamics. The flow was discovered by an artist named Theodor von Kármán when he recognized the familiar alternating pattern of vortices in the wake of the Saint's legs on the surface of the river as he crossed it. The flow field is typically marked by the periodic, alternate formation and shedding of vortices from opposite sides of the cylinder and a regular pattern of vortices in its wake known as the Kármán vortex street. Singular or groups of cylinder-like structures can be found in heat exchangers, cooling systems for nuclear power plants, offshore structures, buildings, chimneys, power lines, grids, downstream of bridge piers in rivers, amongst many others. In many of engineering applications, the strong periodic shedding of Kármán vortices from a cylinder is responsible for problems with flow-induced vibration and noise, the production of highly turbulent and three-dimensional fluid motion in its wake, and structures that experience considerable drag forces. A complete understanding of the fluid dynamics for the flow around a circular cylinder encompasses such fundamental subjects as the boundary layer, the free shear layer, the wake and the dynamics of the vortices formed.

The formation of such alternating vortices, which give the appearance of an upper row of negative vortices and a lower row of positive vortices, were the origin of Strouhal's (1878) classical measurements of the sound frequency produced by translating cylindrical rods through air and for the tones produced by an Aeolian harp as wind blows over a wire or a string. Further, in 1912, von Kármán, not only analyzed the stability of vortex street configurations, but established a theoretical link between the vortex street structure and the drag on the body. He viewed the wake oscillations and alternate generation of vortices as an intrinsic phenomenon. Additionally, he showed that two rows of opposite-

signed vortices were unstable in both a symmetric and anti-symmetric geometry. However, his work did not clearly establish why vortex streets are generated in the first place, which came about from Gerrard (1966) and Perry et al. (1982). Gerrard suggested that a forming vortex draws the shear layer (of opposite sign) from the other side of the wake across the wake center line, eventually cutting off the supply of vorticity to the growing vortex. At the start of motion, the wake cavity contains a symmetrical pair of equal and opposite recirculating-flow regions on either side of the wake. However, when the vortices begin to shed, this cavity opens and instantaneously fluid penetrates through the cavity.

In addition to visualizing the vortex phenomena, many measurements such as Strouhal numbers, coefficients of lift and drag, base pressure (i.e. pressure at a point 180 degrees from the front stagnation point), separation points, surface shear stress, wake velocity measurements such as mean and fluctuation velocity profiles and Reynolds stresses and estimates of the length and width of the "vortex formation" region (Rosenhead, 1953; Wille, 1960; Morkovin, 1964; Berger and Wille, 1972; Oertel, 1990). From these measurements, the vortex dynamics were observed to exist over a large range of Reynolds numbers such that the various flow regimes are based on *Re* numbers. Roshko (1954) defined the flow regimes based on velocity fluctuations, spectra and frequency. He found a "stable" (periodic) laminar vortex shedding regime for Re = 40 – 150, a transition regime in the range Re = 150 – 300, with an "irregular" regime for Re = 300 – 10,000+, where velocity fluctuations showed distinct irregularities. The last regime, termed as the Shear-Layer Transition Regime, is of interest as the *Re* number used in this

study lies in it. This regime is characterized by the developing instability of the separating shear layers from the sides of the body.

2.3.2. Cylinder near a plane wall

Due to the engineering relevance to this flow, there have been a large number of experimental studies. This scenario has several examples such as pipelines on a seabed, flow past a suspension bridge, flow past building construction, heat transfer enhancement in heat exchangers, forced-air cooling of board mounted electronic components, etc. When a cylinder is placed near a wall, the dynamics of vortex shedding as compared to a flow around a cylinder in unbounded condition changed appreciably. The cylinder is under the influence of a non-uniform velocity profile due to the flow over a rigid wall, which has a non-symmetric influence on the body and thus an asymmetry in the strength of vortex shedding. Furthermore, the vorticity shed from the cylinder interacts with the vorticity of the boundary layer resulting in an excited wake-induced boundary layer with complex flow structures. When the gap between the cylinder and the wall is relatively low, the nonlinear interaction is strong, provoking the separation of the boundary layer apart from a drastic change of the entire wake. Thus, the dynamics of vortex shedding in the presence of a wall is influenced by several factors, such as the *Re*, the gap height (*S*), the approaching boundary layer thickness and the free-stream disturbances. To summarize, the major modifications of the flow past a cylinder in the vicinity of a wall can be identified as: (1) deflection of the approaching boundary layer away from the wall, (2) suppression of vortex shedding from the lower half of the cylinder, (3) presence of

separation bubble both upstream and downstream of the cylinder and (4) a significant change of flow parameters such as Strouhal number (*St*), lift and drag coefficient (Sarkar and Sarkar, 2010).

2.3.3. Cylinder confined by two planes

In addition to *Re*, two additional parameters, the gap parameter and the confinement ratio, control the dynamics of the cylinder wake in the case of a cylinder between parallel walls where the gap parameter is defined as the distance between the cylinder and the nearest wall normalized by the cylinder diameter and the confinement ratio as the cylinder diameter over the distance separating the two walls (Rehimi et al., 2008). The confined flow phenomena differ significantly from the unconfined case in the following three factors: 1. the incoming flow is sheared so that the incoming vorticity combines with the vortices shed from the cylinder to alter the vortex structure in the wake region of the cylinder, 2. the flow velocity through the gap above and below the cylinder is higher than that in the unconfined flow scenario due to the blockage. Thus, lower the channel height, higher is the energy of the flow surrounding the cylinder and 3. the interaction with the vortices along the walls interacts with the vortex shedding around the cylinder altering the overall vortex structure in the flow. Consequently, changes in the flow and wake vortex structure can be observed as the height of the channel varies. Thus, the flow

possesses interesting features that are significantly different from the unconfined case (Singha and Sinhamahapatra, 2010).

2.4. **THREE-DIMENSIONAL LASER-INDUCED FLUORESCENCE**

The Laser-Induced Fluorescence (LIF) technique has become an extremely powerful tool to experimentally observe mixing in various types of hydraulic systems including dense jet discharges (such as those from desalination plants) (Gungor and Roberts, 2009), water storage tanks (Tian and Roberts, 2008a; Tian and Roberts, 2008b), outfall discharges (Roberts and Tian, 2004), multiport wastewater diffusers (Tian et al., 2004a; Tian et al., 2004b) and turbulent buoyant jet flows (Tian and Roberts, 2003). The LIF technique quantifies the entire instantaneous tracer concentration field at very high resolution over a planar sampling area. LIF is a non-intrusive technique, like particle image velocimetry (PIV) and laser Doppler velocimetry (LDV), in contrast to traditional point-based techniques such as *in-situ* probes (Roberts, 1979a; Roberts et al., 2001) or extraction of samples (Wright, 1977; Roberts et al., 1989; Roberts and Snyder, 1993). The non-intrusive methods have two major advantages: the flow field is not disturbed by the use of probes and measurements can only practically be conducted at a limited number of points. Furthermore, non-intrusive techniques capture instantaneous concentrations, unlike extraction techniques that only obtain time-averaged results. Prior to 3DLIF, planar LIF (PLIF) or two dimensional imaging techniques were well established (Prasad and Sreenivasan, 1990, Ferrier et al., 1993). Most flows are three-dimensional in nature and two-dimensional systems cannot reveal this three-dimensionality. In addition,

previous LIF systems were limited by spatial variation of laser intensity, short duration of experiments, and limited reactor volumes due to limited computer storage capacity and low camera sensitivity. These limitations have been recently overcome and extended to three dimensions (Tian and Roberts, 2003).

Figure 2.5 shows a schematic of the 3DLIF system developed. A laser beam, with a wavelength of 514 nm and a maximum intensity of 1.75 W, is generated by an argon-ion

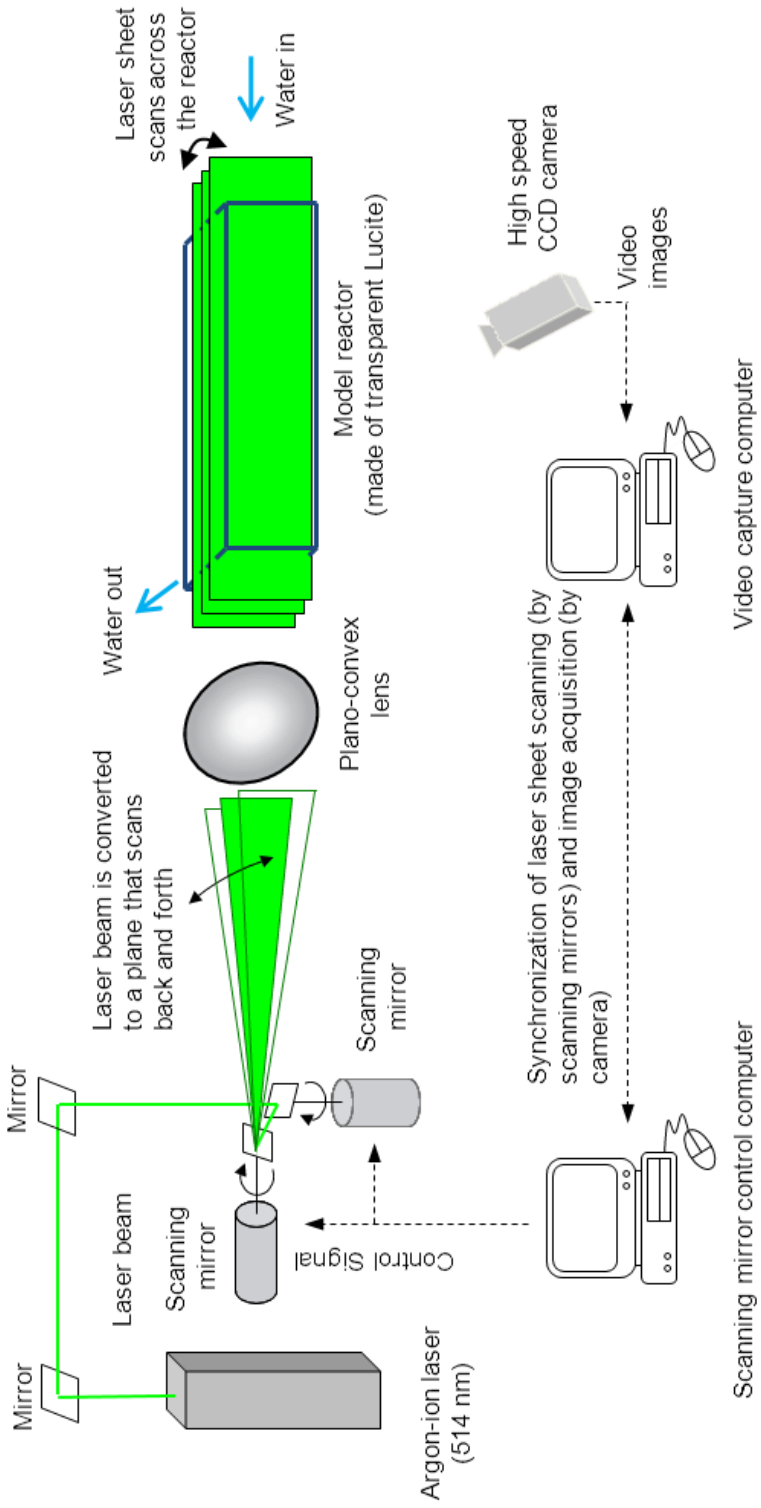

Figure 2.5: Schematic of the three-dimensional laser-induced fluorescence system

laser (Innova 90, Coherent®, Palo Alto, CA), which is used to excite a fluorescent dye, Rhodamine 6G (Sigma-Aldrich, St. Louis, MO). A planar laser sheet was produced by two orthogonal scanning mirrors. The first mirror oscillated rapidly around a horizontal axis to produce a vertical laser sheet while the second mirror scanned the laser sheet horizontally across the width of the reactor. The laser sheet passed through a plano-convex lens of 250 mm diameter and 940 mm focal length (the distance between the lens and scanning mirrors) so that the laser sheets are always parallel to the reactor axis. Each set of three dimensional scans consisted of forty horizontal displaced sheets (completed in 0.2 sec) or of one central sheet for two-dimensional scans. The sheets consisted of 256 gray level images obtained with a high-speed CCD camera (Dalsa® CA-D6, Ontario, Canada), equipped with a sensor with resolution of 532 by 516 pixels and a lens with a focal length of 25 mm (Fujinin, Saitama, Japan).

In Figure 2.6, the first image shows a laser beam passing through a reactor with no scanning. The second image shows the dye fluorescing in the reactor, along with the reflection of the laser light from the walls of the reactor. This reflected light is considered as external noise in LIF experiments and has to be removed. Hence, a long-pass optical filter with a 530 nm cut-off (Schott Glass 530, Reynard Corporation, San Clemente, CA) was placed between the lens and the camera sensor to remove the laser light. The third image in Figure 2.2 is then obtained, where only the light emitted from the fluoresced dye is captured by the camera. Real time images were captured using the Video Savant Version 4 (IO Industries, Ontario, Canada) software and stored in a high capacity storage device.

The images were then processed pixel-by-pixel to correct for (1) vignetting (occurrence of darker margins due to the optical lens characteristics) and (2) attenuation (loss of laser intensity as it passes through the solution in the test reactor), using the software *TFlook* developed by Tian and Roberts (2003). Vignetting was corrected by equation 2.12, using a standard black and white image.

$$I_c(i,k) = K\frac{I_r(i,k) - I_b(i,k)}{I_s(i,k) - I_b(i,k)} \tag{2.12}$$

where $I_c(i,k)$ = pixels of corrected images at the i_{th} and j_{th} pixel indices

$I_r(i,k)$ = pixels of raw images at the i_{th} and j_{th} pixel indices

$I_s(i,k)$ = pixels of standard white images at the i_{th} and j_{th} pixel indices

$I_b(i,k)$ = pixels of black images at the i_{th} and j_{th} pixel indices

K = average pixel value of the standard white image.

Images are further corrected for attenuation (Koochesfahani and Dimotakis, 1985; Walker, 1987; Van Cruyningen et al., 1990) using Beer's Law, as in equation 2.13. Attenuation is a phenomenon in which the intensity of the laser decreases as it travels through the reactor due to absorption by mainly the dye or any other chemicals present in the water.

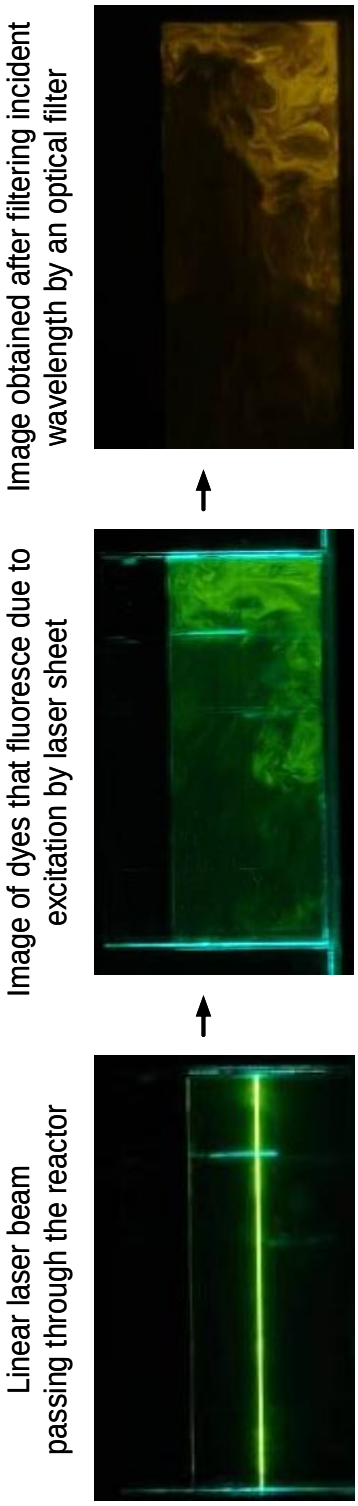

Figure 2.6: Laser beam through a reactor (bottom), dye fluorescence due to excitation by laser (middle) and filtered image by optical filter (top)

$$P = P_0 \cdot e^{-(a_w + 0.00023 \times C)(x - x_0)} \tag{2.13}$$

where P = laser intensity at x

P_0 = laser intensity at x_o

a_w = attenuation coefficient of water

C = concentration of Rhodamine 6G [µg/L].

Incorporating Beer's Law to correct each pixel value, Equation 2.14 was used.

$$I_{cc}(i,k) = \frac{I_c(i,k)}{e^{\sum_{m-1}^{i}(a_w + 0.00023 \times C) \times \Delta x}} \tag{2.14}$$

where I_{cc} = corrected pixel value at the i_{th} and j_{th} pixel indices

Δx = distance between two pixels [L].

Finally, *TFlook* converted the *.raw images into data files that can be read by *Tecplot*® (Tecplot Inc., Bellevue, WA). *Tecplot*® was used to develop profiles of dye concentrations, analyze lateral mixing, and produce 2D and 3D flow animations. The dye concentration was estimated from the pixel intensity in the LIF images by using a calibration factor that was obtained by a linear regression of fluorescence intensity of images of a standard dye solution with a concentration of 20 µg/L.

2.5. PARTICLE IMAGE VELOCIMETRY

Particle Image Velocimetry (PIV) is another nonintrusive measurement technique that visualizes the flow characteristics of a given system. This method results in an instantaneous planar velocity field. The laser and camera system described in Section 2.4 was used to illuminate and capture the particles. In this method, tracer particles have to be added to the flow, which are illuminated in a plane of the flow at least twice within a short time interval. It is assumed that due to the small size of the particles, they travel with the local flow velocity. The light scattered by the particles is recorded by the CCD camera. The displacement of the particles in the captured images has to be determined (Raffel et al., 1998).

For evaluating the displacement of the particles, each image is divided into small subsections called interrogation areas. The local displacement vector for the images of the tracer particles of the first and second illumination is determined for each interrogation area by means of statistical techniques such as auto and cross-correlation. The projection of the vector of the local velocity (two component vector) is calculated using the time delay between the images and magnification of each image. This process is repeated for all interrogation windows in the recording (Raffel et al., 1998).

PIV has been applied in various fields of engineering such as aerospace, biomedical, civil, chemical, environmental and oceanography. PIV has been applied to investigate the fluid mechanics in air and water mediums. Some of its applications include

understanding unsteady flow phenomena downstream of a circular or square cylinder, flow in an artificial heart assist system, in turbulent jets, in swirling flows observed in gas turbine combustors used in burners, chemical processing plants, spray dryers etc., in various disinfection reactors such as ozone and UV, flow around bridge piers in rivers and to investigate the flow around planktons and other marine animals, amongst others.

2.6. RANDOM WALK MODEL

A random walk is a mathematical formulation of a trajectory consisting of random steps in succession. This includes the path traversed by a molecule in a liquid or gas, the search path of a foraging animal or even the price of a fluctuating stock. Random walk models have been used in many fields such as ecology, economics, psychology, computer science, physics, chemistry and biology.

In terms of UV reactors, the random motion of each individual microorganism forms an appropriate basis for the determination of a dose-distribution function. Random-walk models are closely related to diffusion (Bailey, 1964). In a random walk model, the entire series itself is not random. However, the difference between two consecutive steps, i.e. the change from one period to the next, is random. Hence, in flow-type scenarios, the displacement from one period to another is random. The path travelled by the particle can be described by the following equation for an instantaneous velocity vector field:

$$x(t + \Delta t) = x(t) + u(t) \times \Delta t \tag{2.15}$$

$$y(t + \Delta t) = y(t) + v(t) \times \Delta t \quad (2.16)$$

where $x(t + \Delta t)$, $y(t + \Delta t)$ = Particle position at time $t + \Delta t$ [L]

$x(t)$, $y(t)$ = Particle position at time t [L]

$u(t)$, $v(t)$ = Velocity information at time t [L T^{-1}]

Δt = Time difference between two consecutive steps [T]

In addition, time-averaged velocity data can also be used in a random walk model (Chiu et al., 1999). The following equations describe the path of the particle in this scenario:

$$x(t + \Delta t) = x(t) + [\overline{u(x(t), y(t))} + N_x S_x(x(t), y(t))] \times \Delta t \quad (2.17)$$

$$y(t + \Delta t) = y(t) + [\overline{v(x(t), y(t))} + N_y S_y(x(t), y(t))] \times \Delta t \quad (2.18)$$

where $x(t + \Delta t)$, $y(t + \Delta t)$ = Particle position at time $t + \Delta t$ [L]

$x(t)$, $y(t)$ = Particle position at time t [L]

$\overline{u(x(t), y(t))}$, $\overline{v(x(t), y(t))}$ = Time-averaged velocity data at time t [L T^{-1}]

N_x, N_y = Random numbers taken from independent normal distributions

$S_x(x(t), y(t))$, $S_y(x(t), y(t))$ = Standard deviations of the instantaneous velocity distribution

Δt = Time difference between two consecutive steps [T]

However, exceptions to this time-averaged particle tracking method were observed in transverse velocity distributions in the wake region of each lamp. These regions were observed to exhibit bimodal characteristics due to the vortex-shedding behavior that typifies these regions.

2.7. PROPER ORTHOGONAL DECOMPOSITION

Turbulent flows are characterized by organized motions that appear repeatedly and undergo a characteristic temporal life cycle. These are referred to as coherent structures. Understanding their dynamics and interactions with other coherent structures in the flow will lead to an increased understanding of turbulence and its control (Berkooz et al., 1993). However, identifying coherent patterns in experiments and computer-generated data is not a trivial task since, more often than not, they are hidden amongst incoherent turbulent structures. Finally, large amounts of data needs to summarized in a concise manner so that useful information may be extracted (Kostas et al., 2005).

Proper orthogonal decomposition (POD) has proved to be an effective method for identifying dominant features and events in experimental and numerical data. This technique permits the extraction of spatial and temporal structures judged essential. In addition, it can summarize large quantities of data so that the most useful information about the physical processes occurring may be extracted (Kostas et al., 2005). POD also allows us to evaluate the distribution of energy as a function of scale when the flow is statistically inhomogeneous in one or more directions. The POD method decomposes the

vector signal into modes and it evaluates the contribution that each mode makes to the energy (Liu et al., 2001).

POD has been applied in many fields in fluid mechanics such as flow downstream of a half cylinder in terms of passive control (Cruz et al., 2005), influence of wall proximity on characteristics of wake behind a square cylinder (Shi et al., 2010), flow past a backward-facing step (Kostas et al., 2002; Kostas et al., 2005), annular jet (Patte-Rouland et al., 2001), internal combustion engine flow (Fogleman et al., 2004), natural convective flow above an isothermal horizontal plate (Venturi, 2006), turbulent jet in crossflow (Meyer et al., 2007) and the flow around a circular cylinder (Ma et al., 2000; Ma et al., 2003; Dipankar et al., 2007; Perrin et al., 2007; Konstantinidis et al., 2007).

Traditionally, POD has been applied to velocity field measurements, which are obtained using the PIV technique described in Section 2.4. Meyer et al. (2007) applied POD to instantaneous velocity vectors of a jet in cross-flow, measured using stereoscopic PIV, to determine the largest structures of the flow responsible for mixing. The POD technique facilitated important conclusions about the flow structure that is not apparent from visualization of the vector field such as the wake vortices cause a strong interaction between the jet core and the cross-flow and the two flow phenomena, shear-layer and wake vortices, are not coupled with each other. In addition, Shi et al. (2010) applied POD to velocity vectors, obtained using standard PIV and Time-resolved PIV (TR-PIV), to determine the influence of wall proximity on the wake behind a square cylinder, Bernero and Fiedler (2000) analyzed the flow structures in a jet in counter-flow, Graftieaux et al.

(2001) studied unsteady turbulent swirling flows and Pedersen and Meyer (2002) examined flow structures in a scale model of a ventilated room.

POD on vorticity data has been suggested as a more appropriate quantity to use for coherent structure identification as velocity is not ideal since the structure in the flow would depend on the velocity of the observer. Thus, the modes obtained from a POD analysis of the velocity data may be misinterpreted as a result of observing them in an inappropriate reference frame. A POD analysis on vorticity has the potential to be used for the construction of simplified flow models extracted from the modes. Furthermore, using POD analysis of the flow based on vorticity reduces the overall number of computations, since there is only one component of vorticity as compared to two velocity components, u and v. Kostas et al. (2005) compared a snapshot POD analysis of PIV velocity and vorticity data for a backward-facing step, concluding that the objective identification and description of the dominant vortical structures in a flow is more effective using the POD analysis of the vorticity field than the 2D velocity field. Similar analyses on the vorticity field were conducted in an open channel (Gurka et al., 2006), in a circular cylinder controlled by a synthetic jet (Feng et al., 2011) and in the near wake in turbulent flow past a circular cylinder (Ma et al., 2000; Konstantinidis et al., 2007).

Finally, very few studies exist that have applied a POD analysis to concentration data. POD analysis was applied to velocity field and concentration distribution captured simultaneously in a gas-turbine combustor model (Gnirss and Tropea (2008)) and a counter-flow type t-junction (Hirota et al., (2008)). In both cases, complex unsteady

structures were observed. In both studies, results from the concentration-based decomposition were similar to the POD based on velocity fields. However, the concentration-based decomposition analysis helped discern the dominant mechanism responsible for mixing in these systems, as they are very important in their applicability. POD analysis standardizes turbulent structure identification in terms of eigenvalues and eigenvectors. The method of snapshots (Sirovich, 1987) was used in this study, which is further described in Section 3.7.

CHAPTER 3.

EXPERIMENTAL METHODS

3.1. 3DLIF SYSTEM

Detailed information regarding the 3DLIF system used in this study is given in Kim et al. (2010). Briefly, a laser beam generated by an argon ion laser (Innova 90, Coherent®, Palo Alto, CA) at a wavelength of 514 nm and an intensity of 1.5 W was used to excite a fluorescent dye tracer, Rhodamine 6G (Sigma-Aldrich, St. Louis, MO). The laser beam was first directed toward a mirror which oscillated vertically at high frequency to produce a 2D laser sheet that passed through the center width of a reactor. A high-speed CCD camera (Dalsa® CA-D6, Ontario, Canada) captured fluorescence images at a frequency of 200 Hz. To obtain 3D images, another mirror scanned the laser sheet horizontally across the reactor width once per 0.2 s with 40 images captured per scan. The images, attained using Video Savant Version 4 (IO Industries, Ontario, Canada), were then processed using software TFlook (Tian et al., 2003) which converted the images that can be visualized in three dimensions by Tecplot® (Bellevue, WA).

Since the concentration of the dye was 20 µg/L, the relationship between the concentration and image gray scale level was linear. Calibration of the LIF images was accomplished using software called *TFLook* (Tian and Roberts, 2003) in two steps. The first step accounts for vignetting, where the standard image is brighter in the center and darker at the edges while the second step accounts for the attenuation of the laser beam as it traverses through the channel due to the fluorescent dye. The attenuation is corrected

using Beer-Lambert law where the coefficient of attenuation is dependent on the quality of the water and the concentration of dye used. Complete details of the LIF system and calibration can be found in Tian and Roberts (2003).

3.2. MODEL UV REACTOR

A lab-scale model UV reactor (Figure 3.1) was constructed, using transparent 1.27 cm (0.5 in.) thick acrylic sheets, to examine the hydrodynamics across a single 2.8 cm O.D. lamp sleeve placed perpendicular to the direction of flow. Even though it is less common than circular cross-section in full-scale design, the reactor was designed with a square cross-section (7.62 cm × 7.62 cm, 3 in. × 3 in.) to prevent complications associated with the laser light reflecting from a curved surface. The distance between the wall and the lamp placed closest to the wall of the reactor were similar in the model reactor and full-scale rectangular reactors. In order to achieve flow characteristics that closely represent a full-scale reactor, the influent flow rate was determined by matching the Reynolds number described in equation 3.1.

$$Re = \frac{UW}{\upsilon} \tag{3.1}$$

where U = velocity [LT^{-1}]

W = characteristic length [L]

ν = kinematic viscosity [L^2T^{-1}].

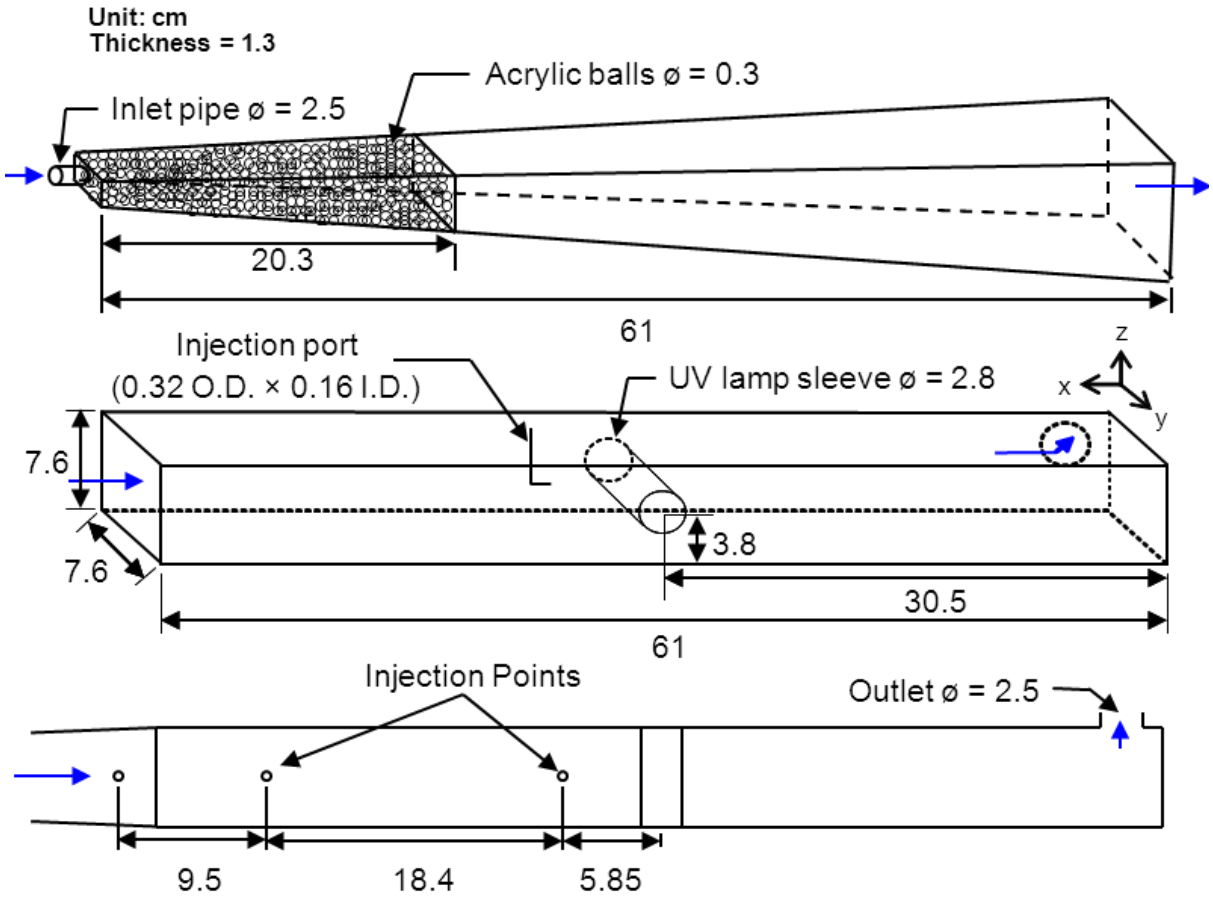

Figure 3.1: Schematic of the model lab-scale UV reactor (dimensions in cm).

The lab-scale model was operated at a flow velocity of approximately 17 cm/s (0.55 ft/s) or a flow rate of 59 L/min (15.5 gal/min), which corresponds to *Re* = 4,900 based on the sleeve diameter. In full-scale UV reactors, velocities range from 4 to 225 cm/s with *Re* between 1,000 and 100,000 based on sleeve diameter. Since water was transported through a 2.54 cm (1 in.) diameter pipe to the reactor inlet, an abrupt change in the cross-sectional area would lead to significant flow separation, which is not characteristic of full-scale reactors. The inlet was, therefore, designed to gradually diverge and packed with 0.32 cm (1/8 in.) acrylic balls to evenly distribute the influent velocities and avoid flow separation. In order to avoid inlet effects on the region of interest, the upstream region was of constant cross-section for a length of more than ten cylinder diameters.

3.3. TRACER TESTS

Tap water, dechlorinated and filtered through 10 and 1 μm cartridge filters at room temperature (20 ± 2^{o}C), was fed to the model reactor at the design flow rate. Upon reaching steady-state, a solution containing 20 μg/L Rhodamine 6G was continuously injected into the reactor at 25 mL/min via a 1.27 cm (0.5 in.) long L-shaped injection port (0.32 cm (1/8 in.) O.D., 0.16 cm (1/16 in.) I.D.) aligned in the stream-wise direction. Dye was injected at the center of the lamp sleeve, and 1.27 cm and 2.54 cm (0.5 in. and 1 in., respectively) above the center of the sleeve through the injection point located 5.85 cm (1.75 in.) upstream of the sleeve center and 3.81 cm (1.5 in.) from the side wall. The tracer was conservative since the tests were performed without UV lamps; the sleeve was

filled with water to minimize laser light reflection off the sleeve. Image capture was initiated prior to dye injection to completely capture its transport around the sleeve. The spatial resolution of concentration images was approximately 2.5×10^{-2} cm as compared to the Batchelor scale of 1.52×10^{-4} cm while the temporal resolution was approximately 5.1 ms, less than the convective time scale of about 0.15 secs.

3.4. PARTICLE IMAGE VELOCIMETRY

In a separate experiment, the velocity field in the wake region of a circular cylinder was measured using the laser system described above. Silver coated hollow glass spheres (Dantec Dynamics, Denmark), d = 10 μm and ρ = 1.1 kg/m^3, were injected more than ten cylinder diameters upstream of the channel inlet at a flow rate of approximately 1000 mL/min such that the particles were completely and uniformly dispersed as they entered the test section. Since the camera captures the laser light scattered by the particles, the images were recorded in the absence of the long pass optical filter. The laser scanned across a 2D vertical slice through the center of the reactor (38.1 mm from the side walls) capturing images for 20 s at a frame rate of 200 Hz. The duration of the sampling was significantly longer than the largest time scales of the highly turbulent flow, i.e., one vortex shedding cycle around the cylinder. The spatial resolution of the velocity images was 0.169 cm as compared to the Kolmogorov scale of 0.0048 cm while the temporal resolution was approximately 5.1 ms, less than the convective time scale of about 0.15 secs.

The PIV images were processed using the DaVis Imaging software (LaVision, Germany). A multipass algorithm with decreasing window sizes of 32 × 32 pixel to 16 × 16 pixel with 50% overlap was used. Masking was applied to eliminate vector processing within the cylinder while a median filter, which was determined by the median value and the standard deviation of the vectors, was used to eliminate erroneous vectors. The final PIV grid was 39 × 66 vectors. Subsequently, when compared to the raw particle images, the resolution of the resulting velocity field was reduced as a vector was present every 8 × 8 pixels. In order to achieve a complete comparison between the concentration data and velocity field data, a new dataset was created by applying a moving average over an 8 × 8 pixel window to obtain an identical resolution as the velocity vector fields. This new dataset was termed the reduced resolution LIF (denoted as 'RRLIF') whereas the original concentration images are denoted as 'LIF' throughout this study. Thus, a comprehensive comparison of the POD analyses using various sampling techniques with different resolutions was achieved.

3.5. REACTIVE TRACER TESTS

The reactive test experiments were conducted similar to the conservative tracer tests described in section 3.3 with the following exceptions: 1. The UV lamp (GPHXA354T6L, Light Sources, Inc.; Orange, CT) used was a low pressure high output (LPHO) amalgam lamp with an arc length 27.8 cm and 19 W UV output at 254 nm and was turned on and 2. H_2O_2 was introduced more than 20 cylinder diameters upstream of the reactor inlet such that it was well-mixed around the lamp with a final concentration of 2 ± 0.1 mM. Two

methods, differing in the location of the tracer dye injection, were employed to analyze and quantify the reactor dose. In the first method, termed ‘premixed’, a solution of dye (625 ppb) and H_2O_2 was introduced upstream of the reactor at approximately 300 mL/min. In the second method, referred to as ‘path specific’, the tracer was injected at various heights (0, 0.64, 1.07 and 2.54 cm above the lamp center and at the top wall) at three upstream distances, 2.5, 10.1 and 17.7 cm from the lamp center. The Rh6G and H_2O_2 solution introduced into the reactor led to an 18 ± 1% (16% reduction was caused due to H_2O_2) reduction in the UV transmission for every 1 cm increase in the distance away from the lamp. As a control, H_2O_2 was not introduced into the reactor in the first method to account for increased dye intensity around the lamp and reflection of the UV light by acrylic while dye and H_2O_2 were injected with the lamp turned off in the second method. The UV lamp was on for 20 min prior to each experiment. Each path specific case was triplicated with 1L sample collected at the outlet and analyzed for dye degradation.

For ‘premixed’ calibration, various Rh6G concentration solutions (final concentration of 400 – 1000 ppb) was injected into the reactor with lamp on and 1000 images were captured. Each gray-scale pixel value on the resulting images was subtracted with the dark base (i.e. no laser source). Finally, for each pixel, its value was plotted against the tracer concentration upstream of the lamp for all Rh6G concentrations to determine a linear correlation. Using this two-dimensional calibration map and the upstream tracer concentration in the reactive tracer experiment, a map for the unreacted tracer (UV lamp on without H_2O_2) or initial concentration, C_0, was obtained.

3.6. LAGRANGIAN-BASED ANALYSIS

A software *Tecplot*® (Bellevue, WA) was used to generate particle paths from the instantaneous velocity field at an integration time step of 0.0005 s for the Lagrangian-based analysis. Each uploaded velocity file was given its appropriate time stamp starting at 0 s with a $\Delta t = 0.005$ s. Initial particle locations were introduced at the center, 1.27 cm off-center and at the wall. For the center and 1.27 cm off-center, two streamlines were introduced above and below the lamp to analyze various tracks. The Lagrangian analysis was performed forty one times on a dataset of 1s each (sufficient for particles to traverse the 13 cm section) with a delta of 0.125 s between the first image in each analysis. The intensity values (description of intensity model is provided in Supporting Information) corresponding to particle path coordinates were then obtained using Matlab™ (MathWorks, Natick, MA) software and were used to calculate the accumulated *IT*.

3.7. PROPER ORTHOGONAL DECOMPOSITION

POD analysis standardizes turbulent structure identification in terms of eigenvalues and eigenvectors. The method of snapshots (Sirovich, 1987) was used in this study. The method and equations described below are specific for the analysis of the velocity field; however, it can be applied to other spatially varying fields like vorticity and concentration. This method requires all the snapshots to be placed in a matrix $\boldsymbol{U}$, where the individual velocity field matrices are reshaped into a column of $\boldsymbol{U}$, where each

column is a different time step and arranged so that the *u* component is followed by the *v* component. The autocovariance matrix was computed as $\boldsymbol{C} = \boldsymbol{U}^{\boldsymbol{T}}\boldsymbol{U}$, where ^{T} denotes the transpose operator. The eigenvalue problem is solved using equation (3.2) (Meyer et al., 2007) with the solutions being arranged in descending order according to the magnitude of the eigenvalue. The resulting eigenvectors, A^i, form the basis for the POD modes, ϕ^i, as described by equation (3.3) (Meyer et al., 2007).

$$CA^i = \lambda A^i \tag{3.2}$$

$$\phi^i = \frac{\sum_{n=1}^{N} A_n^i u^n}{\left\| \sum_{n=1}^{N} A_n^i u^n \right\|} \tag{3.3}$$

where $i = 1, 2, \ldots, N$

λ = the eigenvalue

A_n^i = nth component of the eigenvector corresponding to the ith eigenvalue λ_i

Each snapshot can be reconstructed with a number of modes using expansion coefficients, a_i, for each POD mode i. These coefficients are determined by projecting the fluctuating part of the field in consideration onto the POD modes (equation 3.4) (Meyer et al. 2007). Finally, the reconstructed snapshots of the fluctuating part using N modes can be attained (equation 3.5) (Meyer et al., 2007).

$$a^n = \psi^T u^n \tag{3.4}$$

$$u^n = \sum_{i=1}^{N} a_i^n \phi^i = \psi a^n \tag{3.5}$$

where an array with all the modes, $\psi = [\phi^1 \phi^2 \dots \phi^N]$ (Meyer et al., 2007).

The amount of the total kinetic energy from fluctuations in the snapshots that is associated with a given POD mode is proportional to the corresponding eigenvalue. The ordering of the eigenvalues and eigenvectors therefore ensures that the most important modes are the first few modes. Additionally, this means that these modes will be associated with the large-scale flow structures that occur time and again, often cyclically. Thus, a given snapshot can often be reconstructed satisfactorily using the first few modes, depending on the energy distribution. The snapshot POD analysis was performed using the computing language MATLAB™ and the code is included in Appendix B.

3.8. UV FLUENCE RATE MODEL

Figure 3.2 shows the decrease in UV intensity as a function of radial distance from the lamp. Multiple Point Source Summation (MPSS) was used to model the spatial intensity output from the UV lamp as described by equation 3.6 (Jacob and Dranoff, 1970; Bolton, 2000; Sasges et al., 2007)

$$I(r) = (1-R_1)(1-R_2)\sum_{1}^{n}\left[\frac{P \times L/n}{4\pi} \times Factor \times \cos(\alpha)\right] \times UV_{abs} \tag{3.6}$$

where $I(r)$ = lamp intensity at point located at distance r from the lamp (mW/cm^2)

R = reflectance factors

P = power output from the UV lamp (mW/cm)

L = arc length of the UV lamp (cm)

n = number of points the lamp is modeled as

Factor = accounts for refraction

α = angle between normal to the UV lamp and line from the point source to location of interest

UV_{abs}= UV absorbance of the water

The algorithm approximates the UV lamp intensity at a point, located at a distance r from the lamp, as equivalent to n point sources evenly spaced along the longitudinal axis of the lamp. The lamp output was assumed to be Lambertian, so the radiant intensity from the lamp surface is directly proportional to the cosine of the angle between the point r and the surface normal (Sasges et al., 2007). Lastly, the model assumes the same UV intensity at radially equidistant points from the UV lamp.

The UV transmittance (UVT) at 254 nm, measured using an Agilent 8453 UV-vis spectrophotometer (Palo Alto, CA), was 82%. The lamp was modeled as 200 point sources with a total power assumed to be 0.7 W/cm (19 W power output at 254 nm). The refractive indices for water, n_w = 1.38, and for quartz, n_q = 1.52 was obtained from Bolton (2000).

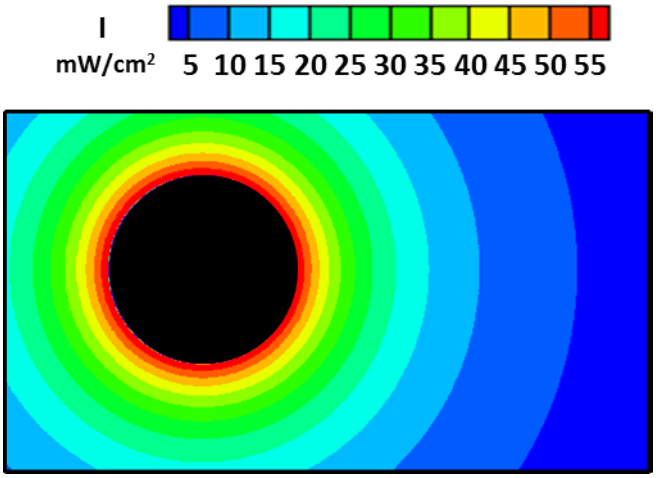

Figure 3.2: UV intensity contour plot (mW/cm^2) as calculated by MPSS model with 83% UVT (1.0 cm optical path) and lamp output power of 65 W with 30% efficiency (27.8 cm arc length).

CHAPTER 4.

UV REACTOR FLOW VISUALIZATION AND MIXING QUANTIFICATION USING THREE-DIMENSIONAL LASER-INDUCED FLUORESCENCE

4.1. FLOW VISUALIZATION USING 3DLIF

Figure 4.1 shows how three dimensional flows in a UV reactor can be visualized using 3DLIF at a high resolution (corresponding to millions of sampling points), which is not possible with traditional dye tracer test techniques. These images were obtained from a 3DLIF experiment performed with dye injected at the point in the center of the y-z plane. The region from the sleeve to the outlet is dissected in the stream-wise (x-z plane), span-wise (x-y plane), and cross-stream (y-z plane) directions. The cross-sections are presented as concentration contours normalized by the initial dye concentration in false color with red as the highest and blue as the lowest dye concentrations. The gray-colored semi-transparent surface is an iso-concentration surface at a level of 0.15 (arbitrary low threshold normalized value) that indicates the outer extent of the dye cloud as it moves through the reactor. The lamp sleeve is represented as a red cylinder in the 3D images and as a black circle/rectangle in the 2D slices.

The 3DLIF visualization shows that the presence of the sleeve affects the dye flow in all three dimensions, however, more pronouncedly in the stream-wise direction. As the dye approached the sleeve, it underwent spreading in all directions as shown by the expansion of the iso-concentration surface which fluctuated (not shown) about the center. Upon

contact with the sleeve, the dye plume spread axially as momentum carried it past the sleeve, depicted by the red contours around the sleeve in the stream-wise and cross-stream slices. Lower dye concentrations in the wake region indicated increased mixing while a von Karman vortex street was observed in the stream-wise slice, albeit vaguely. Furthermore, a vertical slice in the stream-wise direction offset horizontally by 2.5 cm also showed the presence of the vortex street, lower dye concentrations in the wake region and higher concentrations around the edges of the cylinder, confirming previous observations that the flow around a circular cylinder is three dimensional (Williamson, 1996). While the presence of the lamp certainly enhanced dispersion in all three directions, it mainly complicated the flow in the stream-wise direction with the more unsymmetrical flow patterns.

Based on the observations in Figure 4.1, further analysis of the stream-wise plane in 2D (Figure 4.2) was performed to visualize the details of the flow. Figure 4.2a consists of time-series images, spanning 0.12 sec, for a dye injected at the center height when the planar laser sheet was fixed at the mid-point between the walls. These 2D images depict the two main characteristics of the flow around a cylinder: the recirculation region and the von Karman vortex shedding (Williamson, 1996; Zdravkovich, 1997). The presence of the sleeve created a low pressure zone in the wake region, causing water, for example, from the top of the cylinder to rotate clockwise and fill up this region (Figure 4.2a). At the next instant, a vortex on the opposite side of the lamp was formed (not shown) which rotated counter-clockwise into the wake region that caused a release of the first vortex, hence vortex shedding occurred. Immediately, the released vortex began to grow in size

while simultaneously, a new vortex, on the same side of the cylinder, was created and the cycle continued (Zdravkovich, 1997).

It is important to note that this study visualizes the flow around a cylinder in the presence of two additional shear layers due to boundary layers at the walls, representative of the flow in UV reactors. Very few experimental studies were focused on this flow, one at very low *Re* ($\leq$ 250, based on the cylinder diameter) (Rehimi et al., 2008) and another at very high *Re* (= 140,000) (Braza et al., 2006). The presence of the lamp induced blockage or a reduction in the cross-sectional area leading to higher velocities around the cylinder by a factor of 1.6. This caused an increase in the length of the recirculation zone as the increase in momentum forced the dye to travel further as compared to an infinite domain (Singha et al., 2010). The length of the mean recirculation zone, which was measured as the extent of the red contour in the wake region in the concentration plot averaged over 5 s (Figure 4.3b), was approximately 1.75 cm. In addition, the confinement suppressed the complete formation of vortex structures such as the von Karman streets that are typically observed in the cross-flow across an isolated cylinder (Williamson, 1996; Zdravkovich, 1997). Finally, the vortex shedding frequency was characterized using the Strouhal number $St = fD/U$, where f = vortex shedding frequency [T^{-1}], and D = diameter of the cylinder [L]. *St* was found to increase when a cylinder is placed near a plane wall (Price et al., 2002). Typical values for the flow in an infinite domain at $Re = 4{,}900$ is $0.18 \leq St \leq 0.22$ (Zdravkovich, 1997). However, in this setup, $St = 0.28$, calculated using Fast Fourier transform (FFT) of the transient dye concentration at a point 1.5 cm downstream of the sleeve center (data not shown). Thus, the presence of the confinement and the sleeve, due

to an increase in velocities around the cylinder, increased the frequency of vortex shedding.

Chiu et al. (1999b) suggested that the recirculation zone increased the residence time for some microorganisms, based on the analysis of a large-scale reactor with 25 lamps placed perpendicular to flow in a staggered pattern. According to their random walk model based on laser Doppler velocimetry (LDV) measurements, particles that were trapped in the wake region spent longer time in the reactor, thus accumulating a higher dose. This increase in residence time for some microbes caused other organisms to short-circuit through the reactor as they travelled following a higher velocity path found closer to the walls of the reactors and received a lower dose. Similarly, Sozzi and Taghipour (2006) observed regions of higher velocities along the walls of an annular reactor that reduced the UV dose delivered to the microbes. This velocity gradient would lead to minimal transverse mixing in the system, deviating from the ideal plug-flow. In order to analyze these paths, the height of dye injection was increased from the center. Figure 4.3 shows the instantaneous and time-averaged flow of the dye when injected off-center at 1.27 cm (Figure 4.3a and 4.3b) and 2.54 cm (Figure 4.3c and 4.3d) above the center of the sleeve. The sequence of images presented is approximately 0.080 sec and 0.13 sec, respectively.

In comparison with the center injection, the off-center injections showed less dye flow into the wake region. In Figure 4.3a, dye entered the wake region, however, with declining instances as compared to the center injection. Figure 4.3b showed highest concentrations directly above the lamp sleeve, while only about 60% of the dye entered

the recirculation zone as indicated from the legend. Only some of the dye that rotated clockwise into the recirculation zone remained. Then, from below the cylinder, water, rotating counter-clockwise, entered into this zone causing the vortex to release at the top of the cylinder, hence the vortex was shed. Simultaneously, water entered the recirculation zone and the cycle was repeated. Finally, downstream of the cylinder region, dye was observed to be entrained into a von Karman vortex street. Hence, even though dye was injected away from the center, the presence of the cylinder affected this path of travel, entraining substantial amounts of dye into the wake region. Negligible amounts of dye entered the recirculation zone and no vortex was shed when dye was injected at 1 cm; all of the dye followed a straight path away from the recirculation zone past the sleeve. These observations were supplemented by Figure 4.3d which showed all the dye flew past the cylinder close to the walls followed by minimal dye mixing occurring downstream of the UV lamp.

In order to supplement the above observations, dye concentration as a function of radial distance away from the lamp (Figure 4.4) was analyzed. Concentrations from circular discs around the cylinder (Figure 4.5) were obtained from the time-averaged plots of each injection case using *Tecplot*®, where each disc, with radial increments, Δr = 0.05 cm, from the surface of the sleeve, had a single averaged dye concentration value. As expected, the highest dye concentrations were found closest to the lamp in the center injection, which would correspond with the higher UV intensities thus receiving the highest doses. For the off-center cases, the highest dye concentrations corresponded with distances away from the lamp, thus would be exposed to lower UV intensities

(approximately 20% and 4% of the lamp surface intensity for 1.3 cm and 2.5 cm off-center injections, respectively, from Figure 4.4 inset) and hence would receive a proportionally lower dose. Superimposed on the effect of decreased residence time at an off-center injection as discussed above, this would lead to much lower level of inactivation compared to the center injection, the quantitative evaluation of which is the focus of a future study.

4.2. APPROACH SECTION

Dye, when injected at the wall, showed increased dispersion as the length of the inlet section increased, hence a higher probability of microbes entering the region close to the UV lamp. Dye was injected at 20 mL/min at the top wall through point sources located either at 22.9 cm (9 in.) or 32.4 cm (12.75 in.) upstream of the lamp sleeve. The resulting dye concentrations around the sleeve are presented in Figure 4.6 as time-averaged normalized plots of 3000 images captured at 125 Hz. Water flows from the left while the laser enters the reactor from the right. Since the sleeve partially blocked the laser light, there was a sharp gradient in dye concentration (from green to blue) at the edges of the sleeve where the dye concentrations should be higher than it appears. Values below 0.2 were cut-off (indicated as white) to show the extent of dye dispersion.

Dye injected 22.9 cm upstream of the sleeve showed that the highest dye concentrations followed a path close to the wall with very little dye entrained into the wake region. Dye dispersion was limited such that only about 30% of the initial dye concentration was detected at the top surface of the sleeve and less than 20% of the initial dye concentration

immediately upstream of the sleeve. Dye injected 32.4 cm upstream of the sleeve established that the highest dye concentrations were found at the wall upstream of the sleeve. However, due to the increased distance of travel, greater dye dispersion was observed, such that 35 – 40 % of the initial dye concentration was observed immediately upstream and downstream of the sleeve. Hence, by increasing the distance of travel upstream of the lamp array, the paths that led to short circuiting in UV reactors became limited since more dye entered the region closer to the lamp surface. Sozzi and Taghipour (2006) and Moreira et al. (2007) analyzed annular reactors with inlets parallel and perpendicular to lamp axis, and suggested that rearranging the inlet altered the velocity field, thus having a significant impact on the UV dose distribution and the reactor performance. Moreira et al. (2007) further examined a reactor with three inlets placed perpendicular to the lamp axis and found that when operated simultaneously, they behaved like a plug-flow with limited axial dispersion and was more efficient than a reactor with a single perpendicular to lamp inlet.

Chiu et al. (1999b) established that particles that entered close to the wall had a higher probability of experiencing a low UV dose due to higher velocities and distance from the lamp. In order to reduce short-circuiting for microorganisms, the length of the approach section leading to the lamp array might be increased such that microbes entering the reactor at a specific location (e.g. close to the wall) would have an equal probability of traversing regions close to the lamp where UV intensities are higher. Zhao et al. (2009) showed that a longer straight pipe inlet placed perpendicular to an annular reactor shifted the peak of the dose distribution to higher values and increased the reduction equivalent

dose (RED) predicted using microspheres. Based on the results of this study, a minimum straight inlet channel length of at least 30 cm or about 11 sleeve diameters is required to significantly increase the probability of microbes passing through higher UV intensity zones. This, however, depends on the upstream hydraulics such as the flow rate and the velocity profile which defer between reactors. The results show that 3DLIF can be utilized to optimize the length of the approach section to help improve the performance of UV reactors.

4.3. OUTLET SECTION

Mixing of the tracer dye across the reactor height at the wake and the outlet as a function of time was also examined. The degree of mixing can be inferred from a statistical analysis of the tracer concentration over the spatial and temporal variation by computing the coefficient of variation (COV) defined as:

$$\mathrm{COV} = \frac{\sqrt{\frac{1}{n-1}\times\sum_{i,j}\left(C\left(x,y_i,z_j,t\right)-\frac{1}{n}\times\sum_{i,j}C\left(x,y_i,z_j,t\right)\right)^2}}{\frac{1}{n}\times\sum_{i,j}C\left(x,y_i,z_j,t\right)} \qquad (3.1)$$

where n = number of data samples at a given time (n = 1,000)

C = dye concentration

i and j = indices of elements in the y and z direction

t = time.

A lower value of COV indicates a more uniform distribution of tracer concentration or greater mixing across a given section. The temporal variations in COV for the different injection heights at the vertical wake section (Figure 4.7a) suggested that as the dye was injected further away from the center, the COV increased, implying a non-uniform tracer distribution. This difference in mixing is due to the greater mixing that occurred in the recirculation zone for the center injection. The COV as a function of time at the outlet (Figure 4.7b) showed the same upward trend for the various injection heights as observed at the wake region. In addition, the standard deviation of the COV from the mean, denoted next to each average line (shown in green), increased with the injection height. For the off-center injections, the larger fluctuations in the outlet dye concentration would have a direct effect on the biodosimetry results and consequently the RED values.

To further quantify these fluctuations, the standard deviation, σ, (equation 3.2) of the tracer concentration at various vertical line sections along the length of the reactor was computed (Figure 4.8). The standard deviation at a point in each vertical section represents the deviation in the concentration compared to other values along that section. As such, a low standard deviation indicates a lower variation in the concentration about the mean at that point, i.e., greater mixing.

$$\sigma = \sqrt{\frac{1}{N-1}\sum_{i=1}^{N}(C_i - \overline{C})^2} \tag{3.2}$$

where N = number of samples over time (1,000 at each section)

C_i = instantaneous concentrations

$\overline{C}$ = time-averaged concentrations.

As expected, the center injection revealed a low standard deviation in the wake region, confirming prior observations of increased mixing compared to the off-center injections. Analyzing section (i), where the flow separates around the sleeve, the center injection case showed two peaks around the lamp that corresponded to the movement of the dye around the cylinder. A smaller peak in the wake region was observed indicating the dye was well mixed temporally as opposed to 1.3 cm injection, where a larger peak indicated lower mixing. The off-center injection cases also showed the presence of a relatively large peak at the dye injection height. At section (ii), the center injection showed two symmetrical peaks, which occurred due to the origination of the von Karman vortex streets. Furthermore, the region between the peaks showed a higher standard deviation than in the wake region, indicating relatively lower mixing. For the 1.3 cm injection, the standard deviation became more uniform in the central region of the reactor while the large peak close to the wall in the 2.5 cm injection indicated the tracer dye continued travelling the short-circuited paths.

The outlet profile for the center injection was uniform across the reactor height. A relatively flat standard deviation profile across the reactor height indicated uniform mixing. Ignoring wall effects, i.e., where the standard deviation decreased fairly quickly close to the wall, the standard deviations were within 10 % of the mean. However, the

standard deviation profiles at the outlet for the off-center injection cases had a greater variation across the reactor height compared to the center injection. A few inactivated microbial samples collected at the outlet in biodosimetry would not be sufficient to capture the fluctuations observed causing deviations in dose estimations. Therefore, a minimum reactor length downstream of the final lamp array has to be defined where the fluctuations across the outlet is found to be fairly uniform.

4.4. CONCLUSIONS

This study applied the 3DLIF technique for the first time to visualize and quantitatively analyze the flow across a UV lamp in a model reactor used for drinking water treatment. In addition to three-dimensional mixing, the technique successfully visualized the two-dimensional, transient mixing behaviors within the reactor, which has not been possible with traditional tracer test techniques. It is also noteworthy that the 3DLIF technique is non-intrusive, *i.e*. there is no disturbance in the flow due to the placement of the sampling probe. Tracer tests revealed unsteady turbulent flow characteristics such as the recirculation zone and the von Karman vortex street that are normally observed in flows around cylinders. The length of the recirculation zone and the Strouhal number were found to increase in the confined flow compared to an infinite medium. Paths away from the center height, characterized by higher velocities and less influence of the cylinder, were also analyzed. The results demonstrated that a major difference in these pathways was the decreasing amount of dye entering the recirculation zone, which has a higher residence time, as the injection height increased. The results also suggested that a longer

approach length was beneficial to increase the probability of microbes entering the region around the lamp sleeve irrespective of their entrance height into the reactor. Lastly, the length of the outlet i.e., distance from the last lamp array to the reactor exit, was examined as mixing at the outlet was determined to drastically vary over time with an increase in injection height. A well-mixed outlet, i.e., when the concentration profile across the reactor height is within 10% as in the center injection case, would be desirable to improve the accuracy of the biodosimetry results. These inlet and outlet analyses were the first of its kind and aid in the optimization of the reactor design.

Numerous studies that experimentally validate the hydraulics and predict spatial dose distributions in UV reactors have employed RANS based CFD simulations. However, discrepancies between the model's calculations and the actual measurements, which are mainly caused by turbulence modeling, occur near the wake region of the lamp (Liu et al., 2007; Wols et al., 2010a; Wols et al., 2010b). For a better prediction of the time dependent turbulent flows and UV dose distributions, advanced models such as large eddy simulation (LES) need to be used, evident from the vast difference in the instantaneous center injection flow (Figure 4.2a), as opposed to the time averaged flow (Figure 4.2b). In addition, results from Wols et al. (2010a) validate the above findings that LES will result in a more physical and accurate representation of the flow velocities and the transport and mixing within UV reactors which will likely lead to a more accurate prediction of the UV dose received by microorganisms. Therefore 3DLIF is a powerful tool to fully capture the flow in UV reactors that can aid in the validation of LES results

and provide information on the temporal dose distributions that has not been considered in past studies.

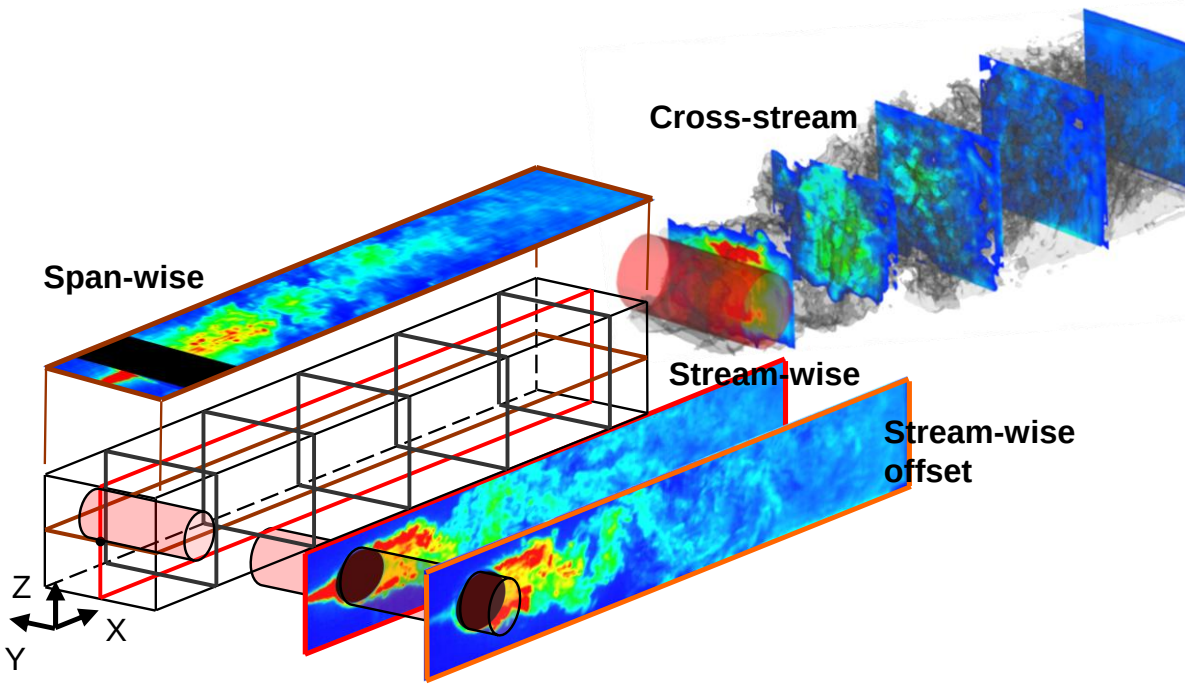

Figure 4.1: 3D LIF images showing the dye transport in the UV reactor dissected into multiple cross-sections.

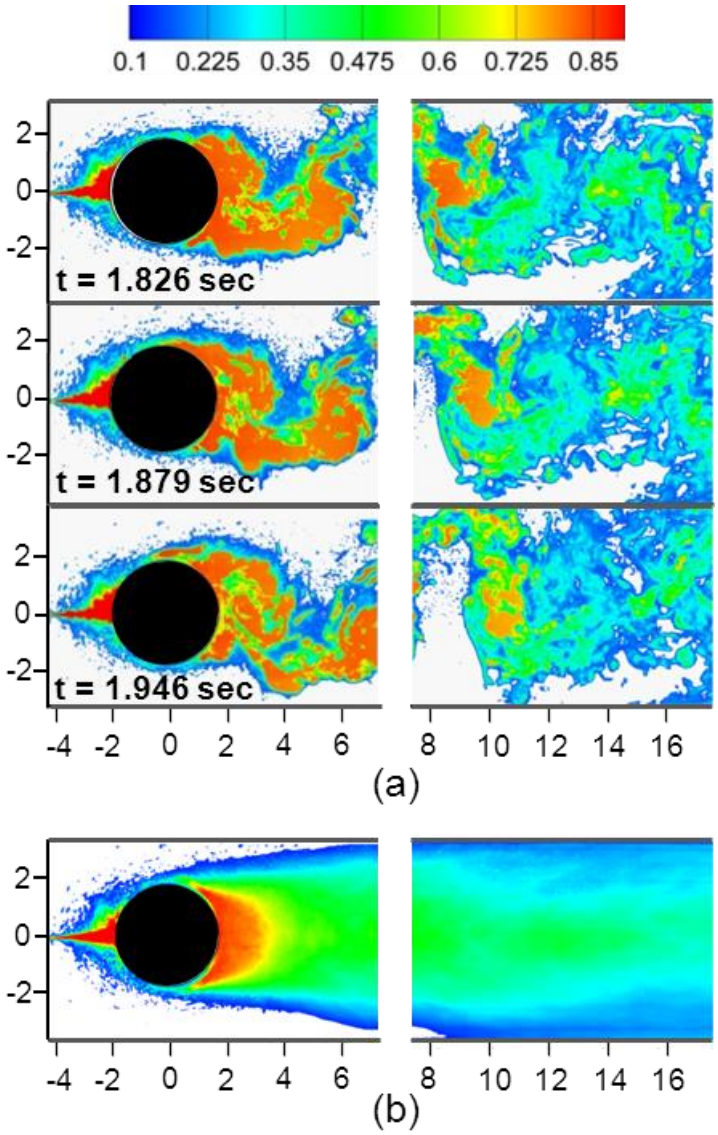

Figure 4.2: 2D visualization of (a) instantaneous dye movement (0.12 sec) and (b) time-averaged concentration contour for the dye injected at the center. Low concentrations (less than 10% of maximum concentration), depicted as white, were cutoff. The gray outlines represent the walls of the UV reactor.

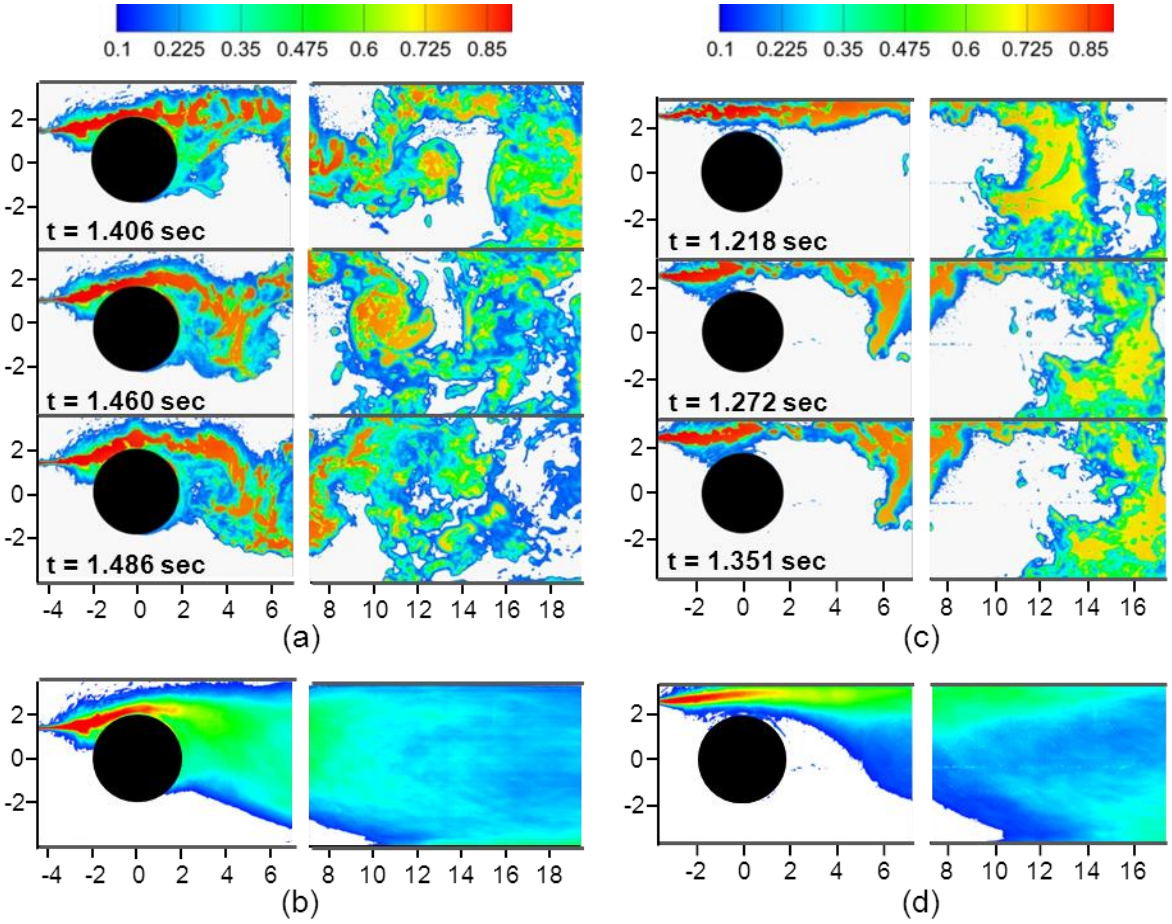

Figure 4.3: 2D visualization of (a) instantaneous dye movement (0.08 sec), (b) time-averaged concentration contour for the dye injected 1.3 cm off-center and (c) instantaneous dye transport (0.13 sec), (d) time-averaged concentration contour for the dye injected 2.5 cm off-center.

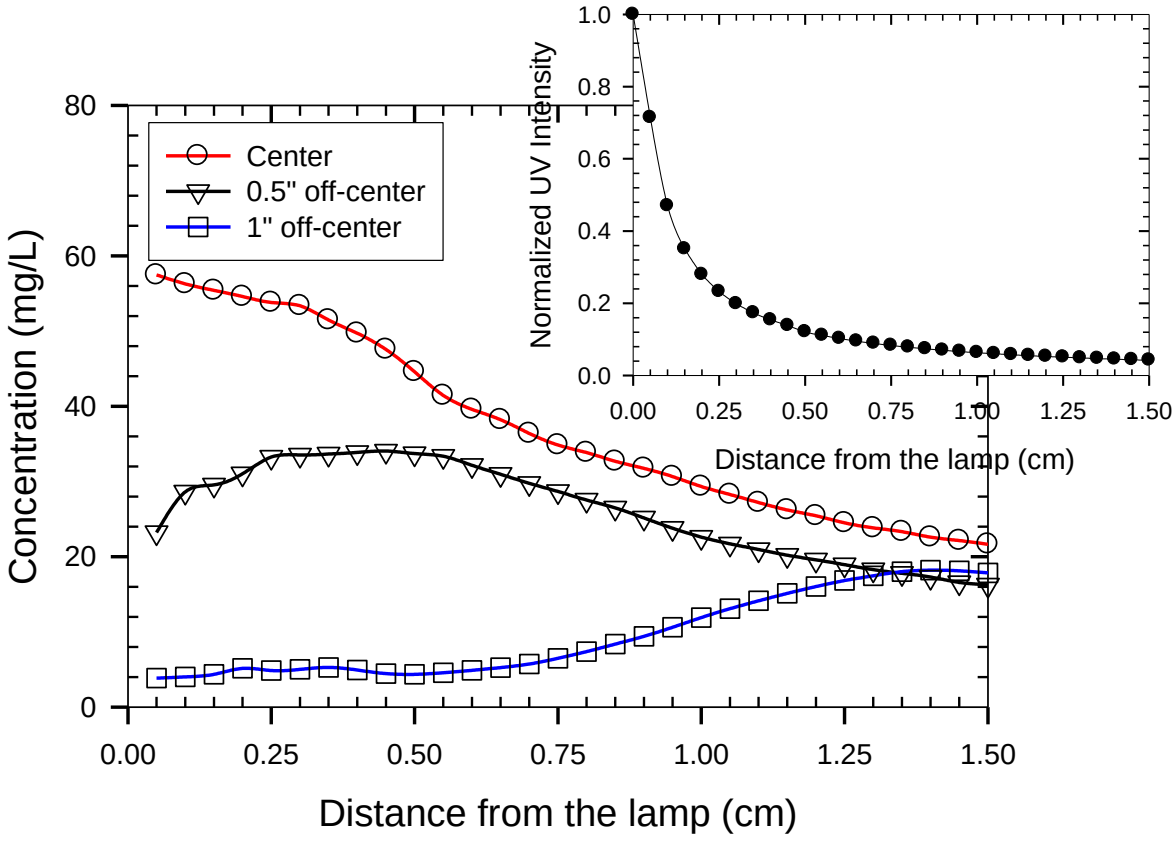

Figure 4.4: Dye concentration as a function of radial distance from the quartz sleeve surface for the various injection cases and (inset) normalized UV intensity changing with increasing distance from the lamps surface.

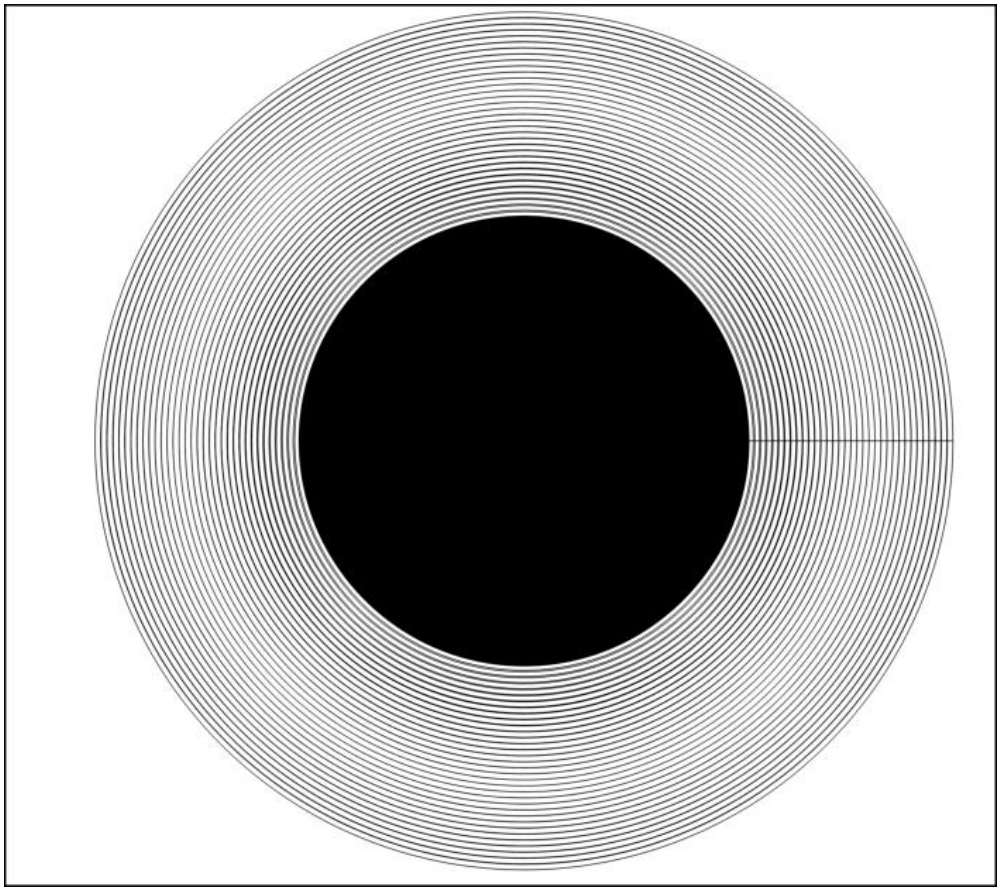

Figure 4.5: Example of the circular meshing to extract conservative tracer test data.

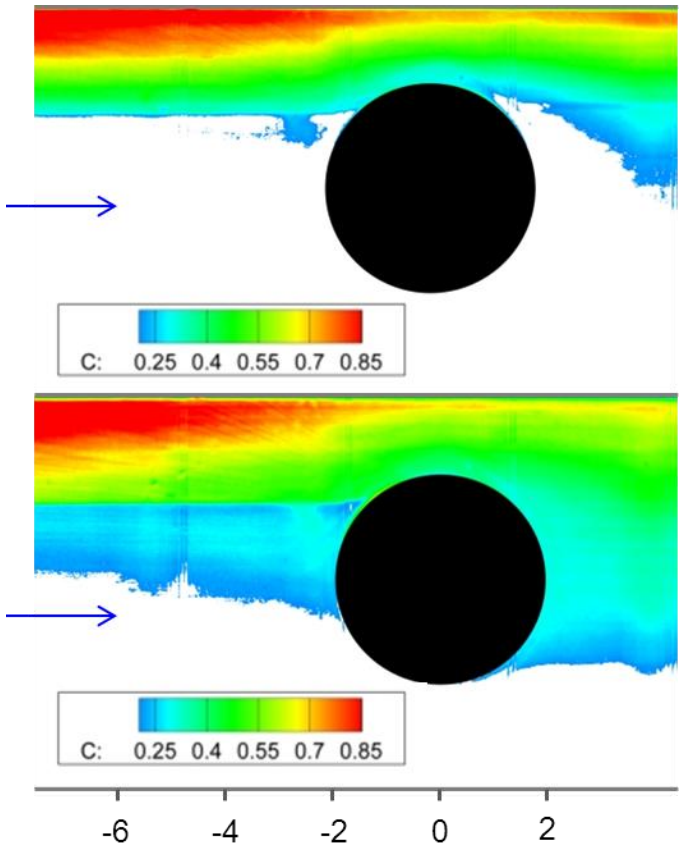

Figure 4.6: LIF images around the sleeve showing the extent of dye dispersion versus distance of injection at (a) 22.9 cm and (b) 32.4 cm upstream of the lamp.

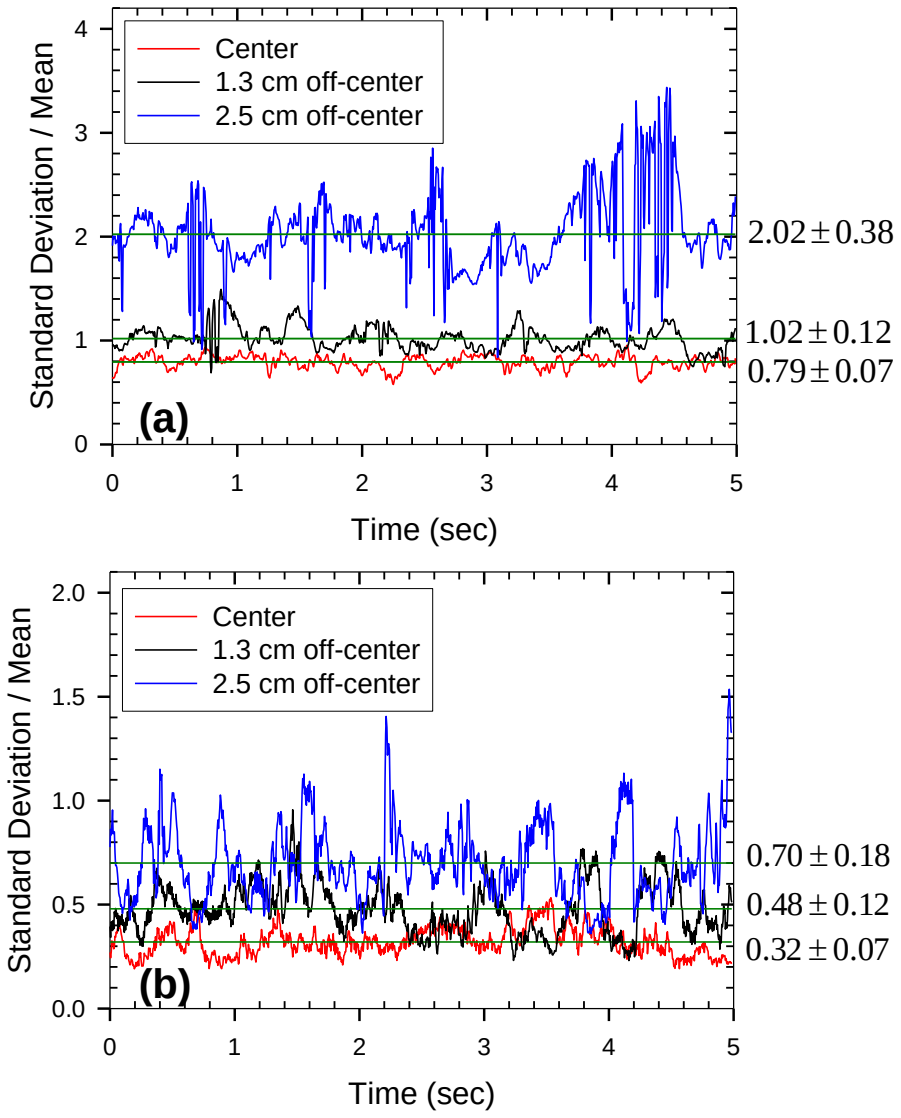

Figure 4.7: Changes in COV of dye concentration through the cross section of the (a) wake region and the (b) outlet over time.

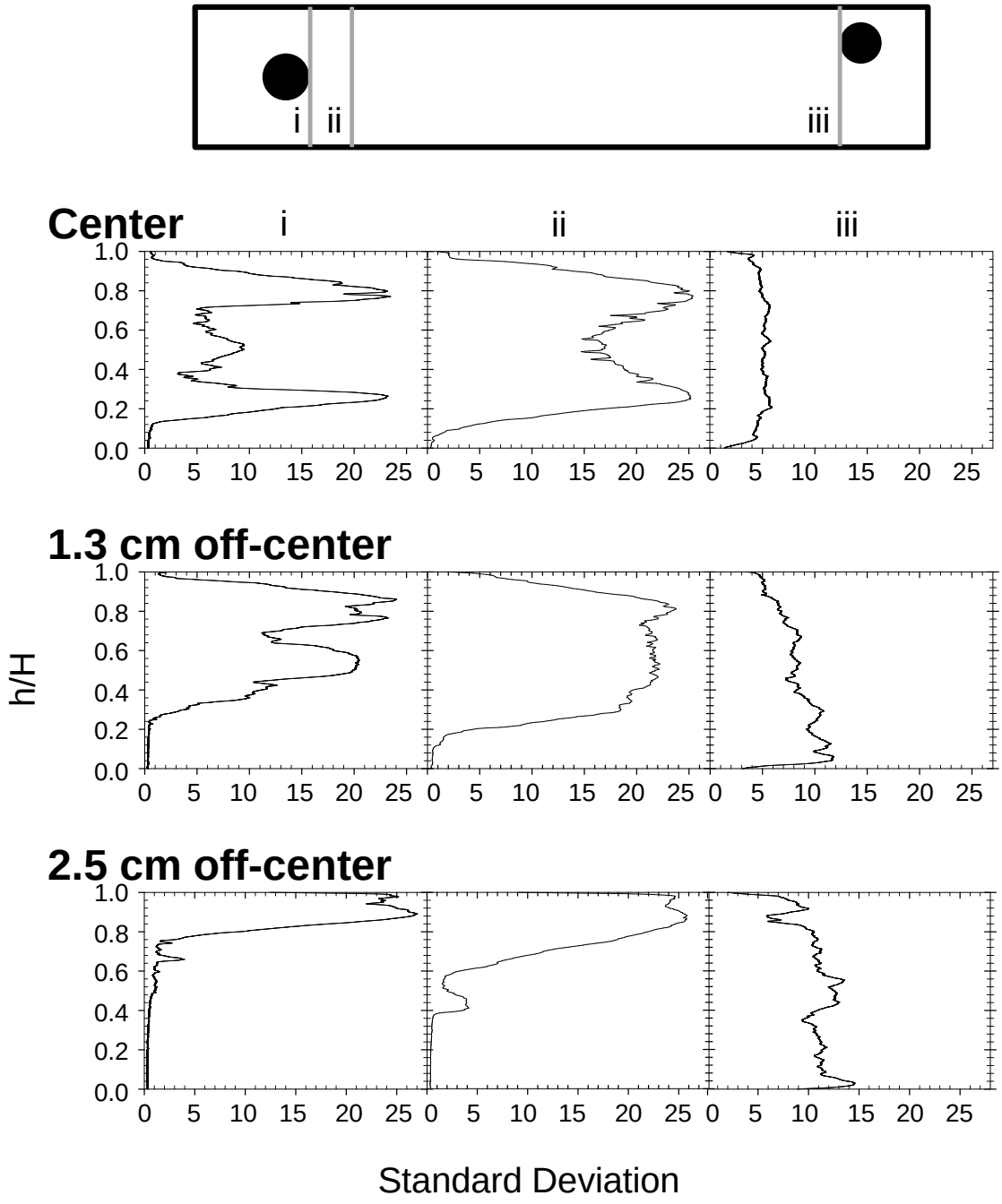

Figure 4.8: Standard deviation of tracer dye concentration at multiple line sections in the UV reactor comparing dye mixing for the various injection heights.

CHAPTER 5.

CONCENTRATION BASED DECOMPOSITION OF THE FLOW AROUND A CONFINED CYLINDER IN A UV DISINFECTION REACTOR

5.1. INSTANTANEOUS AND TIME-AVERAGED FLOW AND TRACER CONCENTRATION

The type of flow investigated in this study has become of great interest to the UV disinfection industry. As a result of the confinement, the Strouhal number, *St*, was found to increase when a cylinder is placed near a plane wall (Price et al., 2002). Typical values of the Strouhal number for the flow in an infinite domain at $Re = 4{,}900$ are $0.18 \leq St \leq 0.22$ (Hirota et al., 2008). In the present study, the Strouhal number, found from a Fast Fourier transform (FFT) of the transient dye concentration (Figures 5.1a and b) and the velocities (Figure 5.1c) at a point 1.5 cm ($x/D = 0.8$) downstream of the edge of the cylinder, is calculated to be 0.28 based on the free stream velocity and 0.18 based on the increased velocity in the gap. In the flow around a circular cylinder, the streamwise velocities always fluctuate between negative and positive in the wake region (Franke et al. 1990). However, dye concentrations, attained from light intensities, are always positive and thus the frequency from the concentrations should be twice that from the velocities. The peak frequency for LIF (Figure 5.1a) and RRLIF tracer images (Figure 5.1b) is observed to be exactly two times the peak of the streamwise velocity field; hence, $St = 0.28$ based on the free stream velocity and 0.18 based on the increased velocity in the gap.

Very few experimental studies have focused on this flow, one at very low *Re* ($\leq$ 250) (Rehimi et al., 2008) and another at very high *Re* (= 140,000) (Braza et al., 2006). In these studies, the *St* and confinement ratio were found to be 0.23 and 0.33 at the lower *Re* and 0.21 and 0.208 at the higher *Re*, respectively. The difference in the *St* can be attributed to the greater confinement ratio in the channel used in this study. The greater confinement causes a velocity increase by a factor of 1.6, thus increasing the vortex shedding frequency.

Figure 5.2 presents time-series images, spanning 0.12 s, depicting the two-dimensional instantaneous velocity vectors (Figure 5.2a) and the corresponding tracer concentration contours (Figure 5.2b) around the cylinder obtained with PIV and LIF techniques, respectively. The velocity field images plot one in four vectors to clearly depict the flow. The tracer concentration is normalized by the initial dye concentration, i.e. the concentration at the dye injector. Regions with concentration below 10% of the initial concentration are blanked out. The cylinder is represented as a black circle in all images.

These instantaneous images visualize the two main characteristics of the flow around a cylinder: the unsteady recirculation zone behind the cylinder and the occurrence of von Karman vortex shedding (Williamson, 1996; Hirota et al., 2008). The presence of the cylinder creates a low pressure zone behind it, causing fluid to enter the unsteady recirculation zone from the one side of the cylinder (Figure 5.2) to fill up this region and thereby creating a rotating vortex. At the next instant, a vortex on the opposite side of the

lamp forms (not shown) rotating in an opposite direction into the wake region and causing a release of the first vortex, which in general terms is called vortex shedding. The released vortex begins to grow in size as a new vortex is simultaneously created and shed, thereby the cycle continues (Hirota et al., 2008).

The time-averaged velocity field (Figure 5.3a) illustrates that majority of the flow vectors point in the stream-wise direction due to the confinement; however, flow separation and recirculation behind the cylinder are also observed. Asymmetry in the time-averaged flow field was clearly observed resulting from the non-uniform approach velocity profile (shown in Figure 5.4). The asymmetric approach flow resulted in only one recirculation vortex in the upper half of the region immediately behind the cylinder. The mean vorticity field (Figure 5.3b) indicates significant shear along the top and bottom of the cylinder and it rapidly decreases in magnitude behind the cylinder. The mean tracer concentration for the LIF (Figure 5.3c) and RRLIF (Figure 5.3d) images are very similar except that the small scale turbulent fluctuations are smoothed out in the reduced resolution image as expected. The images show that the dye that is introduced upstream of the cylinder, spreads vertically marginally and disperses as the magnitude of the normalized concentration decreases in the streamwise direction (white being the highest concentration and dark grey being the lowest concentration). Even though the time-averaged flow field is asymmetric with respect to the channel centerline, the distribution of normalized concentration appears to be symmetric. This could have important consequences for the UV disinfection process and suggests that the inflow velocity profile do not affect the behavior of pathogens around the UV lamps.

Figure 5.4 plots vertical streamwise velocity (Figure 5.4a) and concentration profiles (Figure 5.4b) at selected locations along the test section. The streamwise velocity profile is depicted at the upstream and various normalized distances (*x/D*) downstream of the cylinder while the concentration profile is only plotted downstream of the cylinder. The velocity profile at the inlet of the test section (labeled 'upstream') has some similarities to a turbulent velocity profile, but differences exist. The non-uniform flow is a result of the upstream configuration of the experiment that was built to analyze the flow in a UV reactor. The velocity profiles observed downstream of the cylinder are typical of the flow cylinder interaction. As a result of flow separation and vortex shedding, a wake region is formed, in which the streamwise velocities are reduced. As an effect of the flow confinement, higher streamwise velocities are observed in between the cylinder and the wall. Further downstream of the cylinder, at $x/D = 2.29$, the velocity profile slightly recovers, however, still shows the presence of a wake.

In contrast to the velocity profile, the normalized dye concentrations increases and is fairly uniform immediately behind the cylinder; however, it drops greatly when approaching the walls. Further downstream of the cylinder, the normalized concentration profile exhibits a distinct peak along the channel centerline, which is a result of vortices entraining the tracer into the wake. Near the walls, the concentration profile is close to zero. This occurs as a result of the high momentum of the fluid that does not give sufficient time for the dye to diffuse to the walls and a small lateral turbulent diffusion

coefficient. Finally, unlike the velocity profile, at x/D = 2.29, the concentration profile is not uniform; on the contrary, the peak is most distinct.

5.2. ENERGY FRACTION AND CUMULATIVE ENERGY

Since POD characterizes the contribution of each eigenvalue to the total energy, the energy fraction per mode (Figure 5.5a) and the cumulative energy sum (Figure 5.5b) are plotted for the PIV images (captured in 25 and 5 s at 200 Hz), vorticity (captured in 5 s at 200 Hz), LIF (captured in 5 s at 200 Hz) and RRLIF. The results from the PIV images captured in 25 s are compared with those captured in 5 s taken from the same experiment to determine the effect of sample size necessary for convergence on the POD results. Figure 5.5 shows minor differences in the energy captured per mode between the different datasets; the eigenvalues vary the greatest in the first two modes (total of 44.2% and 42.5% for the first two modes of the 25 s and 5 s dataset, respectively) and then converge after approximately 20 modes.

Feng et al. (2011) and Perrin et al. (2007) performed POD analyses of the velocity vectors for the near wake flow past an isolated cylinder at Re = 950 and 140,000, respectively. In both cases, the first few modes occupied most of the energy, similar to this study. At Re = 950, the energy contained in the first mode varied from approximately 10 to 40 % and in the second mode from approximately 10 to 20 % for different cases by changing the excitation frequency of the synthetic jet placed at the back stagnation point to bring symmetric perturbations upon the flow around the cylinder. In addition, a fairly

steady decrease in the energy contained as the modes increased was observed (Feng et al. 2011). At the higher *Re*, approximately 35% and 25% of the energy was contained in modes 1 and 2 respectively and the reduction in the energy contained between modes 2 and 3 was far more drastic, by approximately 80% (Perrin et al. 2007). In comparison, the results of the current study show a similar amount of energy contained in modes 1 and 2 (23% and 20% respectively). Furthermore, a significant reduction in the energy fraction between modes 2 and 3, approximately 75%, is also observed in this study. Thus, even though the energy captured by the individual modes are not matched, similarities in the decrease in energy contained are observed in the energy fraction per mode for *Re* = 4,900 (current study) and 140,000 (Perrin et al., 2007). This indicates that at these *Re*, the small-scale turbulence was captured by the modes comparably. Subsequently, the dissipation of this small-scale turbulence also occurs in a similar manner.

Similar trends are also observed for the energy fraction per mode for vorticity, the concentration of LIF and the concentration of RRLIF. The energy contained in each mode rapidly reduces for the first several modes and then gradually decreases with each increasing mode number. The first two modes (approximately 12%, 13% and 18% for each mode in the vorticity field, concentration from LIF and concentration from RRLIF, respectively) contained significantly higher energy than each subsequent mode pair. Furthermore, in comparison to modes 1 and 2, the combined energy fraction of modes 3 and 4, is observed to be approximately 80% lower in the vorticity field and 50% lower in the concentration fields. Finally, the cumulative energy captured in the first twenty modes using LIF and RRLIF differ significantly (approximately 60% as opposed to 75%) while

that using PIV is very similar (approximately 64% and 66%). Hence greater differences in the energy captured in the first twenty modes between LIF and RRLIF techniques but very minor differences between the PIV of images captured in 25 s and 5 s are observed. The first few modes in RRLIF have significantly higher energy than the corresponding LIF modes while that trend gradually reverses as the mode number increases. The differences in the LIF and RRLIF modes occur due to averaging of the pixels that filters out the small scale turbulent scales.

5.3. UNCERTAINTY ANALYSIS

The number of modes generated by the application of POD to velocity, vorticity and concentration data is equal to the number of snapshots, *N*. Errors exist in the vector field and concentration measurements, thus reducing the number of reliable modes. A method to determine the threshold at which POD modes become corrupted by noise is presented by Epps and Techet (2010). This threshold criterion requires the root mean square (RMS) velocity of the mode to be greater than the RMS PIV measurement error as described by eq. (4.5).

$$s_k > \sqrt{DN} \cdot \epsilon \tag{4.5}$$

where s_k = square root of the energy in a given mode

D = total number of data points

ϵ = root mean square error of the velocity field measurements.

The root mean square error of this PIV experiment is estimated as $\epsilon_U = 0.1 \times pixel/\Delta t$ (Raffel et al., 2007) based on the velocity gradients. For 5000 images each with 2205 pixels, the POD modes become dominated by noise at the 46th mode, while the reliable modes increase slightly to 50 for 1000 images. The similarity in usable modes further validates the use of 1000 images as the introduction of more data does not improve POD performance.

Additionally, this error threshold technique can be applied to the vorticity and concentration data. The error in vorticity can be reduced by the method of calculation, but careful consideration must be taken not to excessively smooth the data, causing a reduction in the enstrophy signal. The uncertainty associated in the least squares derivative method is $\epsilon_\Delta = 1.0\epsilon_U/\Delta x$ (Raffel et al., 2007). When the error is appropriately propagated through the vorticity calculation, the uncertainty for the vorticity is $\epsilon_\omega = 1.41\epsilon_U/\Delta x$. The method used to calculate the vorticity in this study resulted in an RMS error, $\epsilon_\omega = 0.0176/\Delta t$. The threshold analysis for the vorticity reveals that the first 163 modes have signal strengths greater than the experimental noise. Another method to calculate vorticity is using the Stokes Theorem, which has a RMS error, $\epsilon_\omega = 0.0076/\Delta t$. Applying the Stokes Theorem to calculate vorticity is synonymous to applying a central difference scheme on a smoothed (3 × 3 kernel) velocity field (Raffel et al., 2007). The smoothing out results in reduced signal strength and only the first 13 POD modes were found to be above the noise threshold. Epps and Techet (2010) did not observe a change in the number of reliable modes with energy

above the noise threshold despite the filtering of data. This is a result of using the RMS error calculated for the unfiltered data and applying it to the filtered data. Without further detail on the smoothing spline method used by Epps and Techet (2010), it is not possible to identify whether this was the appropriate RMS error. Finally, the LIF system used in this study was found to have a RMS error, $\epsilon_C = 0.704 \frac{\mu g}{L}$ (Tian, 2002). The first 59 modes in the concentration based decomposition exceeded the noise threshold. The reduced resolution LIF had a RMS error, $\epsilon_{CR} = 0.125\epsilon_C$. Despite having similar shape and form to the full resolution LIF results, only the first four modes of the reduced resolution LIF were found to be above the error threshold.

5.4. POD EIGENMODES

5.4.1. Velocity based decomposition

Figure 5.6a shows the eigenvectors of modes 1 and 2 for the POD of a 2D velocity field captured in 25 s at 200 Hz. It is assumed that the third dimension of the velocity is negligible and does not affect the POD results. These modes capture the recirculation zone and the vortex shedding behind the cylinders. In mode 1, the vortex observed in the wake region rotates clockwise while the second vortex detected further downstream rotates counter-clockwise. Similar vortices are identified in mode 2, however, with the opposite rotation. In both modes, the core of the coherent structure identified in the wake region occurs between x = 2 and 4 cm (corresponding to x/D = 0.5 and 1) and is observed to be smaller in size than the cylinder diameter. In comparison with the time-averaged recirculation zone (Fig. 3a), the vortices appear similar in height, but smaller in width.

The second vortex, formed downstream of the wake region, appears between x = 6 and 8 cm (corresponding to x/D = 1.5 and 2) and has a similar size as the cylinder. However, at Re = 140,000 and a confinement ratio, D/H = 0.208, Perrin et al. (2007) observed the formation of only one vortex in mode 1 with its core at x/D = 1 and two counter-rotating vortices in mode 2 with their centers occurring between x/D = 0.5 and 1 and x/D = 1.5 and 2. The disparity in mode 1 can be attributed to the greater confinement in the test section and the lower Re used in this study. Subsequent modes do not clearly identify any coherent structure, hence they are not shown.

The decomposition analysis of velocity images captured in 5 s at 200 Hz (Figure 5.6b) clearly depicts the vortex shedding behind the cylinders even though the rotation of the vortices is switched. This is merely an artifact of the images selected. The position of the core of the first vortex is between x = 2 and 4 cm (corresponding to x/D = 0.5 and 1) and between x = 6 and 8 cm (corresponding to x/D = 1.5 and 2) for the second vortex. Thus, a POD analysis for a data set captured in 5 s is very similar to that of the larger data set in terms of the energy contained in each mode and the position of each vortex in each mode. However, the rotation of the vortices is shifted by half a cycle and thus the appearance of the vortices differs. This comparison provides confidence that with a data set captured in 5 s at 200 Hz, the POD results converge. Hence, POD analyses of vorticity and concentration field images captured in 5 s at 200 Hz should suffice and yield consistent results.

After the POD analysis was performed, instantaneous fluctuating velocity fields are reconstructed using a selected number of eigenmodes. Figure 5.7 presents the instantaneous velocity fluctuation field with corresponding reconstructed velocity fields using the first 2, 10 and 25 modes. Since the first two modes (in Figure 5.6) capture most of the energy, all reconstructed flow fields clearly show the coherent flow structures, i.e. the two counter rotating vortices. As expected, the greater the number of modes used for reconstruction, the more accurate the image as compared to the instantaneous.

5.4.2. Vorticity based decomposition

Figure 5.8 shows the decomposition of the calculated vorticity magnitudes, where modes 1 – 6 captures 32.2 % of the total energy with 24.2% of the total energy in modes 1 and 2. This energy capture is considerably lower than that captured in the POD of the velocity fields, in which modes 1 – 6 capture 53.7% with 42.5% of the total energy in modes 1 and 2. Nevertheless, modes 1 and 2 of the vorticity based decomposition precisely indicate the presence of the rotating vortices that were identified in the corresponding modes of the velocity field. These modes represent three counter-rotating vortices, where dark blue indicates counter-clockwise motion and red indicates clockwise rotation. The positions of the first two vortices in each mode coincide with those of their velocity-based counterpart, while the third vortex was not identified. In mode 1, the first vortex that forms in the wake region is smaller in size than the other two vortices, which are approximately the same size as the cylinder. In mode 2, a U-shaped vortex is formed immediately downstream of the cylinder.

Previously, Ma et al. (2000) performed vorticity based decomposition on Direct Numerical Simulation (DNS) and Large Eddy Simulation (LES) results for the flow around an isolated circular cylinder at *Re* = 3,900. They observed a similar trend in the energy contained per mode; most of the energy was contained in the first two modes, followed by a significant energy reduction between modes 2 and 3 and then a gradual decrease in the energy per subsequent mode. In addition, unlike at *Re* = 100, they observed that the modes do not appear in pairs since the energy contained in each mode pair was unequal. The vorticity eigenfunctions, obtained from 3D velocity field, for modes 1 and 2 identified the three vortices that were observed in Figure 5.8 in approximately similar positions. In addition, Konstantinidis et al. (2007) found that the first two modes in the cylinder wake at *Re* between 2100 and 2200 were symmetric across the centerline of the cylinder, thus representing anti-symmetrical velocity fields. They also concluded that the first two modes were associated with the basic wake instability. Hence, modes 1 and 2 represent the von Karman vortex (Feng et al., 2011). These conclusions are similar to those observed in the current study.

Modes 3 – 6 appear to be non-symmetrical due to the asymmetric approach flow condition. Contours of modes 3 – 5 indicate the formation of five smaller counter rotating vortices downstream of the cylinder corresponding to a reduction in the energy contribution by 80 – 85 % from these modes. Mode 6 clearly identifies the clockwise rotation into the cylinder wake at the top of the cylinder but vaguely depicts a similar complementary structure with the opposite rotation at the bottom of the cylinder attributed to the asymmetry in the approach flow. Thus, this mode identifies the boundary

layer formed around the cylinder. However, this layer was not observed in the velocity based POD modes.

Figure 5.9 plots an instantaneous vorticity field along with the reconstructed vorticity distributions using the first 2, 10 and 25 modes, respectively. Reconstruction using the first 2 modes captures the most energetic coherent structures, i.e., the counter-rotating vortices that represent the Karman vortex shedding. Similar conclusions were observed by Ma et al. (2000) and Perrin et al. (2007). Using the first 10 modes slightly blurs the dominant large scale features of the flow; however the general von Karman vortex patterns can still be identified. Using the first 25 modes, the patterns get less organized and begin to resemble the instantaneous image.

5.4.3. Concentration based decomposition

Figs. 4.10 and 4.11 present modes 1 – 6 for the LIF and RRLIF concentration based decomposition, respectively. The light and dark grey regions indicate entrainment of concentration into the cylinder wake from the top and the bottom of the cylinder respectively. The location of the dye injection played an important role in the POD results. Dye injected away from the centerline would not travel the same path as dye introduced at the center, thus resulting in different modes from those depicted in this study. However, since the objective of the paper was to compare the coherent structures between concentration images and velocity fields, the center injection approach was employed to clearly illuminate the characteristics of the flow in the wake region and the region downstream of the cylinder explicitly from the fluorescence of the dye.

Despite the reduction in resolution, both LIF and RRLIF modes depict similar features. Since the largest spatial concentration fluctuations at each instant are observed in the downstream regions where no dye was present, modes 1 and 2 represent these regions and hence contain the most energy. These structures exhibit symmetry about the cylinder centerline, thus resulting in a symmetric distribution of the tracer concentration behind the cylinder. Modes 3 – 5 capture the transport of the tracer by the vortices shed in the wake region while mode 6 represents the mass transport due to turbulence along the shear layer at the top and bottom of the cylinder.

Even though similar coherent structures are captured by LIF and RRLIF based decomposition, the major difference between these decomposition methods is that RRLIF images are much smoother than the LIF images. As mentioned before, RRLIF data is obtained by spatially averaging the LIF data, which automatically filters small-scale turbulent structures. Consequently, the magnitudes of the energy captured in the RRLIF modes differ from the energy captured from the LIF modes. For the RRLIF decomposition, the energy capture in modes 1 – 6 was 58% with 35% captured in modes 1 and 2, while for the LIF results, the energy content of modes 1 – 6 is 43.6% with 25.8% in modes 1 and 2. This is due to the fact that in the original data there is quite a bit of energy left in smaller scales that were filtered out in the RRLIF data. Hence, while RRLIF can predict well the large-scale features of the turbulence in the flow, it omits smaller scale and thus overestimates the energy contained in the larger scales.

Figure 5.12 plots an instantaneous concentration contour along with the corresponding reconstructed images using the first 2, 10 and 25 modes for the LIF based decomposition. Reconstruction using the first 2 modes captured the entrainment of the dye into the wake behind the cylinder, while that using the first 10 and 25 modes captured a greater amount of the details of the flow. The main entrainment process, through vortex shedding around the cylinder is captured using only the first 10 modes. Similar to the reconstructed vorticity distribution, when using the first 25 modes, almost the entire instantaneous flow is reproduced.

Finally, a comparison of the decomposition based on concentration was compared with that of velocity and vorticity. The vortices observed in modes 1 and 2 in the concentration based decomposition were neither identified by the velocity nor the vorticity decomposition. This discrepancy occurs because the velocity and vorticity decompositions are based on the analysis of vectors or particles that is present throughout the channel. However, the dye is only present in the region around the cylinder in the concentration decomposition, thus leading to large spatial concentration variations in the channel. The coherent structures identifying the shedding vortices in modes 3 – 5 of the concentration based decomposition are observed in both the velocity and vorticity decomposition as modes 1 and 2. The shedding vortices contains 20% and 15.4% of the energy for the LIF and RRLIF method, respectively, while approximately 43% and 24% in the velocity and vorticity based methods, respectively. However, these identified coherent structures agreed in size and location with those identified in the velocity and vorticity based decomposition. The transport along the wake shear layer observed in

mode 6 of the concentration decomposition is only partially identified in the vorticity decomposition and undetected in the velocity based method. Finally, the reconstruction of the velocity, vorticity and concentration based decomposition are almost completely captured within the first 25 modes.

5.5. CONCLUSION

This study applies the POD method on spatial tracer concentration data for the flow around a confined cylinder for the first time to successfully visualize coherent structures. This type of flow is of particular importance in the emerging field of UV disinfection, in which a UV reactor consists of a cylindrical lamp placed perpendicular to flow. In addition, these results are compared to their corresponding velocity-based and vorticity-based decomposition. The velocity-based decomposition was found to be identical for images captured in 25 s and 5 s at 200 Hz in terms of the energy contained in each mode and in the position of each vortex in modes 1 and 2 even though the rotation of the vortices were shifted by half a cycle. The velocity decomposition results demonstrate that only modes 1 and 2 identify useful coherent structures for the recirculation zone and the von Karman vortex shedding. For the calculated vorticity decomposition, modes 1 and 2 identify three counter-rotating vortices of size similar to the cylinder; modes 3 – 5 indicate five smaller counter-rotating vortices and mode 6 identifies the wake shear layer at the top of the cylinder.

Lastly, modes 1 and 2 in the LIF and RRLIF concentration decomposition represent the regions with the highest concentration fluctuations, i.e., where dye was not present;

modes 3 – 5 captured the shedding vortices downstream of the wake region and mode 6 clearly indicated the wake shear layer around the cylinder. Even though similar coherent structures are captured by LIF and RRLIF based decomposition, the major difference between these decomposition methods is that RRLIF images are much smoother than the LIF images. As mentioned before, RRLIF data is obtained by spatially averaging the LIF data, which automatically filters small-scale turbulent structures. Hence, while RRLIF can predict well the large-scale features of the turbulence in the flow, it omits smaller scale and thus overestimates the energy contained in the larger scales. The number of modes required in the reconstruction of the concentration images was lower than that for velocity and vorticity images.

The concentration based decomposition has advantages over the velocity or vorticity based decompositions. First, tracer concentration data are relatively easier to obtain in various types of flows such as in field experiments or major water bodies, where obtaining velocity field information is rather difficult. Secondly, since the dye tracer data is not interrogated over a window, unlike velocity fields, fine detail is retained, which was clearly observed in the difference between LIF and RRLIF decomposition. Thirdly, computational time is reduced as the raw images are directly used in the POD analysis. Furthermore, the concentration data, like vorticity, is one dimensional as opposed to the x and y velocity vectors, which further reduce analysis time. Lastly, reduced noise levels are expected as absolute concentration values are used, when compared to vorticity, where using derivatives amplify the errors. However, it should be noted that this method only works near the dye injection, where there is strong intermittency of the dye

concentration. Hence, in cases where coherent structures need to be determined over a fairly long distance whereby the dye would be completely mixed, multiple dye injections and image captures need to occur to reveal the coherent structures.

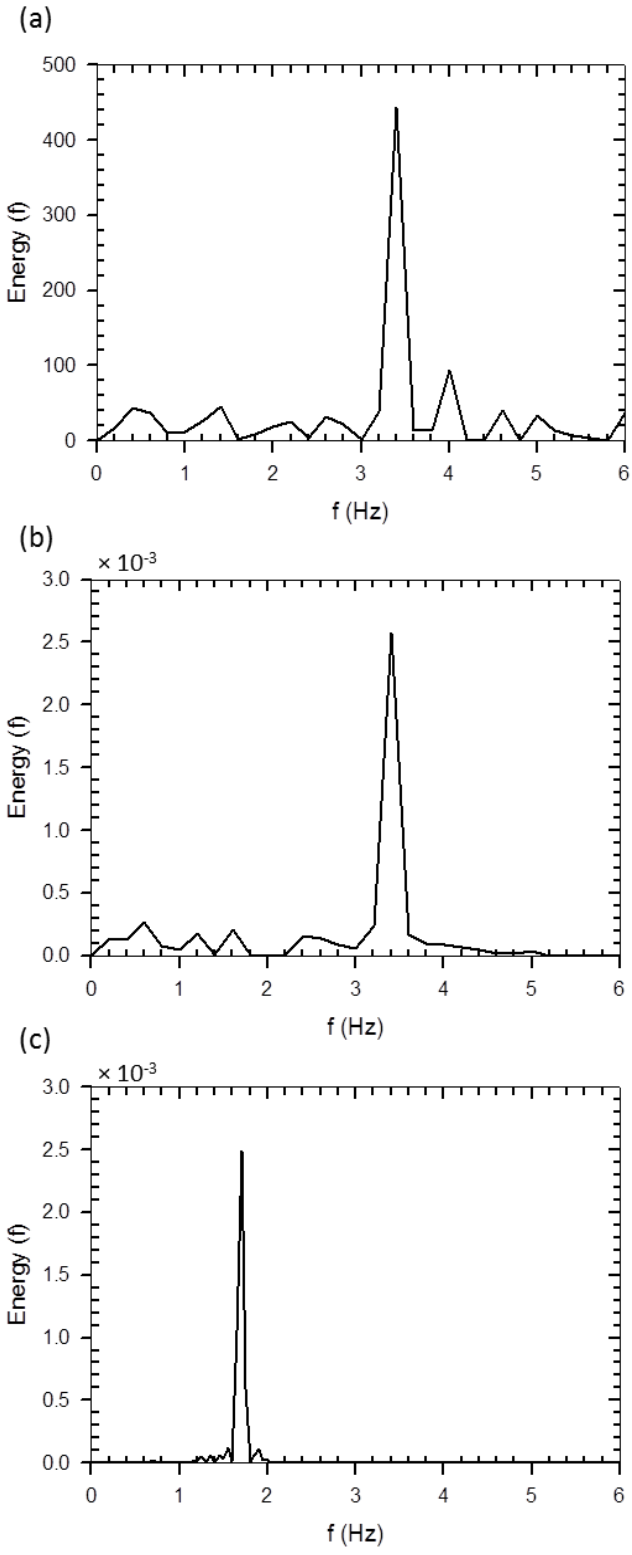

Figure 5.1: Energy spectrum at a point 1.5 cm downstream of the cylinder center for (a) LIF and (b) RRLIF concentration contour and (c) velocity field.

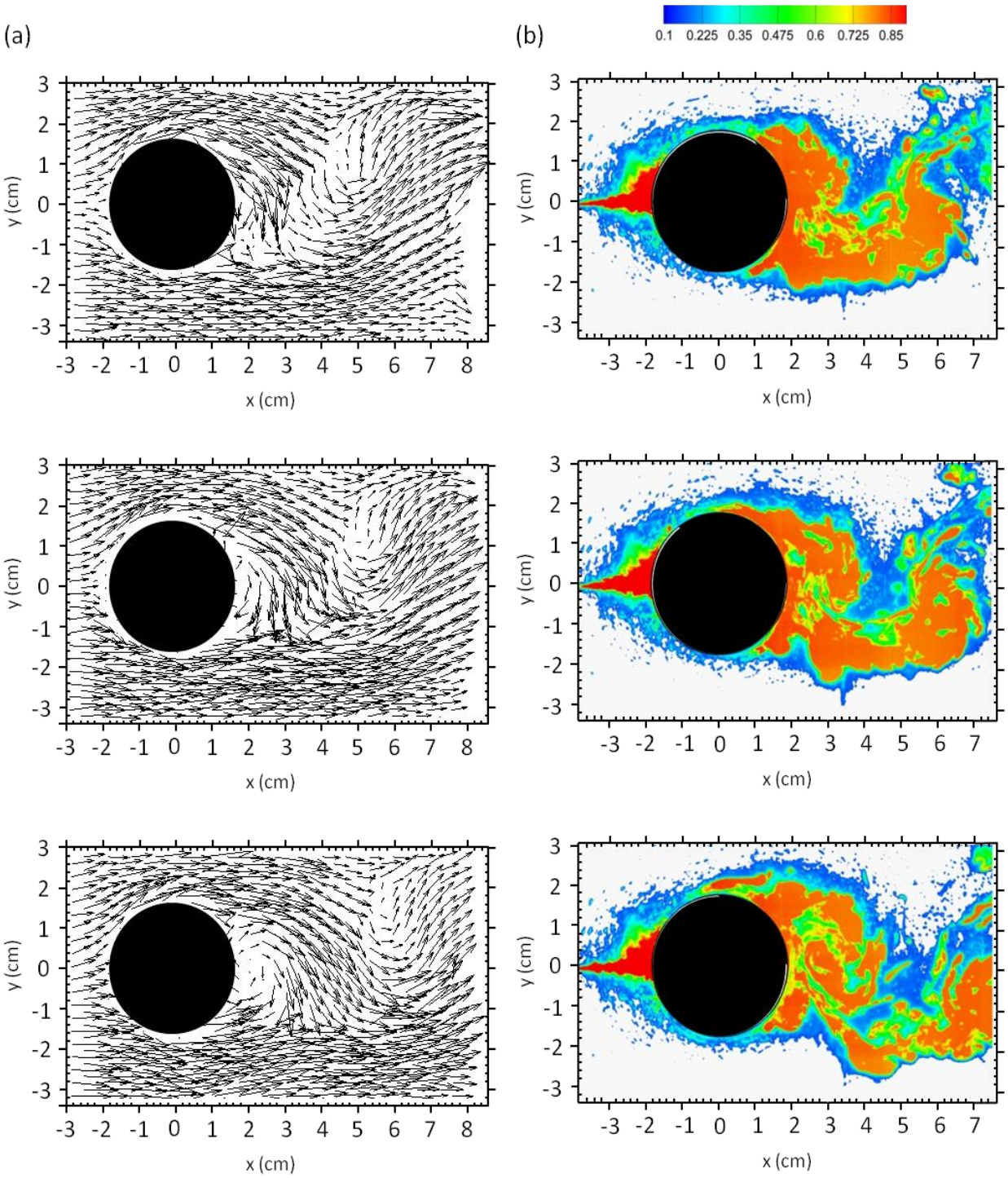

Figure 5.2: 2D visualization of the instantaneous (a) velocity fields and (b) normalized tracer concentrations over a period of 0.12 sec. Every fourth velocity vector, which was magnified three times, was plotted. Low concentrations (less than 10% of maximum concentration), depicted as white, were cutoff.

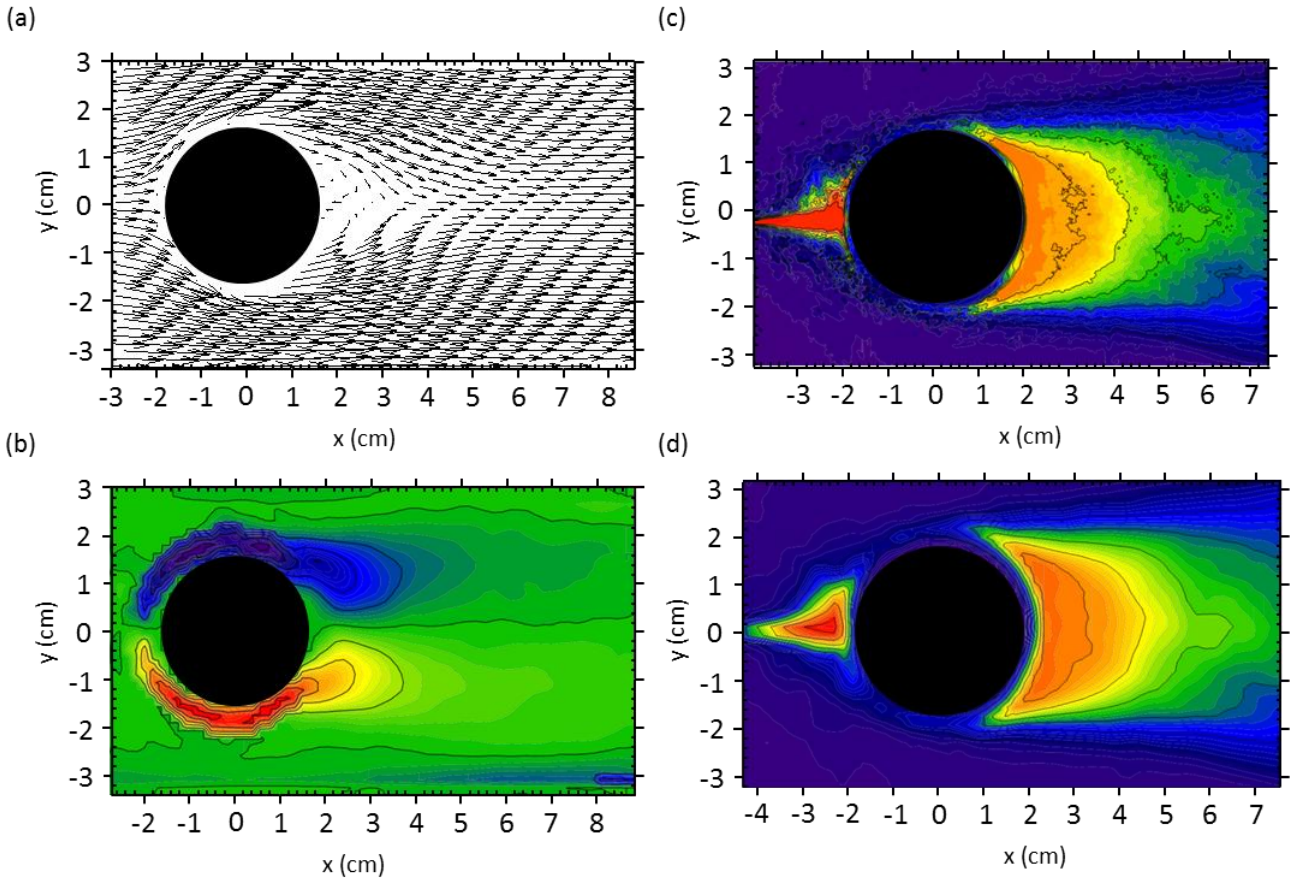

Figure 5.3: 2D visualization of the time-averaged (a) velocity vector field, (b) vorticity contours, (c) tracer concentration contours (LIF) and (d) reduced resolution concentration contours (RRLIF).

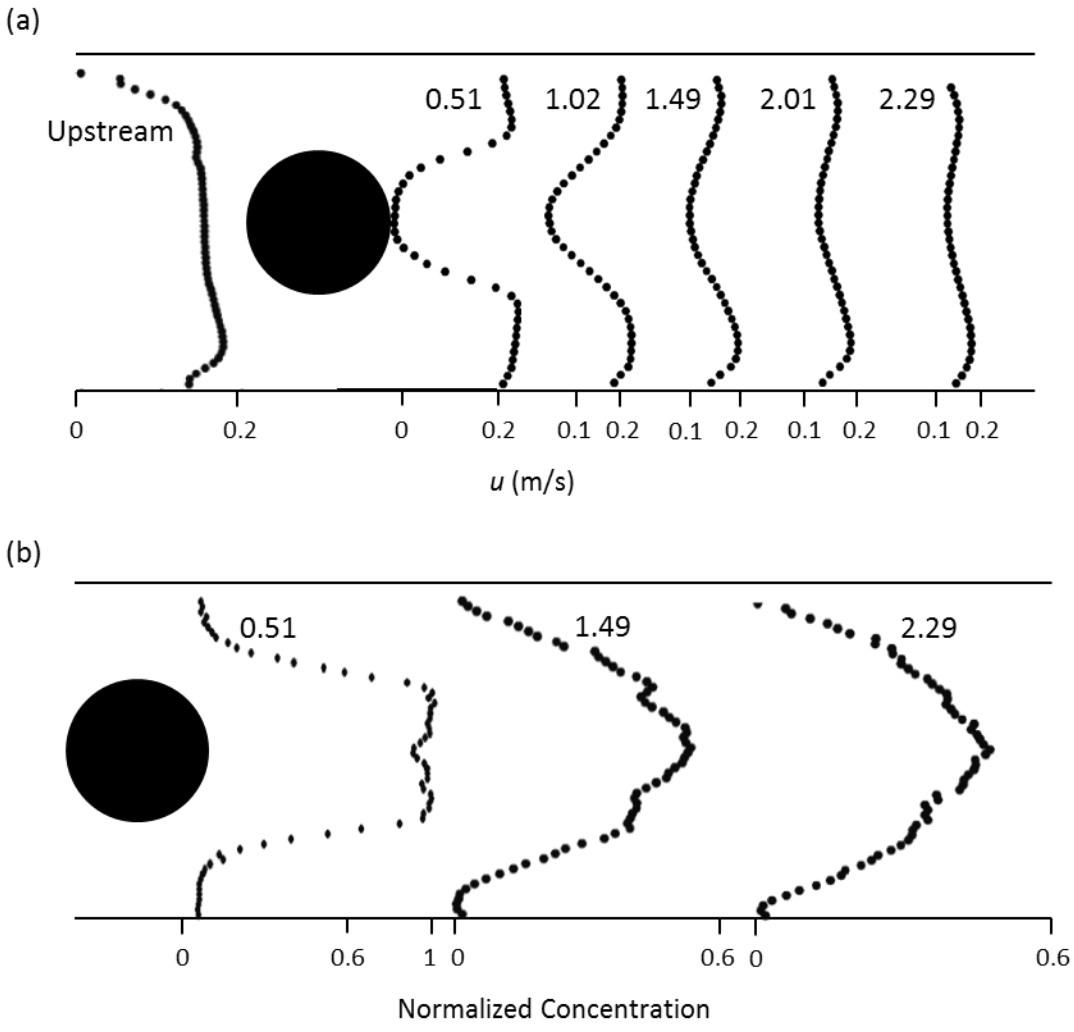

Figure 5.4: Time-averaged (a) velocity and (b) concentration profiles at various normalized distances (*x/D*) away from the cylinder center.

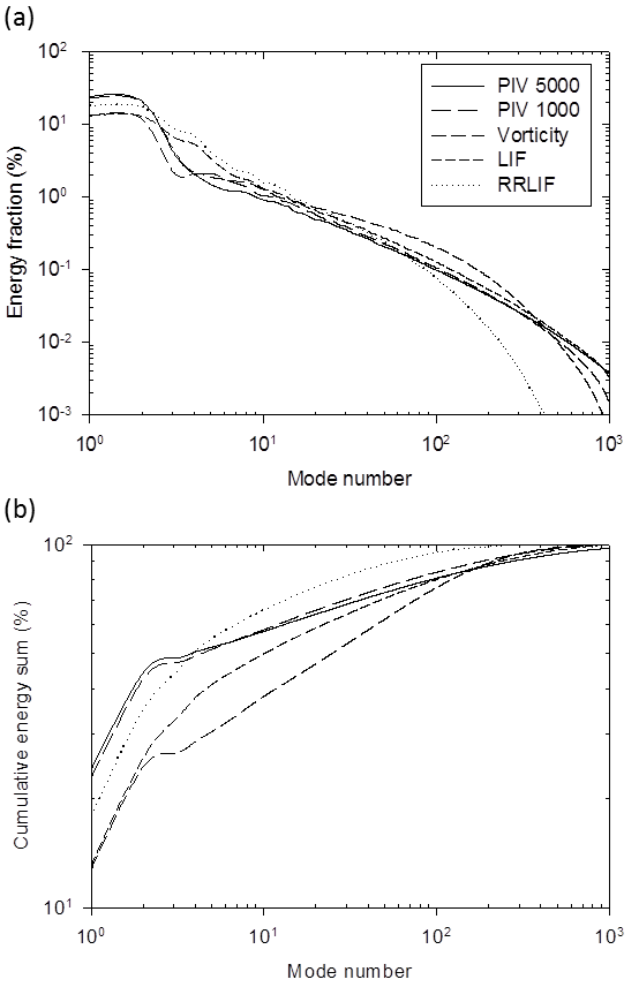

Figure 5.5: (a) Contribution of each eigenmode to the total energy (%) and (b) the cumulative energy sum (%) for the velocity fields obtained from datasets captured in 25 and 5 s, the non-modified (LIF) and the reduced resolution (RRLIF) concentration contour and the vorticity fields.

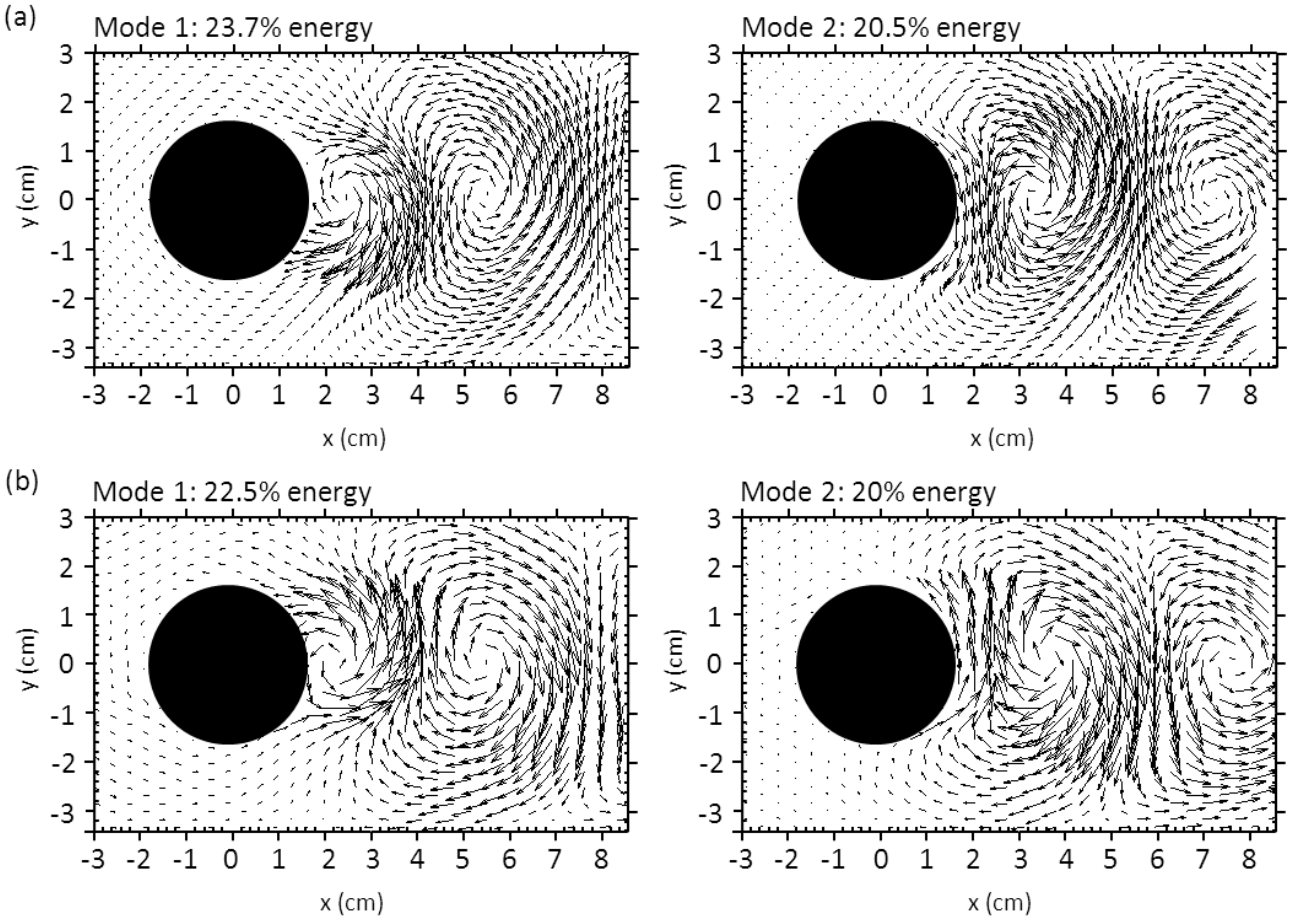

Figure 5.6: POD analysis of the velocity fields showing the first and second modes for (a) images captured in 25 s at 200 Hz dataset and (b) images captured in 5 s at 200 Hz along with the energy captured in each mode.

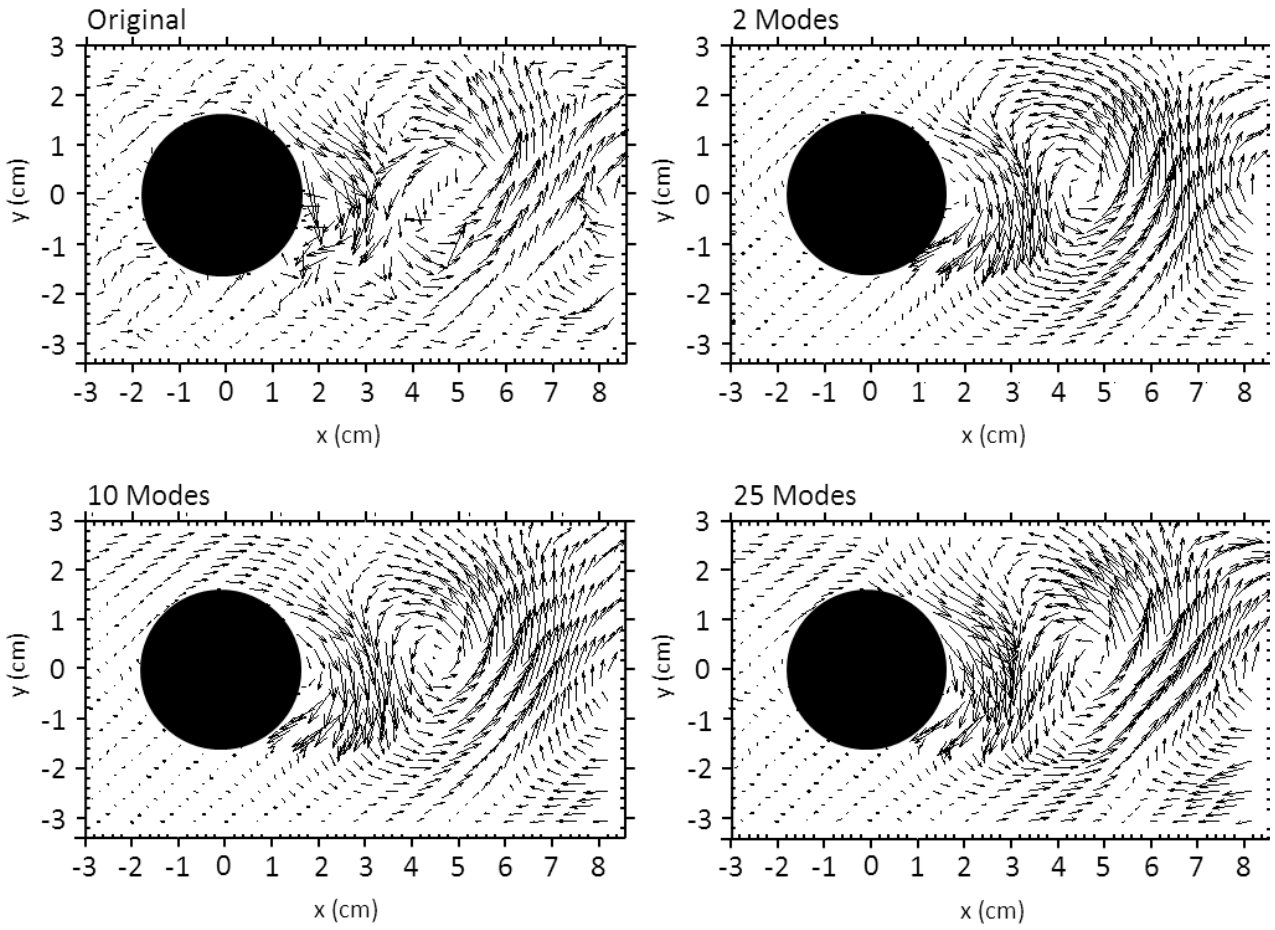

Figure 5.7: Reconstruction of the original instantaneous velocity field image using the first 2, 10 and 25 modes as indicated.

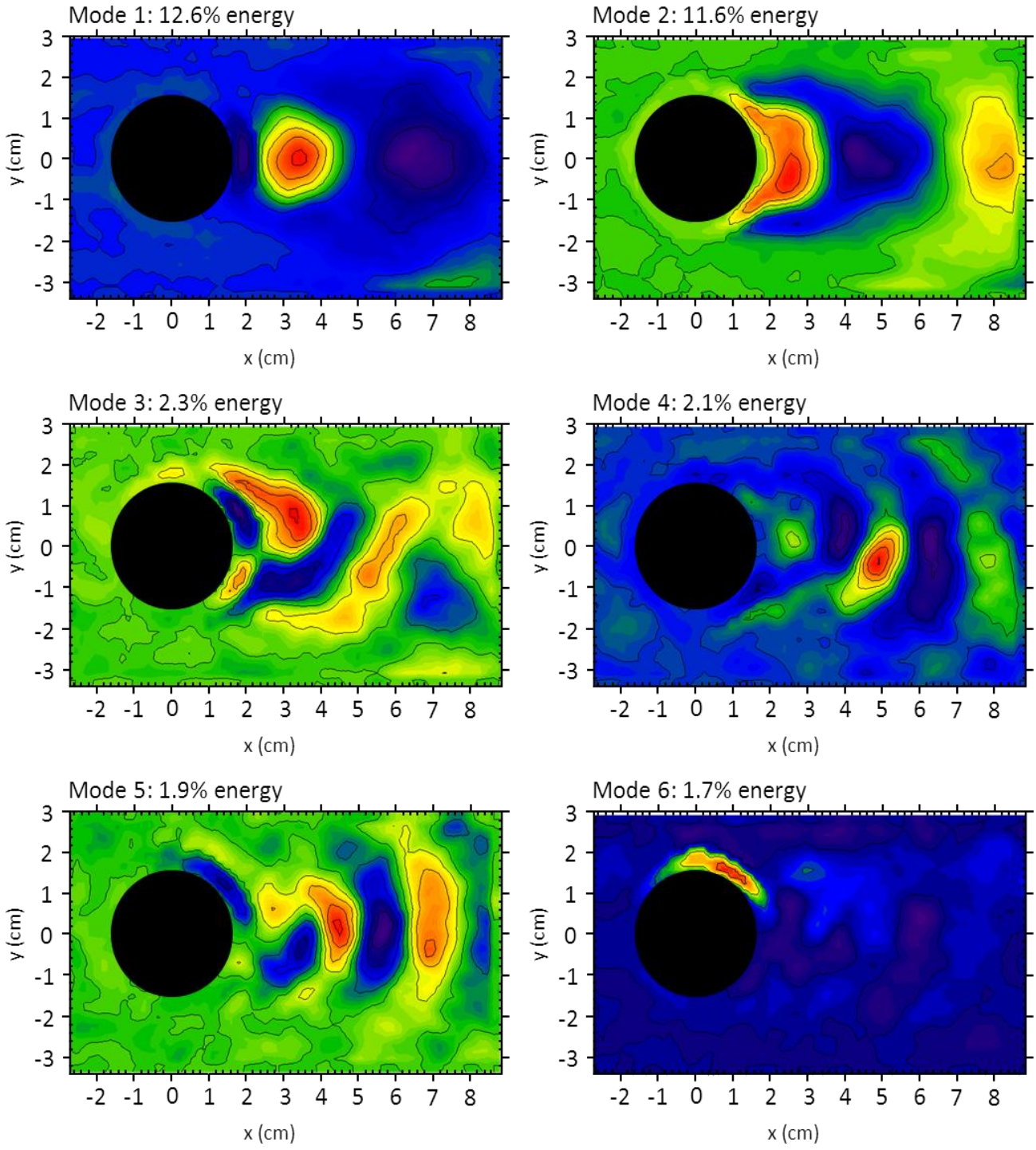

Figure 5.8: POD analysis of the vorticity field showing the first six modes along with the energy captured in each mode.

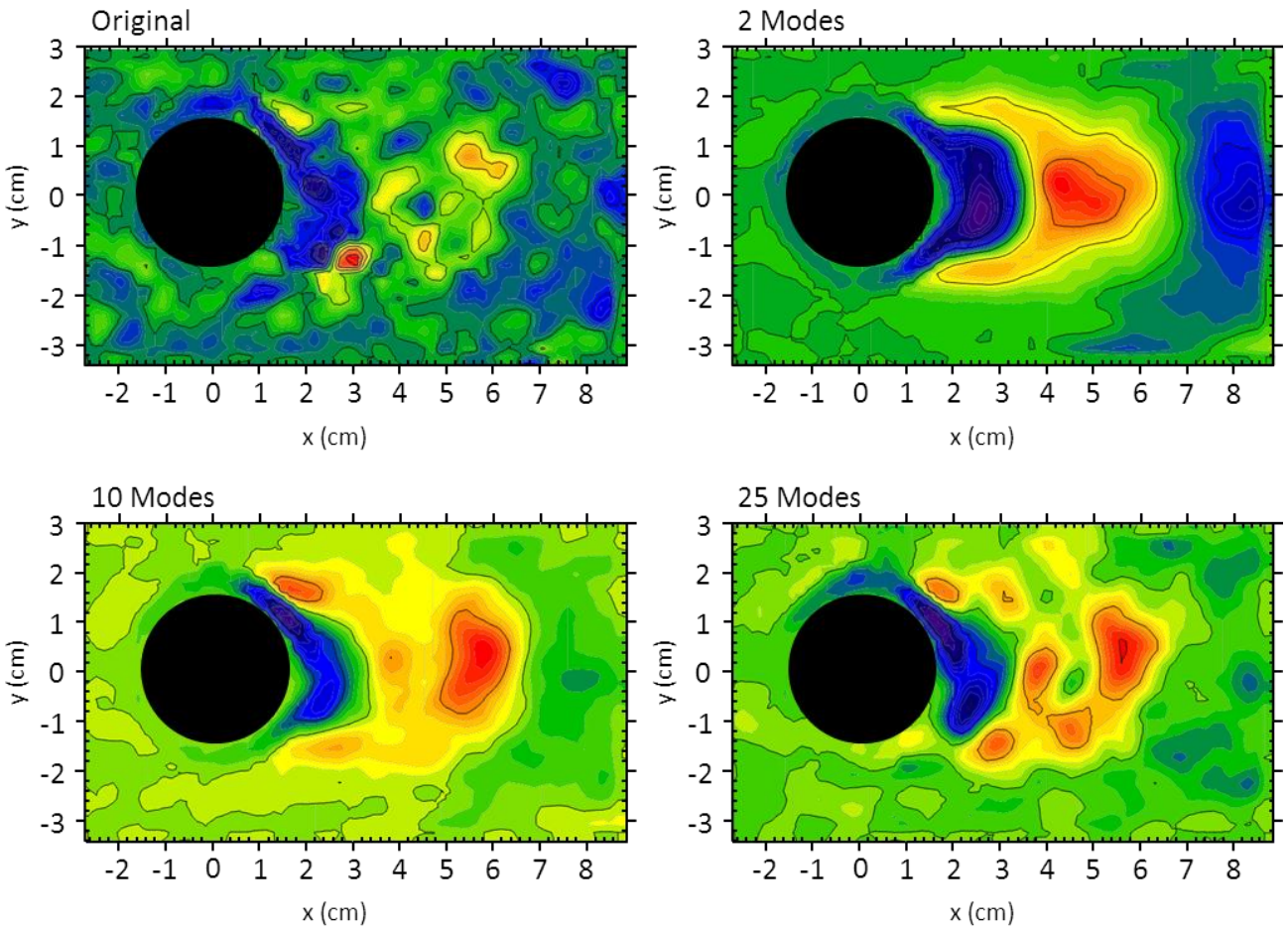

Figure 5.9: Reconstruction of the original instantaneous vorticity field image using the first 2, 10 and 25 modes as indicated.

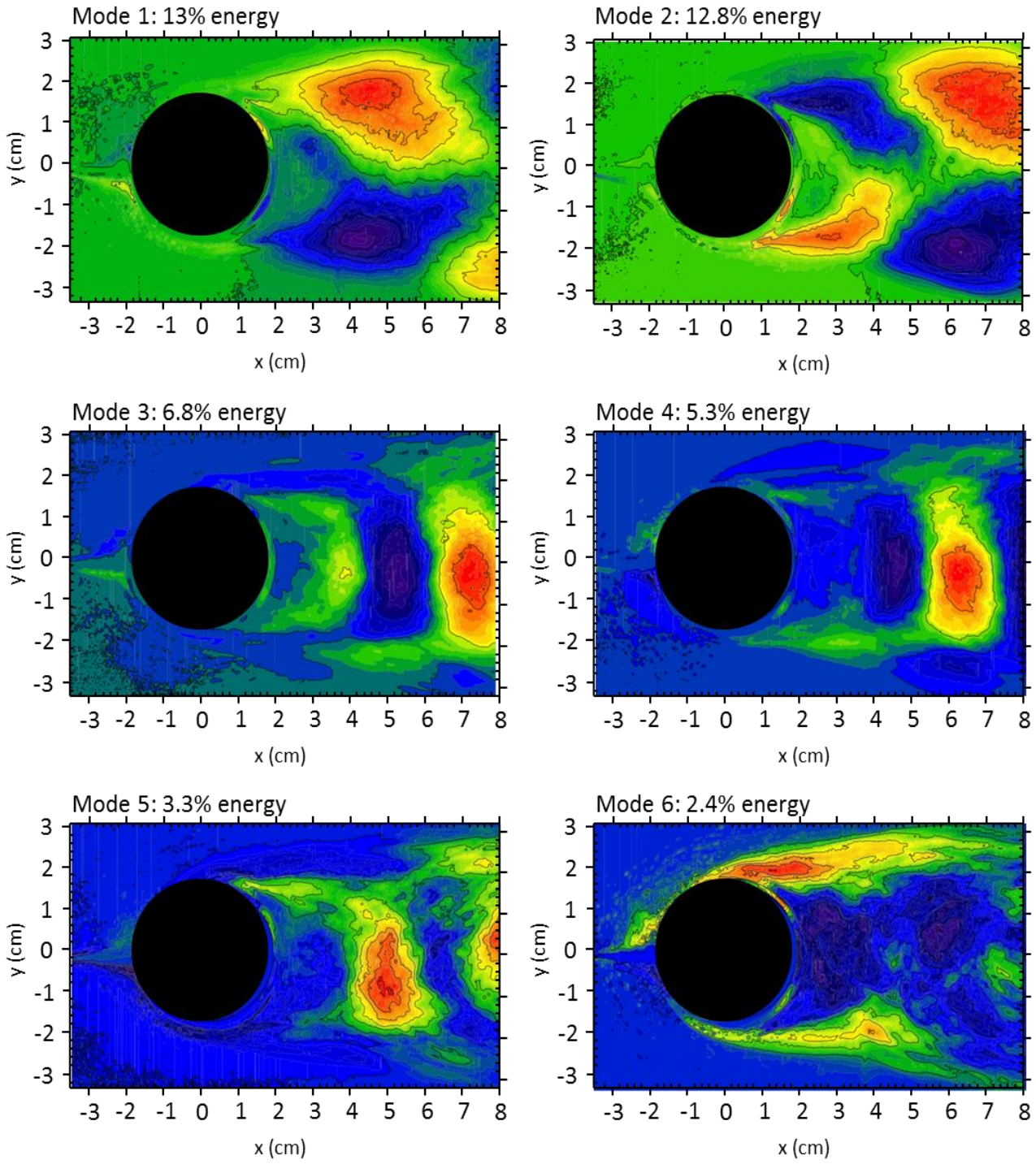

Figure 5.10: POD analysis of the non-modified concentration contours displaying the first six modes along with the energy captured in each mode.

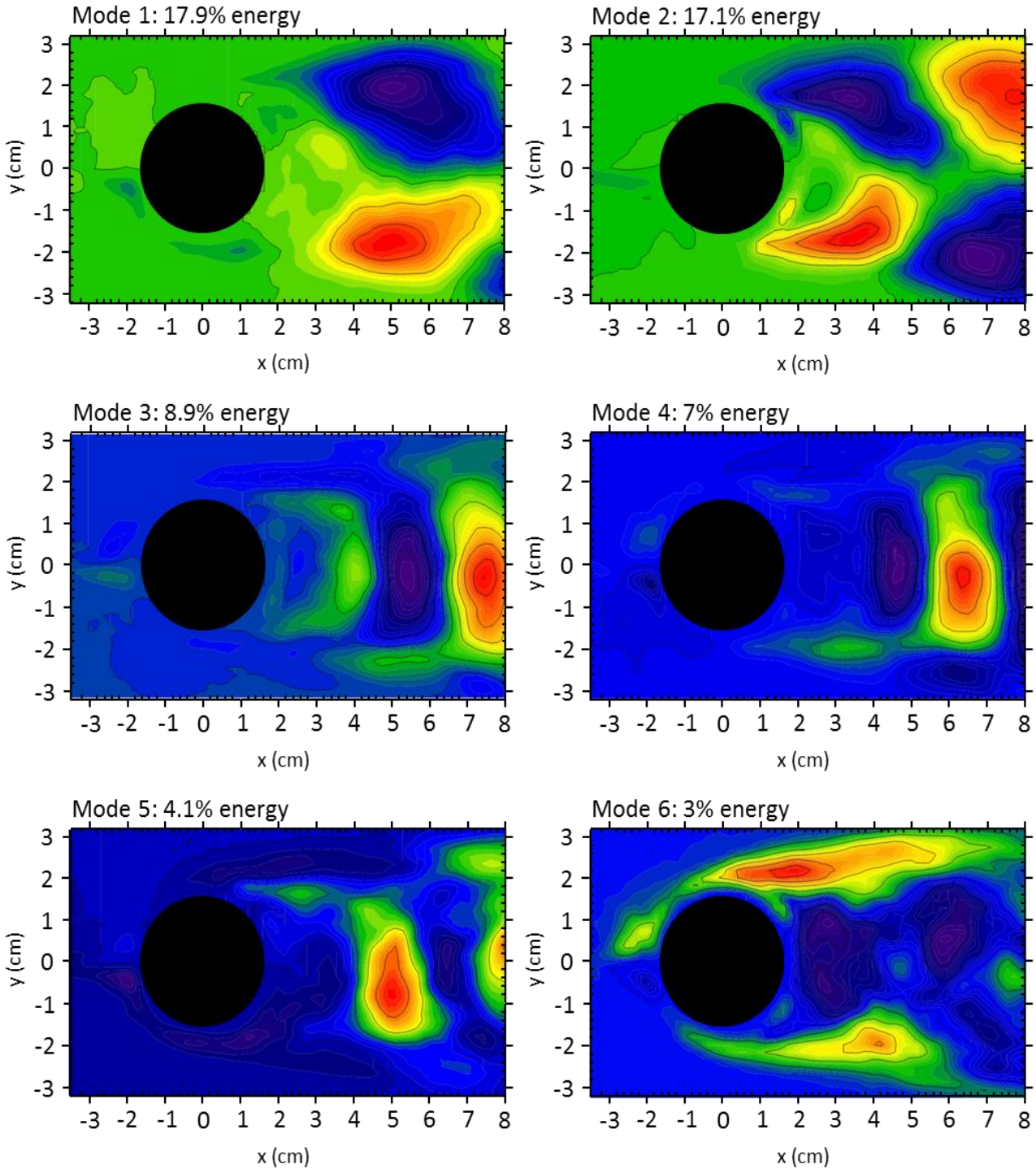

Figure 5.11: POD analysis of the reduced resolution concentration contours displaying the first six modes along with the energy captured in each mode.

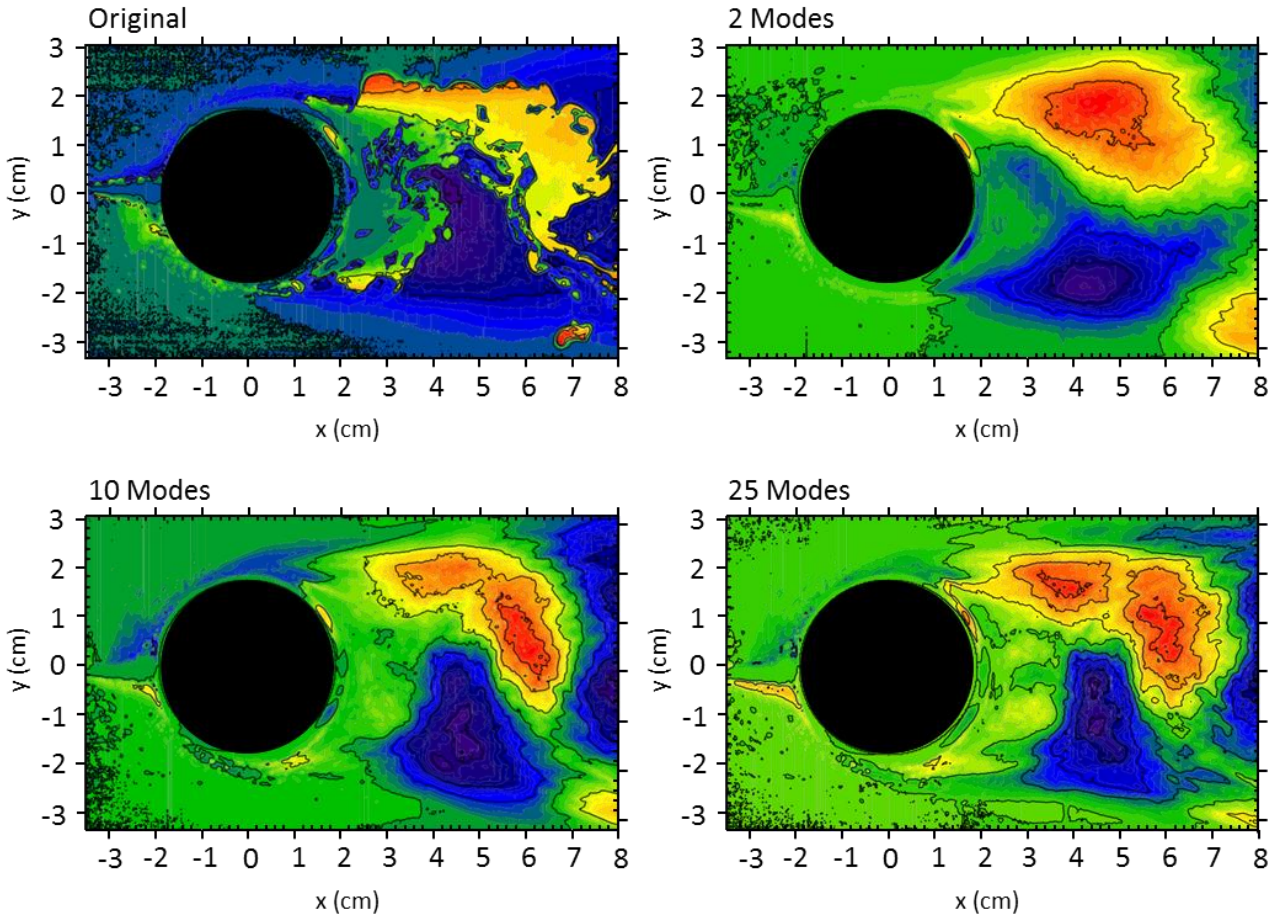

Figure 5.12: Reconstruction of an original instantaneous concentration image using the first 2, 10 and 25 modes as indicated.

CHAPTER 6.

UV REACTOR DOSE DISTRIBUTION VISUALIZATION AND QUANTIFICATION USING THREE-DIMENSIONAL LASER-INDUCED FLUORESCENCE

6.1. DYE DECAY KINETICS

The total rate of reaction of Rh6G during the application of UV/H_2O_2 is the sum of the rates of direct oxidation, direct photolysis and reaction with OH radicals. Figure 6.1 shows the decrease in the concentration of Rh6G versus *IT* (UV fluence: i.e., the average light intensity at 254 nm, *I*, in mW/cm^2, and exposure time, *T*, in s; Bolton and Linden (2003)) during the application of UV light and H_2O_2 at 0 and 2mM. When UV irradiation was applied without H_2O_2 or H_2O_2 applied without UV light, no Rh6G decay was observed. Hence, the dye decay kinetics was exclusively dependent on the reaction with OH radicals. When 2mM H_2O_2 was applied in the presence of UV light (1 mW/cm^2), the decay kinetics was characterized by a first order decrease in Rh6G concentration with respect to *IT*. Similarly, first order decay kinetics was observed for MS2 inactivation. The equations displayed in Figure 6.1 were obtained by fitting a linear curve through the origin and was used to convert dye degradation (C/C_o), obtained from the LIF experiments, to *IT* values and further to MS2 inactivation (N/N_o).

6.2. pH DEPENDENCE ON DYE DECAY KINETICS

No decay was observed when Rhodamine 6G, without H_2O_2, was irradiated under the UV light at all pH's. The decay kinetics and similarly the first order rate constant (*k*) of Rhodamine 6G increased as H_2O_2 concentration was increased (Figures 6.2 and 6.3) under UV irradiation. For example, in the dechlorinated tap water at pH 6.7, an increase in H_2O_2 concentration from 0.1 mM to 2 mM (a 20-fold increase) increased the degradation of the dye from 0.5 log to 2.75 log (a 5.5-fold increase) at an *IT* of 240 mJ/cm^2. Furthermore, for the same H_2O_2 concentration, the first order rate constant increased as the pH was lowered (Figure 6.3). The degradation was observed to be greatest at low pHs since the generation of radicals is higher at lower pHs. Finally, the rate at which the first order rate constant increased with decreasing pH also gradually increased as the H_2O_2 concentration increased. In the control experiment without UV light, no dye degradation was observed when it reacted with H_2O_2 at all pHs.

6.3. UV FLUENCE AND INACTIVATION MAPPING

Figure 6.4a consists of time-series images, spanning 0.12 sec, depicting the variation in spatial and temporal dose delivery (*IT*) and MS2 inactivation around the UV lamp constructed from a 'premixed' reactive tracer test. Note that these images were calibrated from Rh6G concentration plots using the linear relationship between Rh6G residual and *IT* as well as that between *IT* and MS2 inactivation (Figure 6.1). Therefore, the *IT* and MS2 inactivation contours appear the same, despite having different scales. The images

are presented as cumulative fluence (mJ/cm^2) or cumulative log MS2 inactivation (*i.e.*, -log of survival ratio) at each location, where red represents the highest values and blue the lowest. The flow in the reactor is from left to right, the lamp is represented as a black circle, and the reactor walls as black lines outlining the top and bottom of the images. The region upstream of the lamp should be ignored as it experiences a shadow effect due to the obstruction of laser light (coming from right to left) by the lamp.

The accumulated *IT* and the corresponding log inactivation contours show that the wake zone or the region immediately downstream of the lamp (approximately x = 5.25 cm) experienced the highest local fluence and inactivation, greater than 35 mJ/cm^2 and 1.65 log, respectively. This occurs due to the presence of the recirculation zone leading to a higher residence time, explained at great depth in Gandhi et al. (2011). Farther downstream, regions with a lower cumulative fluence of 25 – 40 mJ/cm^2 (1.2 – 1.9 log) were observed in the von Karman vortex shedding zone. This reduction in *IT* occurred due to mixing in the region downstream, leading to an average *IT* that is a combination of higher values in the wake region and lower values from the entrainment into the von Karman vortex (Wols et al., 2010b).

The occurrence of high residence time zone inevitably leads to zone with lower residence time or short-circuiting of flow. Combined with lower fluence rate and minimal transverse mixing downstream of the lamp, this leads to a short-circuiting zone with approximately 50% lower fluence as compared to the central region or the region downstream of the wake (Elyasi and Taghipour, 2010). Santoro et al. (2010) displayed an

enhanced degradation of target contaminant (TCEP) by more than 50% in the wake region compared to near the wall in a RANS based CFD simulation. In a region 1.5 cm wide along the reactor walls, the cumulative fluence was 15 – 20 mJ/cm^2 (0.7 – 0.94 log) and approximately 60% (in the wake) and 25% (at x = 12.75 cm) lower standard deviation existed near the wall as compared to the central region owing to the minimal transverse mixing (Figure 6.4b). As the distance downstream of the lamp increased, the variation in standard deviation across each vertical profile decreased. Greater mixing over shorter distances, such that these gradients are avoided, is desired as it leads to plug flow conditions and is typically achieved using modifications such as rings or baffles (Wols et al., 2010a; Blatchley et al., 1998; Janex et al., 1998).

The *IT* and log inactivation plots were highly transient, with von Karman streets alternating above (upper image in Figure 6.4a, rotating counter-clock wise) and below (bottom image in Figure 6.4a, rotating clock wise) the center of the lamp. The importance of an instantaneous versus time-averaged analysis is further depicted by computing the standard deviation in *IT* over 4.125 s (arbitrary time duration) at two vertical profiles downstream of the lamp (Figure 6.4b), thus measuring the temporal variation in *IT* across the reactor height. In the wake region profile (x = 5.25 cm), the highest standard deviation was observed at the top and bottom edges of the cylinder where *IT* changed significantly and frequently due to the occurrence of the cyclic flow into the region (Figure 6.4a). Furthermore, lower standard deviation was observed in the wake zone where the change in *IT* occurred less frequently due to greater mixing. At x = 12.75 cm, the effect of the cylinder on the flow was reduced and the variation in standard deviation over the region

downstream of the wake became more uniform. However, the overall standard deviation at each point increased slightly as compared to the wake region because limited mixing occurred over a region approximately 15 cm downstream of the lamp based on the non-reacted tracer standard deviation profile (data not shown). These drastic variations in *IT* over time were not captured in Figure 6.5, the time-averaged fluence delivery.

The wake formations downstream of a cylinder appear to strongly affect the fluence delivery in the reactor. In order to identify the relationship between hydrodynamics and fluence, proper orthogonal decomposition (POD) analysis was performed dominant characteristics amongst incoherent turbulent motions were isolated. Note that most POD analyses employ data from multi-point measurement techniques such as PIV, while they have recently been successfully applied to concentration data (Gnirss and Tropea, 2008; Hirota et al., 2008). Figure 6.6 shows the results of decomposition of instantaneous hydrodynamics (Figure 6.6a, constructed using data from Gandhi et al., 2011) and fluence (Figure 6.6b) based on tracer concentrations at different modes that represent spatially averaged structures arranged in descending order of energy contribution to the flow. The vortices in both decompositions, obtained from different experiments, appear similar in size, structure and location. In mode 1, the red contours represent the bulk flow of the tracer and the blue contours regions where no tracer was present; and vice versa in subsequent flow cycles. Mode 2 represents the von Karman vortex shedding and modes 3 and 4 capture the transport of the tracer by the vortices shed in the wake region, where the red and blue contours represent opposite direction of rotation. Minor discrepancies were observed such as the contour colors; however, these are artifacts of the images used

in the analysis. The overall structure of each mode is more important, which reveals the most dominant characteristics. Since the structures uncovered upon decomposition of instantaneous flow appear the same as the fluence, this suggests that fluence fluctuation is largely governed by unsteady hydrodynamics.

6.4. PATH SPECIFIC FLUENCE

Figure 6.7 presents the fluence (values on the left) and corresponding log MS2 inactivation (values on the right) for different injection points (center, 0.64, 1.27 and 2.54 cm above center, and wall) at three upstream distances determined from the 'path specific' experiments. The cumulative *IT* and log inactivation represent mixed-cup values, *i.e.*, the average values at the far downstream of the UV lamp. At the same upstream distance, microorganisms travelling at the center showed the highest *IT* and MS2 log inactivation when compared to the off-center injections. For example, as the injection location into the reactor increased from the center to 0.64, 1.27 and 2.54 cm above center at 2.5 cm upstream of the lamp center, significant drops, 35%, 70% and 87%, respectively, in *IT* relative to center injection were observed. This occurs as the majority of the microorganisms travel through the high UV intensity regions with a greater residence time, thus accumulating a higher fluence. Little or no fluence was accumulated when the tracer was introduced at the walls (depicted as red lines) due to greater velocities and lower fluence rate in this region.

Similar trends were observed at injection distances farther upstream; however, the reduction in *IT* at greater heights from the center became smaller as the upstream distance increased. For example, at 17.7 cm upstream, an *IT* reduction of 38% and 60% was experienced when dye was injected at 1.27 and 2.54 cm above center. Alternatively, when the upstream injection distance increased, higher *IT* and MS2 inactivation were observed for the same height injection. As the upstream distance increased, the rate of log inactivation increased by approximately 30% for 0.64 cm above center injection and 72% for 2.54 cm above center injection, while the increase was insignificant for the center injection. In addition, when dye was introduced at the wall at 32.4 cm upstream, fluence of approximately 2.3 mJ/cm^2 (data not shown) was observed. Collectively, the significance of vertical location for the point of entry becomes less as the upstream distance increases due to lateral mixing. In other words, by increasing the upstream distance of travel, the paths that led to short-circuiting in UV reactors are reduced. The vertical point of entry that leads to 50% reduction in accumulated *IT* compared to center injection would be 1 cm for 2.5 cm upstream injection and 1.9 cm for 17.7 cm upstream injection. These analyses suggest that a significant improvement in performance (for example, 0 to 2.3 mJ/cm^2 at the wall) for paths that diminish the performance of the reactor would be observed when the straight inlet channel length is increased (Gandhi et al., 2011). Consistently, in annular reactors, rearranging the inlet from perpendicular to parallel to the bulk flow (Sozzi and Taghipour, 2006; Moreira et al., 2007) and a longer straight pipe inlet placed perpendicular (Zhao et al., 2009) have been found to enhance reactor performance.

6.5. LAGRANGIAN ANALYSIS

Figure 6.8 illustrates selected particle trajectories for a center (Figure 6.8a) and 1.27 cm off-center and a wall injection (Figure 6.8b) over 1 sec, obtained from the Lagrangian-based analysis in Tecplot® and their corresponding MS2 inactivation calculated using the fitted inactivation equation (Figure 6.1). These trajectories not only represent paths that were unique but depict the range between which particles travel for each injection scenario. The model assumed a two-dimensional flow characterized by the instantaneous velocity field in which the particles were massless and traveled along with the fluid element. This assumption is fairly accurate due to the high *Re* (= 4900 based on sleeve diameter) in the reactor. Since the trajectory of each particle is dependent on the instantaneous vector field, forty one sets of temporal data were analyzed at each particle release point to achieve an accurate representation of all possible paths. Particle release scenarios from above (depicted by black lines) and below (depicted by white lines) the lamp were analyzed for the center and 1.27 cm off-center cases. For the center injection, the particles were released at the top and bottom of the lamp since the velocity vectors upstream of the lamp end in the stagnation zone depicted by the white dot in Figure 4a. However, the inactivation values reported reflect the path travelled along the centerline up to the stagnation point and then along the cylinder surface to the particle release position. The contours in the background represent the UV intensity field used in this study.

For center injection, the paths that traversed the wake received the greatest inactivation, 1.22 – 1.48 log, while paths not entrained received the lowest inactivation, 0.77 and 0.85 log. The particles released at the top traversed in various directions: two particles, (c) and (d), passed through the wake zone, entrained into a von Karman vortex at the bottom of the lamp and flowed horizontally while the other two paths remained outside of the wake, one entrained in a von Karman vortex at the top (path b) and the other experienced no entrainment and flowed horizontally downstream (path a). For the particles released at the bottom, one particle was entrained into the wake zone (path g) with a longer residence time, two particles entrained in a von Karman vortex (paths e and f) and the other particle travelled horizontally downstream (path h). An overall variation in inactivation of approximately 50%, *i.e.*, the mixed cup value downstream of the lamp, was observed in this injection scenario.

Particles released at 1.27 cm off-center travelled farther from the wake zone and thus received lower inactivation. Only one out of the eight paths traversed through the recirculation zone (path d), consequently receiving the highest inactivation, 0.67 log. For the particles released at the top, two particles, paths (b) and (c), was entrained in the von Karman vortex while one particle (path a) travelled horizontally, subsequently receiving the lower inactivation, 0.39 log. Similarly, two particles released from the bottom (paths e and f) were entrained in the von Karman vortex, while paths g and h travelled fairly horizontally through the reactor; path d received the lowest log inactivation (0.41 log). On average, a log inactivation reduction by approximately 50% was observed for all particle paths compared to the center injection. Finally, the particle that was released at

the wall received a mere 0.25 log inactivation, approximately five and two times lower than the center injection and 1.27 cm off-center dose, respectively.

Results presented in Figures 6.7 and 6.8 confirm that as the injection height increased away from the center, the inactivation decreased. In addition, the most critical paths are closest to the wall, where inactivation was reduced by a factor of five compared to the center injection. Additionally, this analysis complements the 'pre-mixed' test results, where the local cumulative *IT* along the walls was 50% less than the central region at x = 12.75 cm. The Lagrangian analysis showed that particles trapped in the wake region spent longer time in the reactor, thus accumulating a higher dose while particles travelling close to the walls received a significantly lower dose, hence concluding that these were the most critical paths (Chiu et al., 1999).

Figure 6.9 depicts the gradual change in instantaneous fluence and log inactivation as dye injected at the center (Figure 6.9a) and 2.54 cm off-center (Figure 6.9b) traversed through the lamp region, which complement the above-discussed Lagrangian analyses in that the images show the 'sum' of various paths that tracer takes at each injection. The center injection received approximately 11 mJ/cm^2 or 0.52 log over the entire section. As microbes traversed the reactor, they accumulated approximately 6 mJ/cm^2 fluence in the recirculation zone while about 3 mJ/cm^2 fluence in the von Karman vortex zone. However, the 2.54 cm off-center injection received approximately 3.5 mJ/cm^2 or 0.165 log, where majority of the *IT* was accumulated in the vicinity of the lamp. It is noted that inactivation predicted from the Lagrangian analysis was approximately two to five times

higher than that measured from the dye injection as the predictions represent inactivation along one particular path while the measurements depict averaged (mix-cup) inactivation for all paths travelled in each injection. In addition, differences can be attributed to the transverse diffusion of the dye, which was not accounted for in the Lagrangian analysis. This phenomenon leads to a non-linear absorption of UV light based on the level of spreading, thus reducing the actual fluence rate along the path travelled by majority of the dye. In order to account for this reduction, the UV intensity model assumed a UVT of 82% in the entire section.

6.6. CONCLUSION

This study demonstrates that the 3DLIF technique can be used to assess the process efficiency of UV reactors, optimize their performance and design new UV reactors. Valuable information regarding the temporal and spatial distribution of delivered UV fluence and microbial inactivation can be obtained, which are not possible with other experimental methods. For example, the results presented herein provide quantitative information on the effect of upstream hydrodynamics on the microbial inactivation and suggests the importance of upstream mixing. Yet, this study is considered as the first demonstration of this technique for visualization and quantification of fluence and inactivation in perpendicular-to-flow UV reactors and the first to establish a connection between fluence delivery and the unsteady turbulence. More research is needed to apply to various other reactor configurations and flow conditions, including larger reactors with circular cross section and multiple-lamp placements. No past studies have performed

quantitative comparison between CFD simulations, which have been widely used for UV reactor design and optimization, and such experimental data, which is the focus of current study.

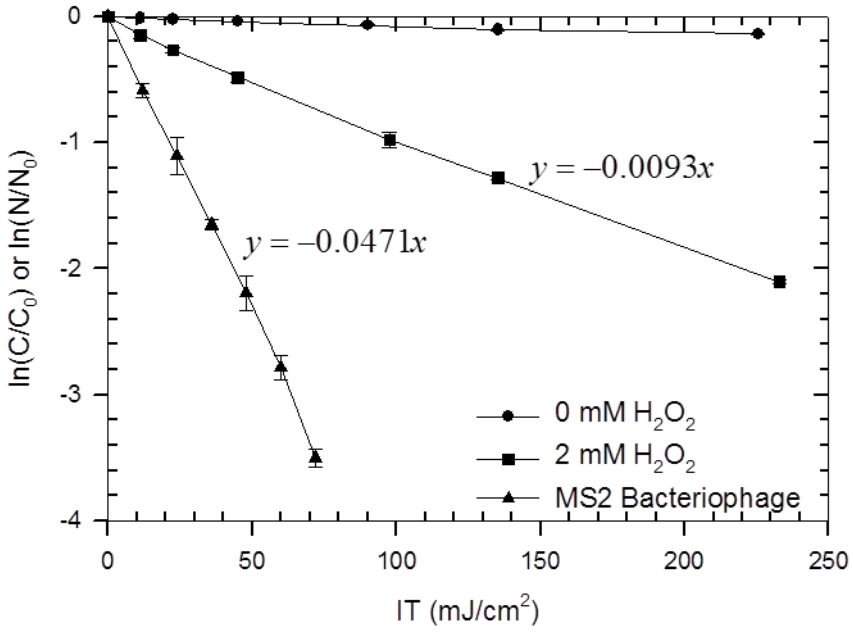

Figure 6.1: Rh6G dye degradation kinetics using 0 and 2 mM H_2O_2 and MS2 inactivation kinetics. Dye decay curve was used to convert dye degradation ($\ln(C/C_0)$ to *IT*, while the MS2 inactivation curve was used to convert *IT* to log inactivation ($\ln(N/N_0)$), according to the equations obtained from a linear curve fit through the origin.

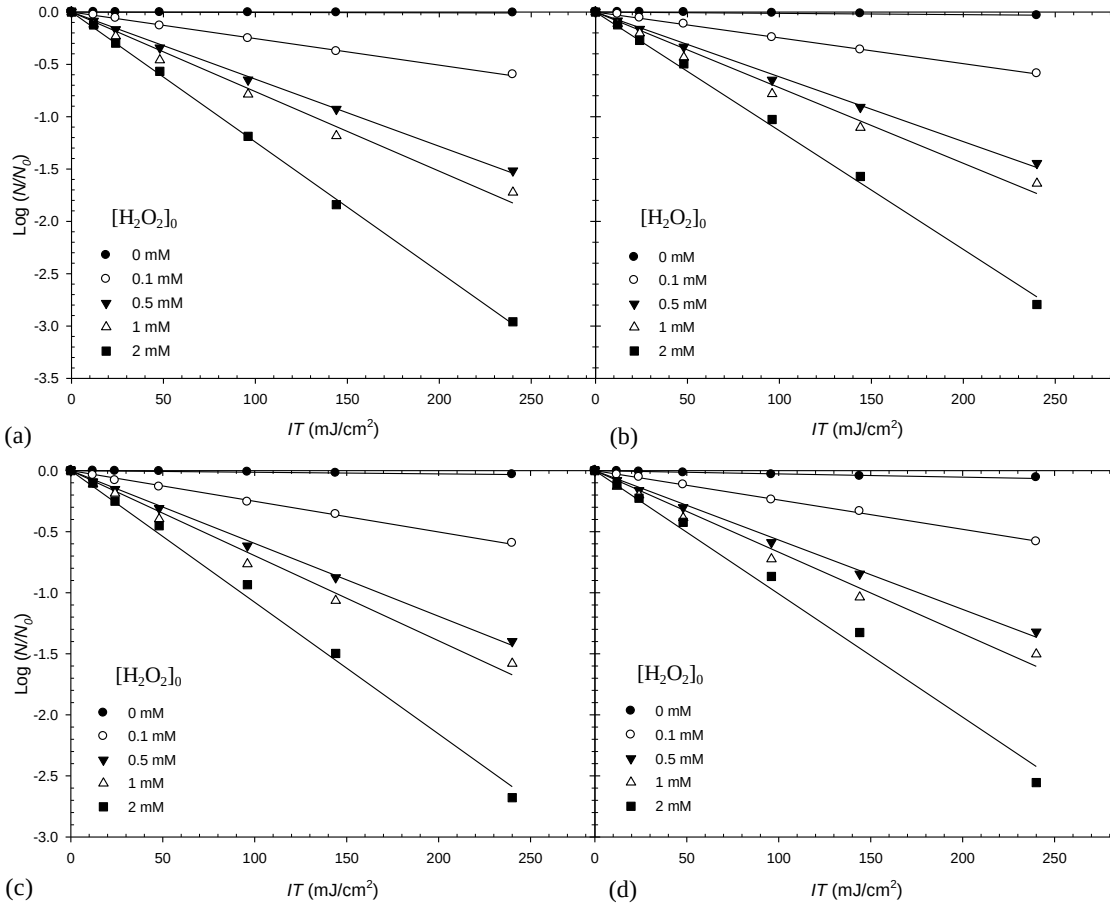

Figure 6.2: Degradation kinetics of Rhodamine 6G at various H_2O_2 concentrations (0, 0.1, 0.5, 1 and 2 mM) for different pHs: (a) pH 4.7, (b) 5.6, (c) 6.7 and (d) 7.8 (20°C).

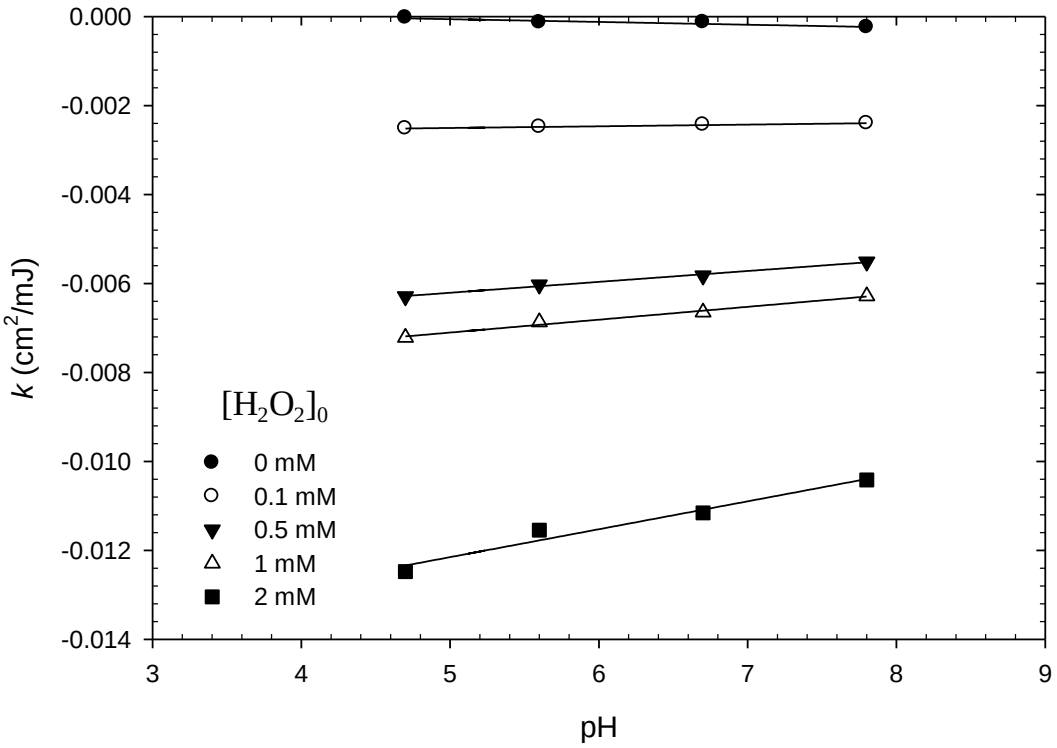

Figure 6.3: Rate constants plotted for different H_2O_2 concentrations (0, 0.1, 0.5, 1 and 2 mM) as a function of pH.

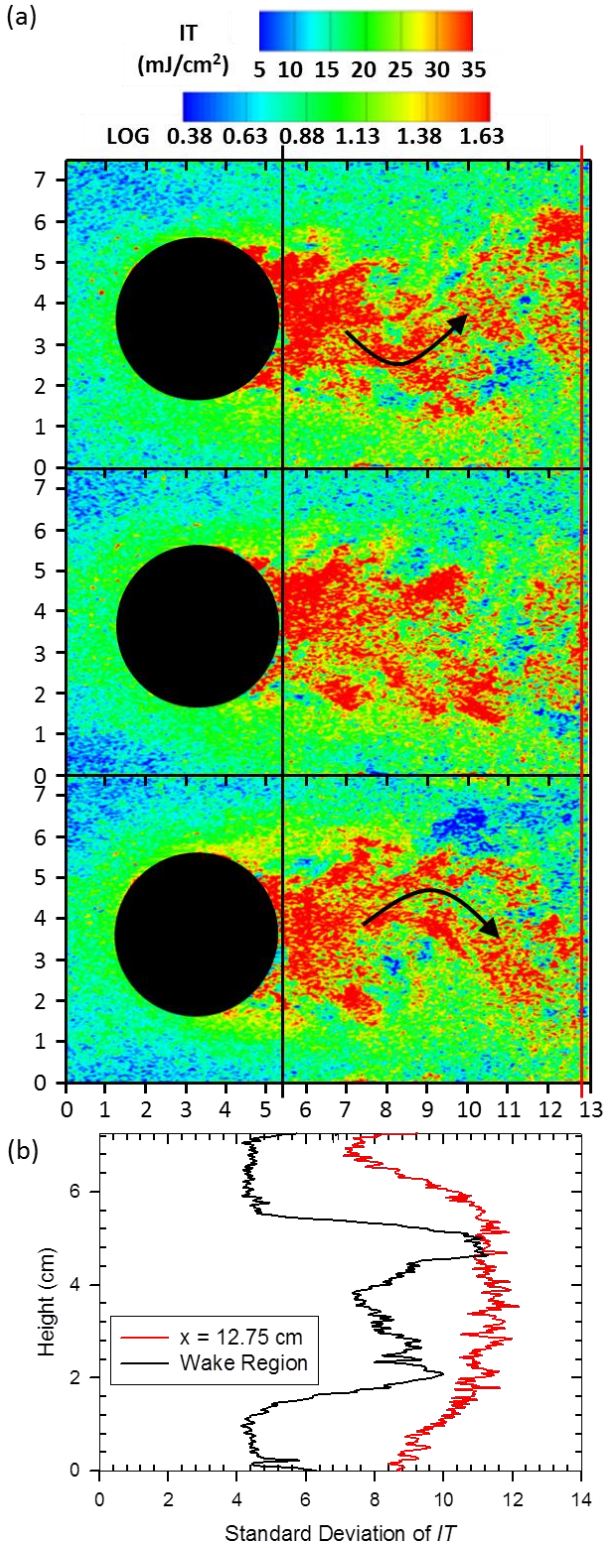

Figure 6.4: (a) 2D instantaneous and temporal variation (0.12 s) in fluence delivery (mJ/cm^2) and MS2 log inactivation around the lamp and (b) standard deviation in the *IT* along vertical profiles at the wake region (x = 5.25 cm) and x = 12.75 cm.

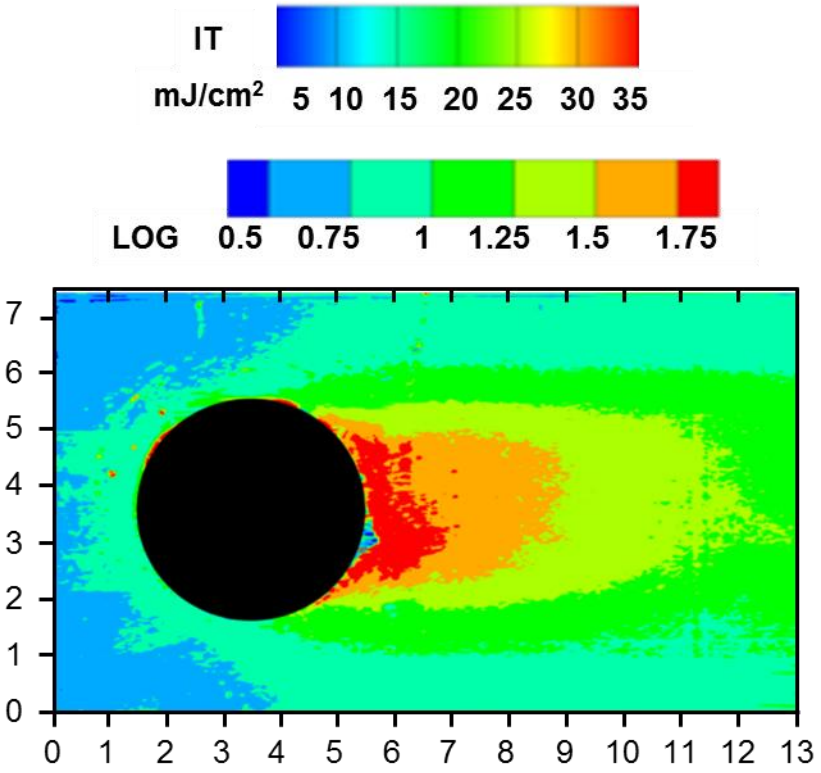

Figure 6.5: 2D time-averaged visualization of the spatial variation of fluence delivery (mJ/cm^2) and MS2 log inactivation around and downstream of the lamp.

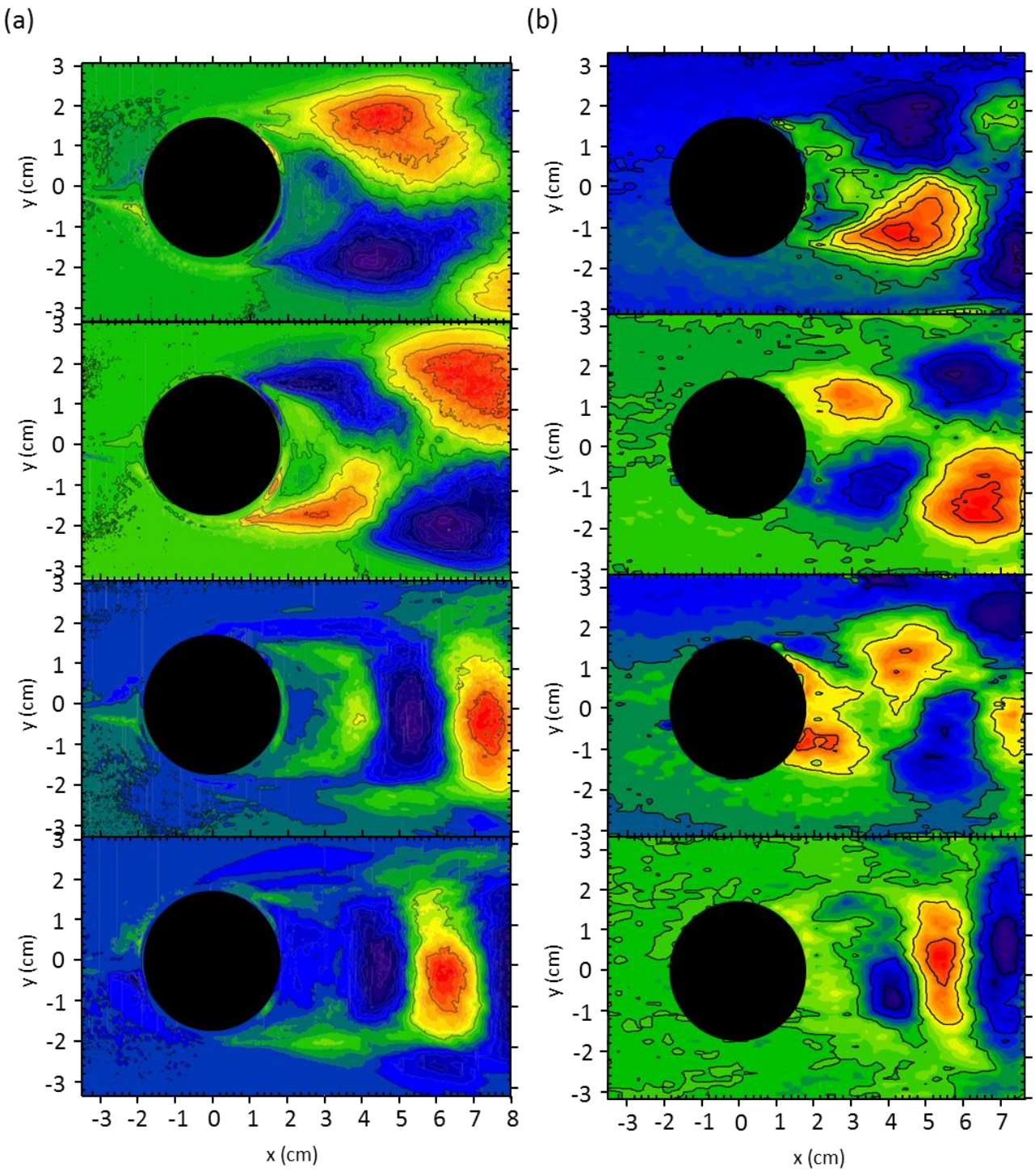

Figure 6.6: Modes 1 – 4 in the decomposition of instantaneous (a) conservative tracer concentration (obtained from Gandhi et al. (2011)) and (b) fluence delivery or MS2 log inactivation.

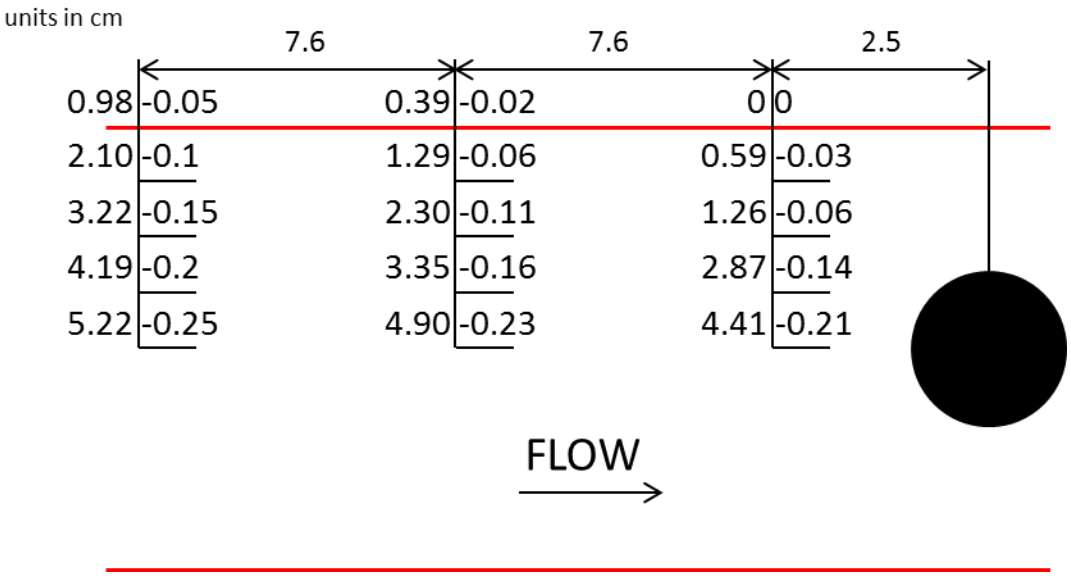

Figure 6.7: Path specific analysis of the fluence (mJ/cm^2, values on the left) and corresponding MS2 log inactivation (values on the right) for a center, 0.64, 1.27 and 2.54 cm above center and a wall injection based on various upstream distances as indicated. The direction of the flow is from the left to right and the red lines indicate the reactor walls.

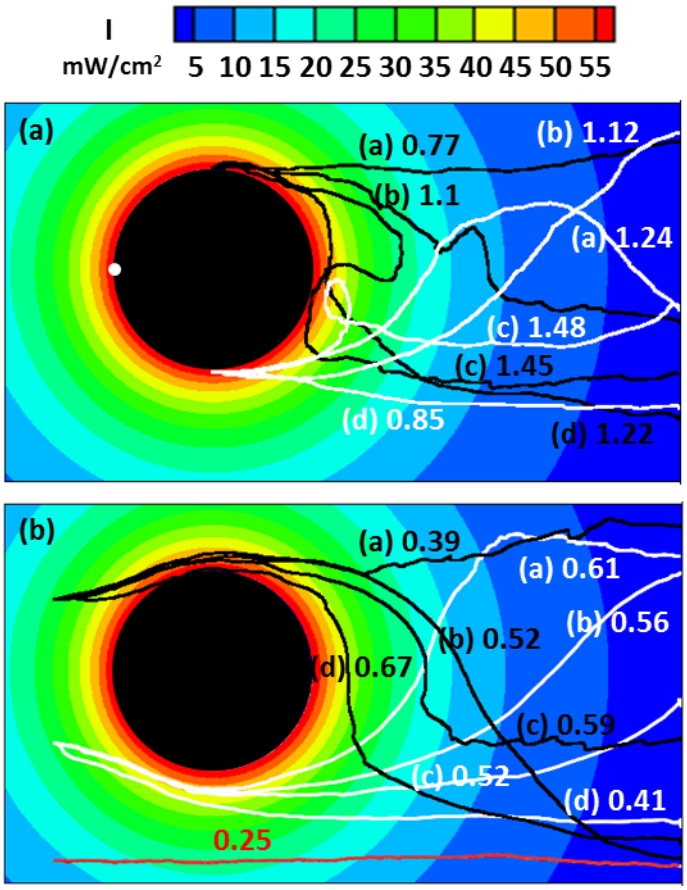

Figure 6.8: Temporal change in MS2 log inactivation for (a) center injection, (b) 1.27 cm above the cylinder and at the wall along with their respective log inactivation values based on a random walk analysis. Particles were released above and below the cylinder and paths that varied significantly from each other are shown. The particle paths were superimposed on the UV intensity field. The white dot in (a) represents the stagnation point.

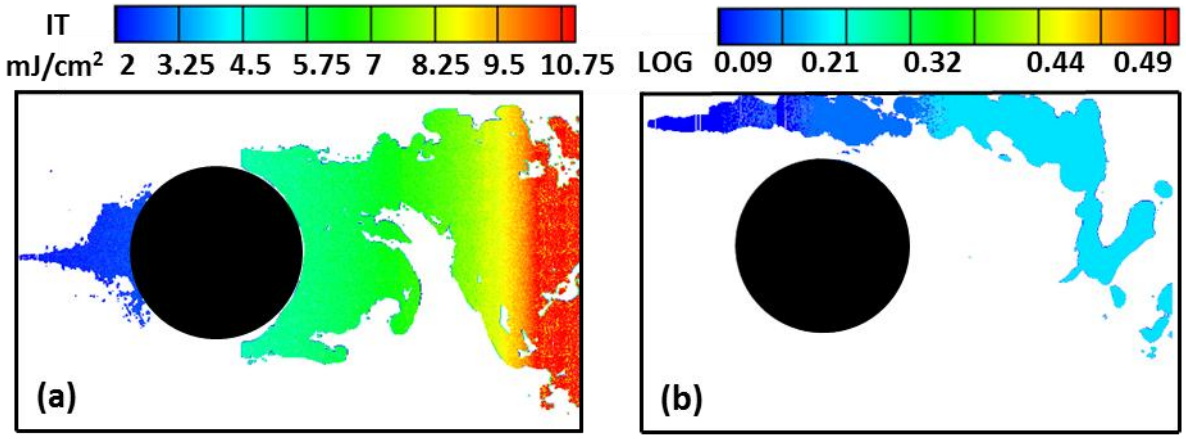

Figure 6.9: 2D visualization of instantaneous fluence (mJ/cm^2) and MS2 inactivation (log) for (a) center and (b) 2.54 cm off-center injection. Low values (less than 0.75 mJ/cm^2), depicted as white, were cutoff.

CHAPTER 7.

CONCLUSIONS

Inactivation by UV light is an effective treatment for microorganisms such as *Cryptosporidium parvum* (*C. parvum*) oocyst and *Giardia lamblia* cysts that have shown strong resistance to common water disinfectants such as free chlorine and monochloramine. In addition, little or no formation of disinfection by-products (DBPs) compared to chemical disinfection makes UV disinfection highly advantageous. However, a spatial and temporal assessment of the hydrodynamics, the UV dose delivered and the reactor performance has been severely limited for utilities practicing UV disinfection; the current validation technique, biodosimetry, treats the UV reactor as a "black-box" and hence does not account for the dependence of the dose delivery on the complex hydrodynamics and the spatial variation in UV intensity. Alternative methods such as fluorescent microspheres, a non-biological surrogate, and computational fluid dynamics have been developed; however, these methods have similar shortcomings.

Furthermore, lack of experimental studies on improving the knowledge of the steady or unsteady hydrodynamics and fluence delivery in a UV reactor with lamps placed perpendicular to flow warrant the need. Additionally, due to the complexity in the flow, brought about by vortex shedding downstream of a lamp, incorporating the time-averaged hydrodynamics vastly differs in predicting the hydrodynamics of the reactor compared to the instantaneous flow as observed in RANS vs LES-based CFD simulations. This vast difference in predicted flow directly affects the particle residence time and dose

distributions in the reactor. Thus, the need arises for a technique that can visualize and quantify the spatial and temporal hydrodynamics and fluence delivery in a UV reactor. This technique would not only aid in validation of simulation results but also in the design and optimization of UV reactors.

Three dimensional laser induced fluorescence (3DLIF) allows real time characterization of mixing conditions in a small-scale UV disinfection reactor by capturing fluorescence image emitted from a laser dye (i.e. Rhodamine 6G) using a high speed CCD camera. The 3DLIF system analyzed the hydrodynamics (Chapter 4) in a single lamp UV reactor placed perpendicular to flow by varying the height of injection from the lamp center. Mixing in each injection case was quantified using standard deviation and coefficient of variance (COV) at vertical profiles various distances away from the lamp center (Chapter 4). In addition, the importance of inlet and outlet structures to the hydrodynamics in the reactor was quantified (Chapter 4).

A tool, proper orthogonal decomposition (POD) that has been applied to a variety of flows, was introduced to UV reactors. It allows for the identification of coherent structures amongst highly turbulent flow; these structures occur most frequently in the flow. POD has been commonly applied to velocity vectors and vorticity contours. The application of POD to concentration data was compared with that of velocity vectors and vorticity contours in the flow around a cylinder in a confined space (Chapter 5) to validate its applicability to concentration data.

Finally, the 3DLIF system quantified the fluence (Chapter 6) in the single lamp UV reactor accounting for temporal and spatial variation of the local cumulative fluence. In addition, POD was applied to the fluence data and the structures were compared with those obtained from the hydrodynamics concentration based decomposition in Chapter 5. Lastly, a path specific analysis of the fluence as a function of the injection distance upstream of the lamp and vertically above the lamp was quantified (Chapter 6) and compared with a random walk model predicting the fluence along various paths.

The major contributions and conclusions of this research are:

1. 3DLIF technique was successfully applied for the first time to visualize and quantitatively analyze the flow characteristics and fluence delivery across a single UV lamp placed perpendicular to flow in a model reactor. This overcomes the limitation of past approaches where the reactor was considered a "blackbox". Table 7.1 shows the advantage and disadvantage of the LIF technique vs. existing validation techniques such as biodosimetry, fluorescence microspheres and CFD.
2. Conservative tracer tests were successfully conducted for the confined flow around UV lamps. It revealed unsteady turbulent flow characteristics such as the recirculation zone and the von Karman vortex street that are normally observed in flows around cylinders. The length of the recirculation zone and the Strouhal number were found to increase in the confined flow compared to an infinite medium.

Table 7.1: Pros and cons of the LIF method developed vs. other existing and alternative validation techniques

Method / Pros/Cons	Biodosimetry	Fluorescent Microspheres	Computational Fluid Dynamics	LIF (Current Method)
Determines Reduction Equivalent Dose (RED)	Yes	Yes	Yes	Yes
Determines Spatial Dose	No	No	Yes	Yes
Determines Temporal Dose	No	No	Possibly[1]	Yes
Accounts for microbes with different REDs	No	Yes	Yes	Yes
Requires further analysis post sample collection	Extensive	Extensive	No	Minimal
Real-time results	No, 24 - 48 hours	A few hours	A few hours to days[2]	Instantly
Experimental validation	Yes	Yes	No	Yes
Requires additional chemicals such as an oxidant	No	No	No	Yes
Requires additional models such as for light intensity	No	No	Yes	No

[1] Depends on the type of simulation used: the more commonly used model RANS does not provide temporal dose while the LES model accounts for the temporal component

[2] Once the model has been setup, the more commonly used model RANS takes only a few hours to complete while the LES model would take a few days to compute

3. Paths away from the center height, characterized by higher velocities and less influence of the cylinder, were also analyzed. The results demonstrated that a major difference in these pathways was the decreasing amount of dye entering the recirculation zone, which has a higher residence time, as the injection height increased. Paths greater than 1.9 cm above the lamp center can be considered as critical since majority of dye did not enter the higher residence time regions and hence need to be considered for when designing UV reactors.
4. Various reactor optimization techniques were introduced and quantified such as the length of the inlet configuration critical for the adequate mixing of water (or microorganism) before reaching the lamp. The results suggested that a longer approach length, greater than 30 cm, was beneficial to increase the probability of microbes entering the region around the lamp sleeve irrespective of their entrance height into the reactor. This is especially important when elbows exist in the pipe upstream of the UV reactor.
5. The length of the outlet i.e., distance from the last lamp array to the reactor exit, was examined as mixing at the outlet was determined to drastically vary over time with an increase in injection height. A well-mixed outlet, i.e., when the concentration profile across the reactor height is within 10% as in the center injection case, would be desirable to improve the accuracy of the biodosimetry results. A minimum of 7 pipe diameters (reactor dimensions) is needed downstream to collect well-mixed samples regardless of the height of sampling without the presence of a static mixer. This ensures uniform mixing spatially over the height of the reactor and temporally and thus sampling in biodosimetry can

occur at any vertical point in the reactor. These inlet and outlet analyses were the first of its kind and aid in the optimization of the reactor design.

6. The POD method was applied to spatial tracer concentration data for the flow around a confined cylinder for the first time to successfully visualize coherent structures. The benefits of a concentration based decomposition method are: 1. Tracer concentration data are relatively easier to obtain in various types of flows such as in field experiments or major water bodies, where obtaining velocity field information is rather difficult; 2. Since the dye tracer data is not interrogated over a window, unlike velocity fields, fine detail is retained, which was clearly observed in the difference between LIF and RRLIF decomposition; 3. Computational time is reduced as the raw images are directly used in the POD analysis and concentration data are one-dimensional and 4. Reduced noise levels are expected as absolute concentration values are used, when compared to vorticity, where using derivatives amplify the errors. In addition, these results are compared to their corresponding velocity-based, to validate the concentration decomposition method.
7. The velocity-based decomposition was found to be identical for images captured in 25 s and 5 s at 200 Hz in terms of the energy contained in each mode and in the position of each vortex in modes 1 and 2 even though the rotation of the vortices were shifted by half a cycle. The velocity decomposition results demonstrate that only modes 1 and 2 identify useful coherent structures for the recirculation zone and the von Karman vortex shedding.

8. For the LIF and RRLIF concentration decomposition, mode 1 represented the regions with the highest concentration fluctuations, i.e., where dye was not present; mode 2 represented the von Karman vortex shedding; modes 3 – 5 captured the shedding vortices downstream of the wake region and mode 6 indicated the wake shear layer around the cylinder. Even though similar coherent structures are captured by LIF and RRLIF based decomposition, the major difference between these decomposition methods is that RRLIF images are much smoother than the LIF images. While RRLIF can predict the large-scale features of the turbulence in the flow well, it omits smaller scale and thus overestimates the energy contained in the larger scales.
9. POD analysis of velocity fields and tracer concentration revealed similar coherent structures, the recirculation zone and von Karman vortices, thus validating the concentration decomposition method.
10. Premixed dye injection method visualized and quantified the spatial and temporal fluence distribution downstream of the UV lamp. This method indicated higher cumulative local fluence in the region downstream of the lamp while more than 50% lower local fluence in a section 1.5 cm wide along the reactor walls due to short-circuiting, lower fluence rates and minimal transverse mixing downstream of the lamp. Transverse mixing along the walls has to be induced to ensure proper mixing between the central and the wall regions even after the distance between the lamp and the wall is reduced to limit short-circuiting zones. This can be brought about by the placement of baffles along the walls to force the flow closer

to the lamps. Additionally, reducing the space between the walls and the UV lamps will help limit these zones at the expense of inefficiency in the lamp usage.

11. The temporal standard deviation profile at various vertical sections downstream of the reactor revealed the importance of instantaneous as opposed to time-averaged analysis. Thus, in CFD simulations, a large eddy simulation (LES) to determine the fluence distribution is required to provide accurate reactor performance. LES modeling requires high computing power, but with the development of technology, this method becomes more affordable in terms of cost and time.
12. The decomposition of local fluence delivery revealed similar structures to that of the hydrodynamics. The main phenomena affecting both equally are the recirculation and von Karman vortex shedding, thus suggesting a direct correlation between hydrodynamics and fluence delivery. The wake formations is shown to be a driving force in the effectiveness of the reactor to disinfect such that changing the *Re* based on the cylinder diameter could be important to optimizing the design of a system.
13. The path specific analyses and Lagrangian-based analysis quantified the effect of injection height and distance from the UV lamp and revealed a significant increase in dye degradation when the distance of injection upstream of the lamp was increased at all heights. Additionally, the high variation in fluence (~50%) amongst different paths in each injection height in the Lagrangian-based analysis further proves the importance of a temporal vs. time-averaged method i.e., mixed-cup results from the experimental path specific analyses.

CHAPTER 8.

FUTURE WORK

8.1 APPLICATION OF THE DEVELOPED TECHNIQUE TO LARGER UV REACTORS

The technique developed was only applied to a small-scale reactor consisting of a single lamp. However, the reactors used in water treatment plants are larger in scale consisting of many lamps placed in a staggered configuration. In addition to rectangular cross-section reactor, those with circular cross-sections are also in use as in many re-engineered water treatment facilities, a section of the pipe was removed and the UV reactor installed. The application of this technique to full-scale reactor like configuration would be helpful to visualize the hydrodynamics and fluence delivery and compare performance with rectangular cross-section reactors.

8.2 APPLICATION OF THE LIF SYSTEM TO OPTIMIZE UV REACTORS

The LIF system can be utilized to optimize the performance of UV reactors. Modifications to the existing reactor such as adding baffles at various positions to analyze its effect on the hydrodynamics and fluence delivery downstream of the lamp. However, the incorporation of baffles further impinges the flow, creating a zone of fast velocities. The placement of the baffle is important to avoid this zone of fast velocities to travel away from the lamp and the wake region. In multiple lamp reactors, the

hydrodynamics associated with various lamp spacing can be analyzed. Lamp spacing is important to avoid the short-circuiting paths from the first lamp to pass through the reactor without passing near a downstream UV lamp. Lastly, various inlet conditions and the effect of the changing inlet angles and the upstream distance from the first lamp can be analyzed in terms of mixing around the lamps and dose delivery downstream of the lamps.

8.3 NUMERICAL SIMULATIONS OF UV REACTORS USING LARGE-EDDY SIMULATION CFD MODEL

LES simulations resolve most of the turbulent eddies and thus the flow fields are predicted more precisely. With the availability of the upstream velocity profile measured using particle image velocimetry (PIV), the LES method can predict the hydrodynamics in a single lamp placed perpendicular-to-flow reactor as examined in the experiments. Coupling the intensity model described in Chapters 3 and 5 with the appropriate dye decay model, a reacted tracer concentration map can then be developed. Conversion of this dye decay map to fluence or microorganism inactivation can then be accomplished using the fitted equation in Chapter 5. Once this LES model is validated with experiments, the development of a complete model for validation of UV reactors would be accomplished. Furthermore, LES can then be used as the modeling technique to analyze flow in various configuration UV reactors and develop energy efficient designs that are not only sustainable but also cost effective.

APPENDIX A

ADDITIONAL INFORMATION FOR CONSERVATIVE TRACER TESTS

A1. Three-dimensional hydrodynamics

Figures A1 and A2 show the instantaneous normalized three dimensional flow of the dye for the 0.5 in. and 1 in. off-center injections, respectively. These images and animations indicated that lower and lower amounts of dye flowed through the recirculation region as the injection moved further away from the center. In the 1 in. off-center injection, most of the dye travelled in a streamline that passed above the lamp with no effect of the presence of the UV lamp.

A2. Coefficient of Variation

Figures A3 and A4 plot the COV as a function of distance from the wake region of the lamp (depicted as 0) to the outlet (depicted as 1) for the three injection heights for the 2D and 3D cases, respectively. The time-averaged COV at each location for each height of injection is plotted. Similar COV trends were observed in the time-averaged two-dimensional and three-dimensional flows. For each injection height, the overall COV decreased, hence uniformity in the flow increased, as the dye moved from the wake region towards the outlet. In addition, the overall COV increased with an increase in injection height, hence reduced mixing was observed. The range of COV values

increased, hence a greater variability in the flow was observed, supporting previous observations. The analysis of the COV on each two dimensional plane perpendicular to flow in the three dimensional case resulted in qualitative comparison of dispersion in that plane for each injection case. A higher COV value meant low dispersion of the dye, which was expected in the regions immediately downstream of the UV lamp. Higher dispersion of the dye was expected in regions further downstream and as such a COV lower than the wake region was observed in these regions. Finally, it was observed that spreading of the dye decreased as the height of dye injection increased.

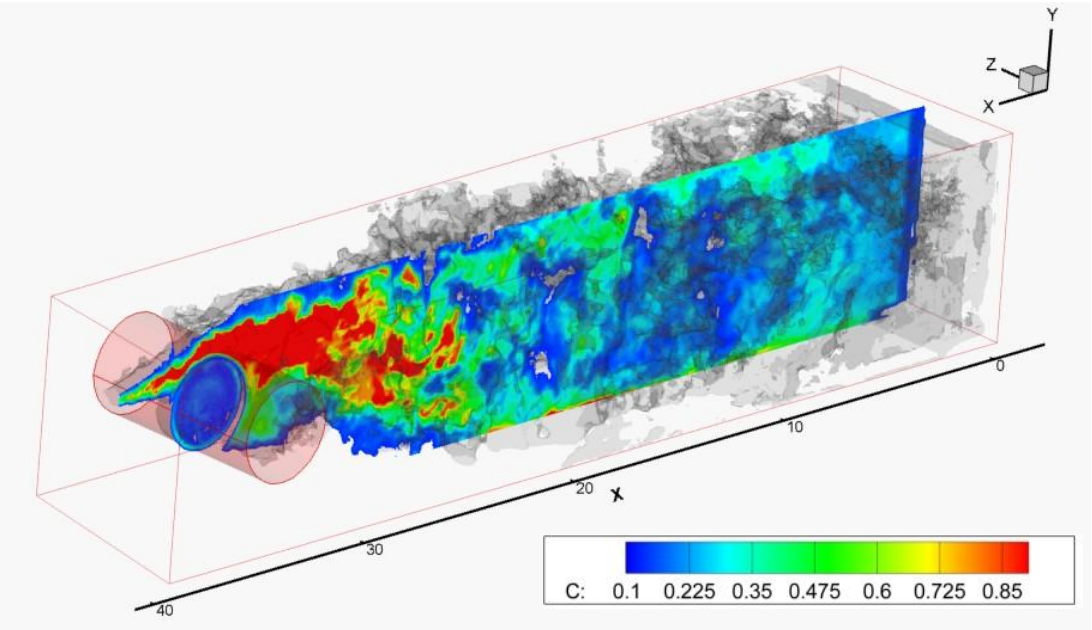

Figure A1: Normalized three-dimensional tracer flow for a 0.5 in. off-center injection shown on the center plane along with a gray iso-concentration surface.

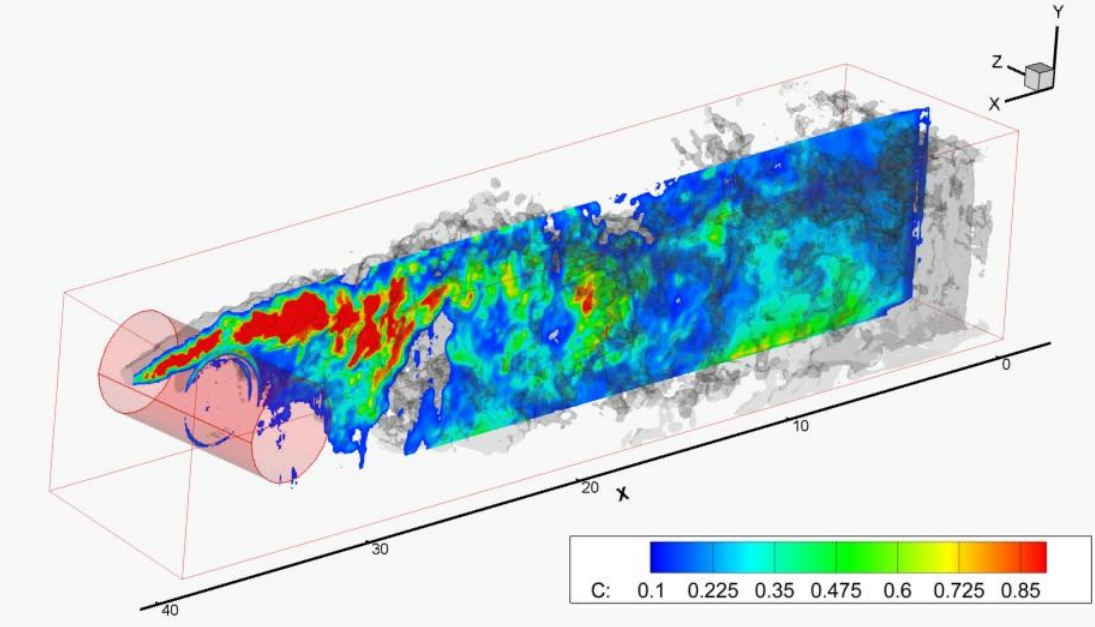

Figure A2: Normalized three-dimensional tracer flow for a 1 in. off-center injection shown on the center plane along with a gray iso-concentration surface.

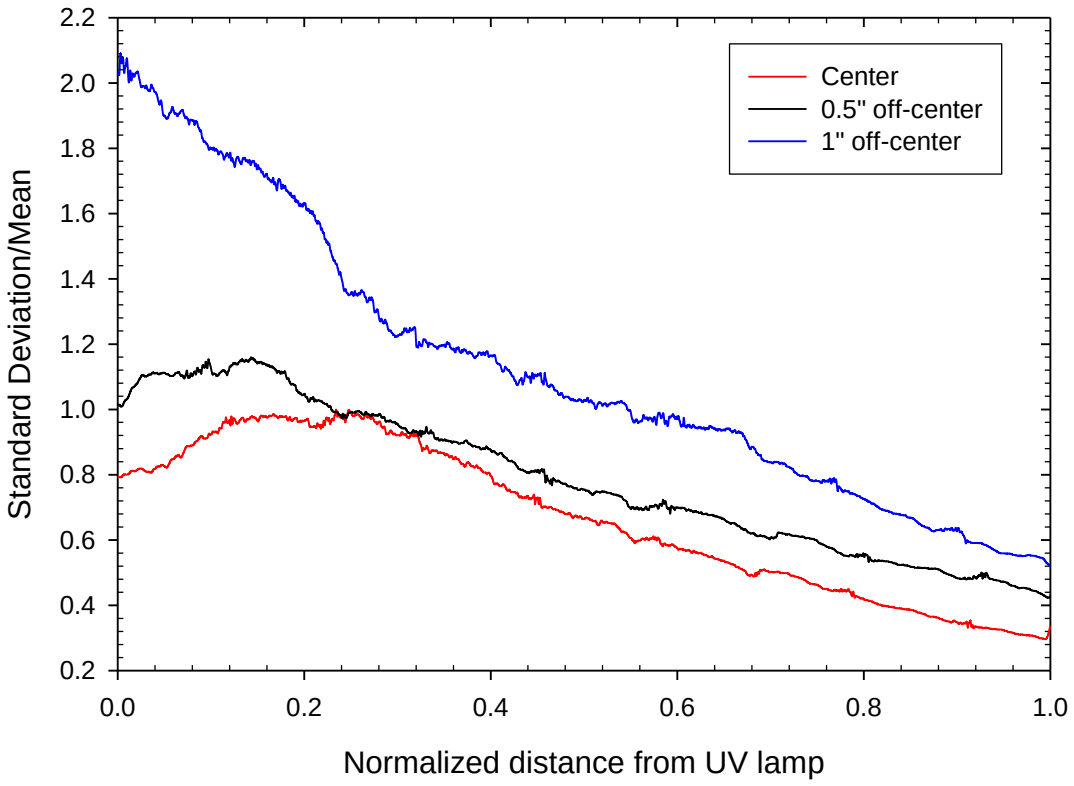

Figure A3: Time-averaged COV from the wake region (depicted at 0) to the outlet (depicted at 1) for zones perpendicular to flow in a two-dimensional flow for center (red), 0.5 in. off-center (black) and 1 in. off-center (blue) injections.

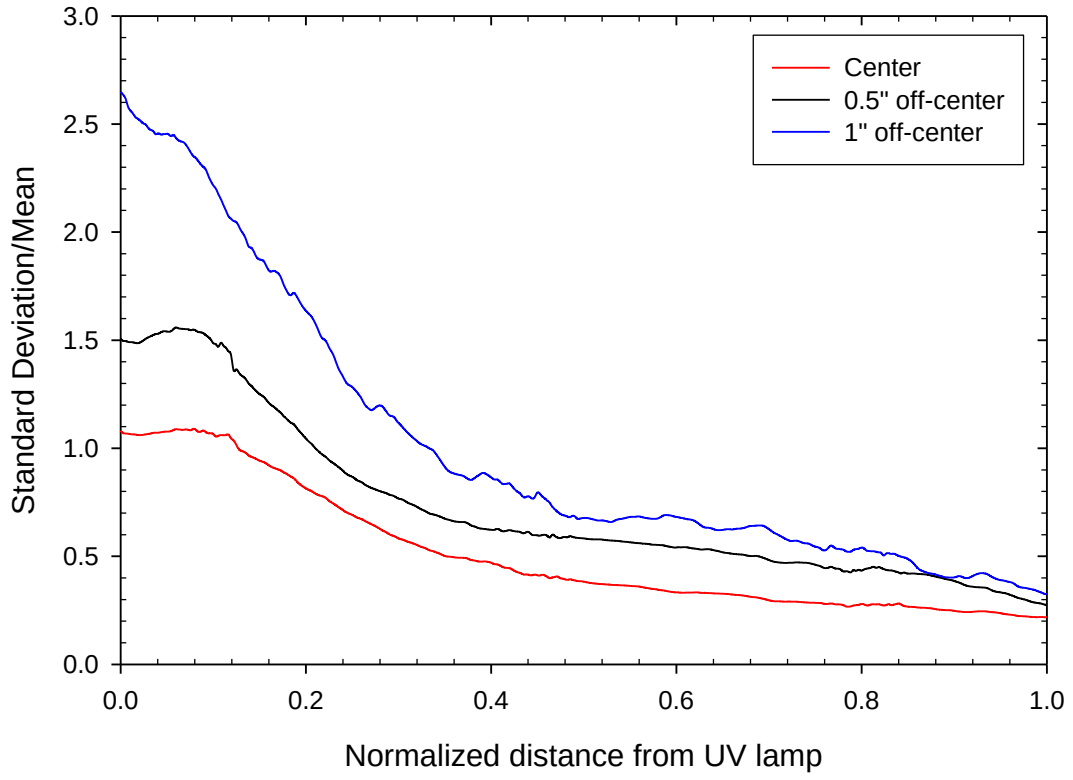

Figure A4: Time-averaged COV from the wake region (depicted at 0) to the outlet (depicted at 1) for planes perpendicular to flow in a three-dimensional flow for center (red), 0.5 in. off-center (black) and 1 in. off-center (blue) injections.

APPENDIX B

MATLAB™ CODE FOR PROPER ORTHOGONAL DECOMPOSITION OF REACTIVE TRACER TESTS*

---

*Code was developed with guidance from Duncan B. Bryant, Ph.D.

The same code can be adapted for the POD of concentration images by changing the following variables:

nx, ny, folder containing the images, numofimages and equation of the circle.

```
%%%%%%%%%%%%%%%%%%% Proper Orthogonal Decomposition %%%%%%%%%%%%%%%%%%%%
nx=500; % x direction pixels
ny=233; % y direction pixels
matlabpool open 4 % uses four processors to speed up calculation
cd ('E:\UV-LIF\UV RTT\Option 1\IT') % Folder containing images

%%%%%%%%%% Set Num of Images
numofimages = 826;
L=zeros(ny*nx,numofimages);% Preallocate Matrix Size

%%%%%%%%%% Create Matrix of Data

for i=1:numofimages
    k=i+172;
    clear header data Lif2
    [header,data]=hdrload(strcat(num2str(k),'.dat'));
    [Lif2,xi,yi,dy,dx,gridA]=dataextractandcomposC(data,nx,ny);
    for m=1:1:ny
        for j=1:1:nx
            if (m-114)^2+(j-296)^2 > 62^2 % Equation of circle with
center coordinates(296,114) and radius (62)
            else
                Lif2(m,j)=0;
            end
        end
    end

    L(1:nx*ny,i) = reshape(Lif2',nx*ny,1);
end
clear Lif2 header data xi yi dy dx gridA

%%%%%%%%%% Subtract Average and Build Covariance Matrix

Psi=mean(L')';
for i=1:numofimages
    L(:,i)=L(:,i)-Psi; % Subtract mean from each image
```

```
end;
save('mean.txt','Psi','-ascii');
CL=L'*L;

%%%%%%%%%% Calculate and Sort Eigenvalues and Eigenvectors

DL=eig(CL);
[VL,Q]=eig(CL);
clear CL
[DL,bL]=sort(DL,'descend');
for j=1:numofimages
    VL2(:,j)=VL(:,bL(j));
end
VL=VL2; clear VL2

%%%%%%%%%% Compute PHI and Normalize

PHIL=L*VL;
for i=1:numofimages
    PHIL(:,i)=PHIL(:,i)/norm(PHIL(:,i),2);
end
DL=DL/(numofimages-1);
save('modeEIGnosub.txt','DL','-ascii')
save('modePHILnosub.txt','PHIL','-ascii')

%%%%%%%%%% ENERGY FOR POD IN EACH MODE

tenergyL=sum(DL,1);
energyL = 0;
sumenL=zeros(length(DL),1);
nbasisL = 0;
i=1;
while (((energyL/tenergyL)*100) < 95)
    energyL = energyL+ DL(i);
    i=i+1;
end
for j=1:length(DL)
    sumenL(j)=sum(DL(1:j));
end
sumenL=(sumenL./tenergyL)*100;
nbasisL=i;

%%%%%%%%%% Modes 1-10

count = 1;

for j = 1:ny
    r = j-1;
    for i = 1:nx
        s = i - 1;
        b(count,1) = s*(-0.00024);
        b(count,2) = r*(0.00024);
        count = count + 1;
    end
end
```

```
mode1=zeros(nx*ny,4);
mode1(:,1:2)=data(:,1:2);
mode1(:,4)=PHIL(:,1);
file='mode1.dat';
fid=fopen(file,'wt');
fprintf(fid, '%s\n %d\n', 'VARIABLES = "X" "Y" "Z" "C", Zone I=500
J=233 K=1 ZONETYPE=ORDERED DATAPACKING=POINT'); % CHANGE
fclose(fid);
dlmwrite(file, mode1, '-append', 'newline','pc','delimiter','\t');

mode2=zeros(nx*ny,4);
mode2(:,1:2)=b;
mode2(:,4)=PHIL(:,2);
file='mode2.dat';
fid=fopen(file,'wt');
fprintf(fid, '%s\n %d\n', 'VARIABLES = "X" "Y" "Z" "C", Zone I=500
J=233 K=1 ZONETYPE=ORDERED DATAPACKING=POINT'); % CHANGE
fclose(fid);
dlmwrite(file, mode2, '-append', 'newline','pc','delimiter','\t');

mode3=zeros(nx*ny,4);
mode3(:,1:2)=b;
mode3(:,4)=PHIL(:,3);
file='mode3.dat';
fid=fopen(file,'wt');
fprintf(fid, '%s\n %d\n', 'VARIABLES = "X" "Y" "Z" "C", Zone I=500
J=233 K=1 ZONETYPE=ORDERED DATAPACKING=POINT'); % CHANGE
fclose(fid);
dlmwrite(file, mode3, '-append', 'newline','pc','delimiter','\t');

mode4=zeros(nx*ny,4);
mode4(:,1:2)=b;
mode4(:,4)=PHIL(:,4);
file='mode4.dat';
fid=fopen(file,'wt');
fprintf(fid, '%s\n %d\n', 'VARIABLES = "X" "Y" "Z" "C", Zone I=500
J=233 K=1 ZONETYPE=ORDERED DATAPACKING=POINT'); % CHANGE
fclose(fid);
dlmwrite(file, mode4, '-append', 'newline','pc','delimiter','\t');

mode5=zeros(nx*ny,4);
mode5(:,1:2)=b;
mode5(:,4)=PHIL(:,5);
file='mode5.dat';
fid=fopen(file,'wt');
fprintf(fid, '%s\n %d\n', 'VARIABLES = "X" "Y" "Z" "C", Zone I=500
J=233 K=1 ZONETYPE=ORDERED DATAPACKING=POINT'); % CHANGE
fclose(fid);
dlmwrite(file, mode5, '-append', 'newline','pc','delimiter','\t');

mode6=zeros(nx*ny,4);
mode6(:,1:2)=b;
mode6(:,4)=PHIL(:,6);
file='mode6.dat';
fid=fopen(file,'wt');
```

```
fprintf(fid, '%s\n %d\n', 'VARIABLES = "X" "Y" "Z" "C", Zone I=500
J=233 K=1 ZONETYPE=ORDERED DATAPACKING=POINT'); % CHANGE
fclose(fid);
dlmwrite(file, mode6, '-append', 'newline','pc','delimiter','\t');

mode7=zeros(nx*ny,4);
mode7(:,1:2)=b;
mode7(:,4)=PHIL(:,7);
file='mode7.dat';
fid=fopen(file,'wt');
fprintf(fid, '%s\n %d\n', 'VARIABLES = "X" "Y" "Z" "C", Zone I=500
J=233 K=1 ZONETYPE=ORDERED DATAPACKING=POINT'); % CHANGE
fclose(fid);
dlmwrite(file, mode7, '-append', 'newline','pc','delimiter','\t');

mode8=zeros(nx*ny,4);
mode8(:,1:2)=b;
mode8(:,4)=PHIL(:,8);
file='mode8.dat';
fid=fopen(file,'wt');
fprintf(fid, '%s\n %d\n', 'VARIABLES = "X" "Y" "Z" "C", Zone I=500
J=233 K=1 ZONETYPE=ORDERED DATAPACKING=POINT'); % CHANGE
fclose(fid);
dlmwrite(file, mode8, '-append', 'newline','pc','delimiter','\t');

mode9=zeros(nx*ny,4);
mode9(:,1:2)=b;
mode9(:,4)=PHIL(:,9);
file='mode9.dat';
fid=fopen(file,'wt');
fprintf(fid, '%s\n %d\n', 'VARIABLES = "X" "Y" "Z" "C", Zone I=500
J=233 K=1 ZONETYPE=ORDERED DATAPACKING=POINT'); % CHANGE
fclose(fid);
dlmwrite(file, mode9, '-append', 'newline','pc','delimiter','\t');

mode10=zeros(nx*ny,4);
mode10(:,1:2)=b;
mode10(:,4)=PHIL(:,10);
file='mode10.dat';
fid=fopen(file,'wt');
fprintf(fid, '%s\n %d\n', 'VARIABLES = "X" "Y" "Z" "C", Zone I=500
J=233 K=1 ZONETYPE=ORDERED DATAPACKING=POINT'); % CHANGE
fclose(fid);
dlmwrite(file, mode10, '-append', 'newline','pc','delimiter','\t');
```

Function **dataextractandcomposC** used in the above code:

```
function [ci,xi,yi,dy,dx,gridA]=dataextractandcomposC(data,nx,ny)
%Build Velocity and Axis from Davis Velocity Txt file
dx=abs((data(2,1)-data(1,1))/1000); % grid size [m]
dy=abs((data(nx+1,2)-data(1,2))/1000); % grid size [m]
gridA=dx*dy; %Real area of 1 grid [m^2]

ui=zeros(ny,nx);
```

```
vi=zeros(ny,nx);
k=0;
for i=ny:-1:1
    for j=1:nx
        k=k+1;
        ci(i,j)=data(k,4);
        xi(i,j)=data(k,1);
        yi(i,j)=data(k,2);
    end
end
```

Function **hdrload** used in the above code:

```
function [header, data] = hdrload(file)

% HDRLOAD Load data from an ASCII file containing a text header.
%     [header, data] = HDRLOAD('filename.ext') reads a data file
%     called 'filename.ext', which contains a text header.  There
%     is no default extension; any extensions must be explicitly
%     supplied.
%
%     The first output, HEADER, is the header information,
%     returned as a text array.
%     The second output, DATA, is the data matrix.  This data
%     matrix has the same dimensions as the data in the file, one
%     row per line of ASCII data in the file.  If the data is not
%     regularly spaced (i.e., each line of ASCII data does not
%     contain the same number of points), the data is returned as
%     a column vector.
%
%     Limitations:  No line of the text header can begin with
%     a number.  Only one header and data set will be read,
%     and the header must come before the data.
%
%     See also LOAD, SAVE, SPCONVERT, FSCANF, FPRINTF, STR2MAT.
%     See also the IOFUN directory.

% check number and type of arguments
if nargin < 1
  error('Function requires one input argument');
elseif ~isstr(file)
  error('Input must be a string representing a filename');
end

% Open the file.  If this returns a -1, we did not open the file
% successfully.
fid = fopen(file);
if fid==-1
  error('File not found or permission denied');
  end

% Initialize loop variables
% We store the number of lines in the header, and the maximum
% length of any one line in the header.  These are used later
% in assigning the 'header' output variable.
```

```
no_lines = 0;
max_line = 0;

% We also store the number of columns in the data we read.  This
% way we can compute the size of the output based on the number
% of columns and the total number of data points.
ncols = 0;

% Finally, we initialize the data to [].
data = [];

% Start processing.
line = fgetl(fid);
if ~isstr(line)
  disp('Warning: file contains no header and no data')
  end;
[data, ncols, errmsg, nxtindex] = sscanf(line, '%f');

% One slight problem, pointed out by Peter vanderWal: If the
% first character of the line is 'e', then this will scan as
% 0.00e+00. We can trap this case specifically by using the
% 'next index' output: in the case of a stripped 'e' the next
% index is one, indicating zero characters read.  See the help
% entry for 'sscanf' for more information on this output
% parameter. We loop through the file one line at a time until
% we find some data.  After that point we stop checking for
% header information. This part of the program takes most of the
% processing time, because fgetl is relatively slow (compared to
% fscanf, which we will use later).
while isempty(data)|(nxtindex==1)
  no_lines = no_lines+1;
  max_line = max([max_line, length(line)]);
  % Create unique variable to hold this line of text information.
  % Store the last-read line in this variable.
  eval(['line', num2str(no_lines), '=line;']);
  line = fgetl(fid);
  if ~isstr(line)
    disp('Warning: file contains no data')
    break
    end;
  [data, ncols, errmsg, nxtindex] = sscanf(line, '%f');
  end % while

% Now that we have read in the first line of data, we can skip
% the processing that stores header information, and just read
% in the rest of the data.
data = [data; fscanf(fid, '%f')];
fclose(fid);

% Create header output from line information. The number of lines
% and the maximum line length are stored explicitly, and each
% line is stored in a unique variable using the 'eval' statement
% within the loop. Note that, if we knew a priori that the
% headers were 10 lines or less, we could use the STR2MAT
% function and save some work. First, initialize the header to an
% array of spaces.
```

```
header = setstr(' '*ones(no_lines, max_line));
for i = 1:no_lines
  varname = ['line' num2str(i)];
  % Note that we only assign this line variable to a subset of
  % this row of the header array.  We thus ensure that the matrix
  % sizes in the assignment are equal.
  eval(['header(i, 1:length(' varname ')) = ' varname ';']);
  end

% Resize output data, based on the number of columns (as returned
% from the sscanf of the first line of data) and the total number
% of data elements. Since the data was read in row-wise, and
% MATLAB stores data in columnwise format, we have to reverse the
% size arguments and then transpose the data.  If we read in
% irregularly spaced data, then the division we are about to do
% will not work. Therefore, we will trap the error with an EVAL
% call; if the reshape fails, we will just return the data as is.
eval('data = reshape(data, ncols, length(data)/ncols)'';', '');

% And we're done!
```

APPENDIX C

MATLAB™ CODE TO CALCULATE THE DYE DEGRADATION, *IT* AND LOG INACTIVATION FOR REACTIVE TRACER TESTS

```
% UV RTT
clear all
cd('G:\Data\UV RTT\Water\ASCII Files')
[h,a]=hdrload(strcat('1.dat'));
d(:,1:3)=a(:,1:3);

clear a

for k = 1:826
    i = k - 1;
    j = i + 173;
    cd('G:\Data\UV RTT\Rxn\Calibrated\Smooth')
    file = strcat(num2str(j),'.','dat');
    [h,a]  =  hdrload(strcat(num2str(j),'.','dat'));  % Loads  the  file
with reacted dye

    cd('G:\Data\UV RTT\Water\Calibrated\Calibrated\Smooth')
    [h,b]  =  hdrload(strcat(num2str(i),'.','dat'));  % Loads  the  file
with no reaction

    c   =   real(log(((a(:,4))./b(:,4)))/-0.0093);   %   Converts   dye
degradation to IT

    c(find(c<0))=NaN; % Values below 0 are modified using an average of
the neighboring values
    y = inpaint_nans(c,5);
    c = y;

    c(find(c>100))=NaN;  % Values  above  100  (very  high)  are  modified
using an average of the neighboring values
    y = inpaint_nans(c,5);
    d = a;

    cd('G:\Data\UV RTT\IT') % Save the new variable

    fid=fopen(file,'wt');
    fprintf(fid, '%s\n %d\n', 'Zone I=500 J=233 K=1 f=point');
    fclose(fid);

    d(:,4) = y;
%     d(:,4)=y;
    dlmwrite(file, d, '-append', 'newline','pc','delimiter','\t');

end
```

```
% Convert IT to log inactivation of microbes

   for k = 1:826
        i = k - 1;
        cd('G:\Data\UV RTT\IT')
        file = strcat(num2str(i),'.','dat');
        [h,a] = hdrload(strcat(num2str(i),'.','dat'));

        b(:,4)=a(:,4).*-0.0471;  % Convert IT to log inactivation of
microbes

        cd('G:\Data\UV RTT\Inactivation') % Save the new variable

        fid=fopen(file,'wt');
        fprintf(fid, '%s\n %d\n', 'Zone I=500 J=233 K=1 f=point');
        fclose(fid);
        dlmwrite(file, b, '-append', 'newline','pc','delimiter','\t');

     end
```

APPENDIX D

MATLAB™ CODE TO COMBINE THE STREAMLINE PATH OBTAINED FROM TECPLOT ® WITH UV INTENSITY ALONG THE PATH TO CALCULATE THE ACCUMULATED *IT*

```
%% Combining streamlines and IT

% Load intensity profile
cd('E:\UV-LIF\Random Walk\UV Intensity')
[hdr,int] = hdrload('Intensity Profile-fine rect.dat');

cd('E:\UV-LIF\Random Walk\Velocity Files')
file = load('File numbers.txt');

% Use delta t (used 0.0005 in tecplot to calculate the particle track)
to calculate IT
deltat = 0.0005;

% Load particle path
cd('E:\UV-LIF\Random Walk\Velocity Files\201-400\Center circle')
[hdr,path] = hdrload('partpath.dat');

% Create new variable that stores all the intensity values along with
% particle path information
path_int = zeros(length(path),6);
path_int(:,1:4) = path;

uv_int = zeros(length(path),1);
index = zeros(length(path),1);

% Search for position in IT profile

 for i=1:length(path)

% Search for nearest x position first
     rx = (int(:,1) - path(i,1)); % rx is the difference in the x
     coordinate
     mx = (min(rx(find(rx >= 0)))); % mx is the minimum difference
     nx = find(rx==mx); % nx is the index with minimum values
     diff_x(i) = mx; % array with all the differences

% Search for the nearest y position in the nearest x position indexes
(nx) found above

     ry = (int(nx,2) - path(i,2)); % ry is the difference in the y
coordinate at ind1 index
```

```
     my = (min(ry(find(ry >= 0))));
     ny = (find(ry==my)); % final index closest to ith particle path
point
     index(i)=ny; % array with the closest indices

% Stores intensity values along with particle path information
     uv_int(i,1) = int(ny,4);
 end

path_int(:,5) = uv_int;
path_int(:,6) = path_int(:,5) * deltat;

s=cumsum(path_int);
```

REFERENCES

Abbaszadegan, M., Hasan, M.N., Gerba, C.P., Roessler, P.F., Wilson, B.R., Kuennen, R. and Van Dellen, E., 1997. "The disinfection efficacy of a point-of-use water treatment system against bacterial, viral and protozoan waterborne pathogens." *Water Research* 31(3), 574-582.

Alpert, S.M., Knappe, D.R.U. and Ducoste, J.J., 2010. "Modeling the UV/hydrogen peroxide advanced oxidation process using computational fluid dynamics." *Water Research* 44(6), 1797-1808.

Bakewell, H.P. and Lumley, J.L., 1967. "Viscous sublayer and adjacent wall region in turbulent pipe flow." *Physics of Fluids* 10(9P1), 1880-1886.

Ball, K.S., Sirovich, L. and Keefe, L.R., 1991. "Dynamic eigenfunction decomposition of turbulent channel flow." *International Journal for Numerical Methods in Fluids* 12(6), 585-604.

Batch, L.E., Schulz, C.R. and Linden, K.G., 2004. "Evaluting water qualify effects on UV disinfection of MS2 coliphage." *Journal American Water Works Association* 96(7), 75-87.

Baxendale, J.H. and Wilson, J.A., 1957. "The photolysis of hydrogen peroxide at high light intensities." *Transactions of the Faraday Society* 53(3), 344-356.

Berger, E. and Wille, R., 1972. "Periodic flow phenomena." *Annual Review of Fluid Mechanics* 4, 313-340.

Berkooz, G., Holmes, P. and Lumley, J.L., 1993. "The proper orthogonal decomposition in the analysis of turbulent flows." *Annual Review of Fluid Mechanics* 25, 539-575.

Bernero, S. and Fiedler, H.E., 2000. "Application of particle image velocimetry and proper orthogonal decomposition to the study of a jet in a counterflow." *Experiments in Fluids* 29, S274-S281.

Blatchley, E.R., 1997. "Numerical modelling of UV intensity: Application to collimated-beam reactors and continuous-flow systems." *Water Research* 31(9), 2205-2218.

Blatchley, E.R., Do-Quang, Z., Janex, M.L. and Laine, J.M., 1998. "Process modeling of ultraviolet disinfection." *Water Science and Technology* 38(6), 63-69.

Blatchley, E.R., Shen, C.Y., Naunovic, Z., Lin, L.S., Lyn, D.A., Robinson, J.P., Ragheb, K., Gregori, G., Bergstrom, D.E., Fang, S.Y., Guan, Y.H., Jennings, K. and

Gunaratna, N., 2006. "Dyed microspheres for quantification of UV dose distributions: Photochemical reactor characterization by Lagrangian actinometry." *Journal of Environmental Engineering-Asce* 132(11), 1390-1403.

Blatchley III, E.R., Shen, C., Scheible, O.K., Robinson, J.P., Ragheb, K., Bergstrom, D.E. and Rokjer, D., 2008. "Validation of large-scale, monochromatic UV disinfection systems for drinking water using dyed microspheres." *Water Research* 42(3), 677-688.

Bohrerova, Z., Bohrer, G., Mohanraj, S.M., Ducoste, J. and Linden, K.G., 2005. "Experimental measurements of fluence distribution in a UV reactor using fluorescent microspheres." *Environmental Science & Technology* 39(22), 8925-8930.

Bolton, J.R., 2000. "Calculation of ultraviolet fluence rate distributions in an annular reactor: significance of refraction and reflection." *Water Research* 34(13), 3315-3324.

Bolton, J. R. and Linden, K. G., 2003. "Standardization of methods for fluence (UV dose) determination in bench-scale UV experiments." *Journal of American Water Works Association* 129 (3), 209-215.

Braza, M., Perrin, R. and Hoarau, Y., 2006. "Turbulence properties in the cylinder wake at high Reynolds numbers." *Journal of Fluids and Structures* 22 (6-7), 757-771.

Buxton, G.V., Greenstock, C.L., Helman, W.P. and Ross, A.B., 1988. "Critical-Review of Rate Constants for Reactions of Hydrated Electrons, Hydrogen-Atoms and Hydroxyl Radicals (.Oh/.O-) in Aqueous-Solution." *Journal of Physical and Chemical Reference Data* 17(2), 513-886.

Cabaj, A. and Sommer, R., 2000. "Measurement of ultraviolet radiation with biological dosemeters." *Radiation Protection Dosimetry* 91(1-3), 139-142.

Campbell, A.T. and Wallis, P., 2002. "The effect of UV irradiation on human-derived Giardia lamblia cysts." *Water Research* 36(4), 963-969.

Cantwell, B. and Coles, D., 1983. "An experimental-study of entrainment and transport in the turbulent near wake of a circular-cylinder." *Journal of Fluid Mechanics* 136(NOV), 321-374.

Chiu, K., Lyn, D.A., Savoye, P. and Blatchley, E.R., 1999. "Integrated UV disinfection model based on particle tracking." *Journal of Environmental Engineering-Asce* 125(1), 7-16.

Chiu, K.P., Lyn, D.A., Savoye, P. and Blatchley, E.R., 1999. "Effect of UV system modifications on disinfection performance." *Journal of Environmental Engineering-Asce* 125(5), 459-469.

Cho, M., Gandhi, V., Hwang, T.M., Lee, S. and Kim, J.H., 2011. "Investigating synergism during sequential inactivation of MS-2 phage and Bacillus subtilis spores with UV/H2O2 followed by free chlorine." *Water Research* 45(3), 1063-1070.

Clancy, J.L., Hargy, T.M., Marshall, M.M. and Dyksen, J.E., 1998. "UV light inactivation of Cryptosporidium oocysts." *Journal American Water Works Association* 90(9), 92-102.

Cortelyou, J.R., Mcwhinnie, M.A., Riddiford, M.S. and Semrad, J.E., 1954. "The effects of ultraviolet irradiation on large populations of certain water-borne bacteria in motion .2. Some physical factors affecting the effectiveness of germicidal ultraviolet irradiation." *Applied Microbiology* 2(5), 269-273.

Craun, G.F., Hubbs, S.A., Frost, F., Calderon, R.L. and Via, S.H., 1998. "Waterborne outbreaks of cryptosporidiosis." *Journal American Water Works Association* 90(9), 81-91.

Crittenden, J.C., Hu, S.M., Hand, D.W. and Green, S.A., 1999. "A kinetic model for H_2O_2/UV process in a completely mixed batch reactor." *Water Research* 33(10), 2315-2328.

Cruyningen, I., Lozano, A. and Hanson, R.K., 1990. "Quantitative imaging of concentration by planar laser-induced fluorescence." *Experiments in Fluids* 10(1), 41-49.

Cruz, A.S., David, L., Pecheux, J. and Texier, A., 2005. "Characterization by proper-orthogonal-decomposition of the passive controlled wake flow downstream of a half cylinder." *Experiments in Fluids* 39(4), 730-742.

Deane, A.E., Kevrekidis, I.G., Karniadakis, G.E. and Orszag, S.A., 1991. "Low-dimensional models for complex-geometry flows - application to grooved channels and circular-cylinders." *Physics of Fluids a-Fluid Dynamics* 3(10), 2337-2354.

Dipankar, A., Sengupta, T.K. and Talla, S.B., 2007. "Suppression of vortex shedding behind a circular cylinder by another control cylinder at low Reynolds numbers." *Journal of Fluid Mechanics* 573, 171-190.

Driedger, A.M.; Rennecker, J.L.; Mariñas, B.J. (2001a). "Inactivation of *Cryptosporidium parvum* oocysts with ozone and monochloramine at low temperature." *Water Research*, 35(1), 41-48.

Driedger, A.M.; Staub, E.; Pinkernell, U.; Mariñas, B.J., Köster, W.; von Gunten, U. (2001b) “Inactivation of *Bacillus subtilis* spores and formation of bromate during ozonation”, *Water Research,* 35(12), 2950-2960.

Ducoste, J., Linden, K., Rokjer, D. and Liu, D., 2005. "Assessment of reduction equivalent fluence bias using computational fluid dynamics." *Environmental Engineering Science* 22(5), 615-628.

Ducoste, J.J., Liu, D. and Linden, K., 2005. "Alternative approaches to modeling fluence distribution and microbial inactivation in ultraviolet reactors: Lagrangian versus Eulerian." *Journal of Environmental Engineering-Asce* 131(10), 1393-1403.

Durgesh, V., Semaan, R.C. and Naughton, J.W., "Revealing unsteady flow structure from flow visualization images." *European Physical Journal-Special Topics* 182(1), 35-50.

Dyksen, J.E., Marshall, M.M., Gera, A. and Clancy, J.L., 1998. "Cost of advanced UV for inactivating crypto." *Journal American Water Works Association* 90(9), 103-111.

Elyasi, S. and Taghipour, F., 2010. "Simulation of UV Photoreactor for Degradation of Chemical Contaminants: Model Development and Evaluation." *Environmental Science & Technology* 44(6), 2056-2063.

Elyasi, S. and Taghipour, F., 2011. "Performance Evaluation of UV Reactor Using Optical Diagnostic Techniques." *Aiche Journal* 57(1), 208-217.

Epps, B. and Techet, A., 2010. "An error threshold criterion for singular value decomposition modes extracted from PIV data." *Experiments in Fluids* 48(2), 355-367.

Feng, L.H., Wang, J.J. and Pan, C., 2011. "Proper orthogonal decomposition analysis of vortex dynamics of a circular cylinder under synthetic jet control." *Physics of Fluids* 23(1), 13.

Ferrier, A.J., Funk, D.R. and Roberts, P.J.W., 1993. "Application of Optical Techniques to the Study of Plumes in Stratified Fluids." *Dynamics of Atmospheres and Oceans* 20(1-2), 155-183.

Ferziger, J. H. and M. Perić. 2002. *Computational Methods for Fluid Dynamics.* Berlin: Springer-Verlag.

Fogleman, M., Lumley, J., Rempfer, D. and Haworth, D., 2004. "Application of the proper orthogonal decomposition to datasets of internal combustion engine flows." *Journal of Turbulence* 5.

Franke, R., Rodi, W. and Schonung, B., 1990. "Numerical-calculation of laminar vortex-shedding flow past cylinders." *Journal of Wind Engineering and Industrial Aerodynamics* 35(1-3), 237-257.

Gandhi, V., Roberts, P.J.W., Stoesser, T., Wright, H. and Kim, J.H., 2011. "UV reactor flow visualization and mixing quantification using three-dimensional laser-induced fluorescence." *Water Research* 45(13), 3855-3862.

Gerrard, J.H., 1966. "The mechanics of the vortex formation region of vortices behind bluff bodies." *Journal of Fluid Mechanics* 25, 401-413.

Glaze, W.H., Weinberg, H.S. and Cavanagh, J.E., 1993. "Evaluating the formation of brominated DBPs during ozonation." *Journal American Water Works Association* 85 (1), 96-103.

Gnirss, M. and Tropea, C., 2008. "Simultaneous PIV and concentration measurements in a gas-turbine combustor model." *Experiments in Fluids* 45(4), 643-656.

Graftieaux, L., Michard, M. and Grosjean, N., 2001. "Combining PIV, POD and vortex identification algorithms for the study of unsteady turbulent swirling flows." *Measurement Science & Technology* 12(9), 1422-1429.

Guiraud, P., Bertrand, J. and Costes, J., 1991. "Laser Measurements of Local Velocity and Concentration in a Turbulent Jet-Stirred Tubular Reactor." *Chemical Engineering Science* 46(5-6), 1289-1297.

Guiraud, P., Costes, J. and Bertrand, J., 1997. "Local measurements of fluid and particle velocities in a stirred suspension." *Chemical Engineering Journal* 68(2-3), 75-86.

Guiraud, P., Duquenne, A.M., Etcheto, L. and Bertrand, J., 1993. "Numerical-Simulation of in-Line Mixers." *Computers & Chemical Engineering* 17, S511-S516.

Gungor, E. and Roberts, P.J.W., 2009. "Experimental Studies on Vertical Dense Jets in a Flowing Current." *Journal of Hydraulic Engineering-Asce* 135(11), 935-948.

Gurka, R., Liberzon, A. and Hetsroni, G., 2006. "POD of vorticity fields: A method for spatial characterization of coherent structures." *International Journal of Heat and Fluid Flow* 27(3), 416-423.

Gyürék, L.; Finch, G.R.; Belosevic M., 1997. "Modeling chlorine inactivation requirements of *Cryptosporidium parvum* oocysts." *ASCE Journal of Environmental Engineering*, 123(9), 865-875.

Hancock, C.M., Rose, J.B. and Callahan, M., 1998. "Crypto and Giardia in US groundwater." *Journal American Water Works Association* 90(3), 58-61.

Hirota, M., Nakayama, H., Koide, S. and Takeuchi, I., 2008. "Experimental Study on Turbulent Flow and Mixing in Counter-Flow Type T-Junction." *Journal of Thermal Science and Technology* 3(1), 147-158.

Ho, C.F.H., Pitt, P., Mamais, D., Chiu, C. and Jolis, D., 1998. "Evaluation of UV disinfection systems for large-scale secondary effluent." *Water Environment Research* 70(6), 1142-1150.

Huffman, D.E., Slifko, T.R., Salisbury, K. and Rose, J.B., 2000. "Inactivation of bacteria, virus and Cryptosporidium by a point-of-use device using pulsed broad spectrum white light." *Water Research* 34(9), 2491-2498.

Hunt, J.P. and Taube, H., 1952. "The photochemical decomposition of hydrogen peroxide - quantum yields, tracer and fractionation effects." *Journal of the American Chemical Society* 74(23), 5999-6002.

Hussain, A.K.M.F., 1983. "Coherent structures---reality and myth." *Physics of Fluids* 26(10), 2816-2850.

Hussain, A.K.M.F., 1986. "Coherent structures and turbulence." *Journal of Fluid Mechanics* 173, 303-356.

Jacob, S.M. and Dranoff, J.S., 1970. "Light intensity profiles in a perfectly mixed photoreactor." *Aiche Journal* 16(3), 359-&.

Jagger, J. 1967. *Introduction to Research in Ultraviolet Photobiology*. Englewood Cliffs, NJ: Prentice-Hall, Inc.

Janex, M.L., Savoye, P., Do-Quang, Z., Blatchley, E. and Laine, J.M., 1998. "Impact of water quality and reactor hydrodynamics on wastewater disinfection by UV, use of CFD modeling for performance optimization." *Water Science and Technology* 38(6), 71-78.

Kim, D., Nemlioglu, S., Roberts, P.J.W. and Kim, J.H., 2010. "Ozone-contactor flow visualization and quantification using three-dimensional laser-induced fluorescence." *Journal American Water Works Association* 102 (1), 90-99.

Konstantinidis, E., Balabani, S. and Yianneskis, M., 2007. "Bimodal vortex shedding in a perturbed cylinder wake." *Physics of Fluids* 19(1).

Koochesfahani, M.M. and Dimotakis, P.E., 1985. "Laser-induced fluorescence measurements of mixed fluid concentration in a liquid plane shear-layer." *Aiaa Journal* 23(11), 1700-1707.

Kostas, J., Soria, J. and Chong, M., 2005. "A comparison between snapshot POD analysis of PIV velocity and vorticity data." *Experiments in Fluids* 38(2), 146-160.

Kostas, J., Soria, J. and Chong, M.S., 2002. "Particle image velocimetry measurements of a backward-facing step flow." *Experiments in Fluids* 33(6), 838-853.

Krasner, S.W., Weinberg, H.S., Richardson, S.D., Pastor, S.J., Chinn, R., Sclimenti, M.J., Onstad, G.D. and Thruston, A.D., 2006. "Occurrence of a New Generation of Disinfection Byproducts†." *Environmental Science & Technology* 40(23), 7175-7185.

Krasner, S.W., Westerhoff, P., Chen, B., Rittmann, B.E. and Amy, G., 2009. "Occurrence of Disinfection Byproducts in United States Wastewater Treatment Plant Effluents." *Environmental Science & Technology* 43(21), 8320-8325.

Kurokawa, Y., Hayashi, Y., Maekawa, A., Takahashi, M., Kokubo, T. and Odashima, S., 1983. "Carcinogenicity of potassium bromate administered orally to F344 rats." *J Natl Cancer Inst* 71(5), 965-972.

Kurokawa, Y., Maekawa, A., Takahashi, M. and Hayashi, Y., 1990. "Toxicity and carcinogenicity of potassium bromate--a new renal carcinogen." *Environ Health Perspect* 87, 309-335.

Lawryshyn, Y.A. and Cairns, B., 2003. "UV disinfection of water: the need for UV reactor validation." *Water Science and Technology: Water Supply* 3(4), 293-300.

Linden, K.G., Shin, G. and Sobsey, M.D., 2001. "Comparative effectiveness of UV wavelengths for the inactivation of Cryptosporidium parvum oocysts in water." *Water Science and Technology* 43(12), 171-174.

Linden, K.G., Shin, G.A., Faubert, G., Cairns, W. and Sobsey, M.D., 2002. "UV disinfection of Giardia lamblia cysts in water." *Environmental Science & Technology* 36 (11), 2519-2522.

Lisle, J.T. and Rose, J.B., 1995. "*Cryptosporidium* contamination of water in the USA and UK - a mini-review." *Journal of Water Supply Research and Technology-Aqua* 44(3), 103-117.

Liu, D., Ducoste, J., Jin, S. and Linden, K., 2004. "Evaluation of alternative fluence rate distribution models." *Journal of Water Supply Research and Technology-Aqua* 53(6), 391-408.

Liu, D., Wu, C., Linden, K. and Ducoste, J., 2007. "Numerical simulation of UV disinfection reactors: Evaluation of alternative turbulence models." *Applied Mathematical Modelling* 31 (9), 1753-1769.

Liu, Z., Adrian, R.J. and Hanratty, T.J., 2001. "Large-scale modes of turbulent channel flow: transport and structure." *Journal of Fluid Mechanics* 448, 53-80.

Lyn, D.A., 2004. "Steady and unsteady simulations of turbulent flow and transport in ultraviolet disinfection channels." *Journal of Hydraulic Engineering-Asce* 130(8), 762-770.

Lyn, D.A. and Blatchley, E.R., 2005. "Numerical computational fluid dynamics-based models of ultraviolet disinfection channels." *Journal of Environmental Engineering-Asce* 131(6), 838-849.

Lyn, D.A., Chiu, K. and Blatchley, E.R., 1999. "Numerical modeling of flow and disinfection in UV disinfection channels." *Journal of Environmental Engineering-Asce* 125(1), 17-26.

Ma, X., Karamanos, C.S. and Karniadakis, G.E., 2000. "Dynamics and low-dimensionality of a turbulent near wake." *Journal of Fluid Mechanics* 410, 29-65.

Ma, X., Karniadakis, G.E., Park, H. and Gharib, M., 2003. "DPIV-driven flow simulation: a new computational paradigm." *Proceedings of the Royal Society of London Series a-Mathematical Physical and Engineering Sciences* 459(2031), 547-565.

March, J., 1985. *Advanced Organic Chemistry*. John Wiley & Sons, Inc., New York, 3rd edition.

Meyer-Arendt J. R., 1984. *Introduction to Classical and Modern Optics*, 2nd ed. Prentice-Hall, Englewood Cliffs, NJ, pp. 300 – 302.

Meyer, K.E.E., Pedersen, J.M. and Ozcan, O., 2007. "A turbulent jet in crossflow analysed with proper orthogonal decomposition." *Journal of Fluid Mechanics* 583, 199-227.

Meulemans, C.C.E. 1986. The basic principles of UV-sterilization of water. In: *Ozone Ultraviolet Water Treatment*, Aquatec Amsterdam, Paris: International Ozone Association. B.1.1 – B.1.13.

Moin, P. and Moser, R.D., 1989. "Characteristic-eddy decomposition of turbulence in a channel." *Journal of Fluid Mechanics* 200, 471-509.

Moreira, R.M., Pinto, A.M.F., Mesnier, R. and Leclerc, J.P., 2007. "Influence of inlet positions on the flow behavior inside a photoreactor using radiotracers and colored tracer investigations." *Applied Radiation and Isotopes* 65(4), 419-427.

Morkovin, M.V., 1964. "Flow around a circular cylinder-kaleidoscope of challenging fluid phenomena." *Proceedings in ASME Symposium Fully Separated Flows*, p. 102.

Nakayama, A., Yano, Y., Kobayashi, S., Ishikawa, M. and Sakai, K., 1996. "Comparison of pressure resistances of spores of six Bacillus strains with their heat resistances." *Applied and Environmental Microbiology* 62(10), 3897-3900.

Noack, B.R., Afanasiev, K., Morzynski, M., Tadmor, G. and Thiele, F., 2003. "A hierarchy of low-dimensional models for the transient and post-transient cylinder wake." *Journal of Fluid Mechanics* 497, 335-363.

Oertel, H., 1990. "Wakes behind blunt bodies." *Annual Reviews in Fluid Mechanics* 22, 539-562.

Ono, Y., Somiya, I. and Mohri, S., 1994. "Evaluation of genotoxicity of bromate ion produced during ozonation." *Ozone-Science & Engineering* 16(5), 443-453.

Oppenheimer, J.A., Jacangelo, J.G., Laine, J.M. and Hoagland, J.E., 1997. "Testing the equivalency of ultraviolet light and chlorine for disinfection of wastewater to reclamation standards." *Water Environment Research* 69(1), 14-24.

Patte-Rouland, B., Lalizel, G., Moreau, J. and Rouland, E., 2001. "Flow analysis of an annular jet by particle image velocimetry and proper orthogonal decomposition." *Measurement Science & Technology* 12(9), 1404-1412.

Pedersen, J.M. and Meyer, K.E., 2002. "POD analysis of flow structures in a scale model of a ventilated room." *Experiments in Fluids* 33(6), 940-949.

Perrin, R., Braza, M., Cid, E., Cazin, S., Barthet, A., Sevrain, A., Mockett, C. and Thiele, F., 2007. "Obtaining phase averaged turbulence properties in the near wake of a circular cylinder at high Reynolds number using POD." *Experiments in Fluids* 43(2-3), 341-355.

Perry, A.E., Chong, M.S., and Lim, T.T., 1982. "The vortex shedding process behind two-dimensional bluff bodies." *Journal of Fluid Mechanics* 116, 77-90.

Phibbs, M. K.; Giguere, P. A., 1951. "Hydrogen peroxide and its analogues. III. Absorption spectrum of hydrogen and deuterium peroxides in the near ultraviolet." *Canadian Journal of Chemistry* 29 (6), 490-493.

Prasad, R.R. and Sreenivasan, K.R., 1990. "Quantitative 3-Dimensional Imaging and the Structure of Passive Scalar Fields in Fully Turbulent Flows." *Journal of Fluid Mechanics* 216, 1-34.

Price, S.J., Sumner, D., Smith, J.G., Leong, K. and Paidoussis, M.P., 2002. "Flow visualization around a circular cylinder near to a plane wall." *Journal of Fluids and Structures* 16 (2), 175-191.

Qualls, R.G., Dorfman, M.H. and Johnson, J.D., 1989. "Evaluation of the Efficiency of Ultraviolet Disinfection Systems." *Water Research* 23(3), 317-325.

Qualls, R.G. and Johnson, J.D., 1983. "Bioassay and dose measurement in UV disinfection." *Appl. Environ. Microbiol.* 45(3), 872-877.

Qualls, R.G. and Johnson, J.D., 1985. "Modeling and efficiency of ultraviolet disinfection systems." *Water Research* 19(8), 1039-1046.

Raffel, M., Willert, C.E., Wereley, S.T. and Kompenhans J., 2007. *Particle image velocimetry: a practical guide.* Springer, New York.

Rehimi, F., Aloui, F., Ben Nasrallah, S., Doubliez, L. and Legrand, J., 2008. "Experimental investigation of a confined flow downstream of a circular cylinder centred between two parallel walls." *Journal of Fluids and Structures* 24 (6), 855-882.

Rennecker, J.L., Driedger, A.M., Rubin, S.A. and Mariñas, B.J., 2000. "Synergy in Sequential Inactivation of *Cryptosporidium parvum* with Ozone/Free Chlorine and Ozone/Monochloramine." *Water Research*, 34(17), 4121-4130

Roberts, P.J.W., 1979. "Line plume and ocean outfall dispersion." *Journal of the Hydraulics Division-Asce* 105(4), 313-331.

Roberts, P.J.W., Maile, K. and Daviero, G., 2001. "Mixing in stratified jets." *Journal of Hydraulic Engineering-Asce* 127(3), 194-200.

Roberts, P.J.W. and Snyder, W.H., 1993. "Hydraulic model study for Boston outfall .1. Riser configuration." *Journal of Hydraulic Engineering-Asce* 119(9), 970-987.

Roberts, P.J.W., Snyder, W.H. and Baumgartner, D.J., 1989. "Ocean outfalls .1. Submerged wastefield formation." *Journal of Hydraulic Engineering-Asce* 115(1), 1-25.

Roberts, P.J.W. and Tian, X.D., 2004. "New experimental techniques for validation of marine discharge models." *Environmental Modelling & Software* 19(7-8), 691-699.

Robinson, S.K., 1991. "Coherent Motions in the Turbulent Boundary Layer." *Annual Review of Fluid Mechanics* 23(1), 601-639.

Rosenfeldt, E.J. and Linden, K.G., 2004. "Degradation of endocrine disrupting chemicals bisphenol A, ethinyl estradiol, and estradiol during UV photolysis and advanced oxidation processes." *Environmental Science & Technology* 38(20), 5476-5483.

Rosenfeldt, E.J., Melcher, B. and Linden, K.G., 2005. "UV and UV/H2O2 treatment of methylisoborneol (MIB) and geosmin in water." *Journal of Water Supply Research*

and Technology-Aqua 54(7), 423-434.

Rosenhead, L., 1953. “Vortex systems in wakes.” *Advances in Applied Mechanics* 3, 185-195.

Roshko, A., 1954. “On the development of turbulent wakes from vortex streets.” *National Advisory Committee for Aeronautics*, Washington, D.C.

Ruan, X., Song, X. and Yamamoto, F., 2001. "Direct measurement of the vorticity field in digital particle images." *Experiments in Fluids* 30(6), 696-704.

Sakamoto, H. and Haniu, H., 1990. "A study on vortex shedding from spheres in a uniform-flow." *Journal of Fluids Engineering-Transactions of the Asme* 112(4), 386-392.

Santoro, D., Raisee, M., Moghaddami, M., Ducoste, J., Sasges, M., Liberti, L. and Notarnicola, M., 2010. "Modeling Hydroxyl Radical Distribution and Trialkyl Phosphates Oxidation in UV-H_2O_2 Photoreactors Using Computational Fluid Dynamics." *Environmental Science & Technology* 44(16), 6233-6241.

Sarkar, S. and Sarkar, S., 2010. “Vortex dynamics of a cylinder wake in proximity to a wall.” *Journals of Fluids and Structures* 26, 19-40.

Sasges, M. R., van der Pol, A., Voronov, A. and Robinson, J., 2007. “A Standard Method for Quantifying the Output of UV Lamps.” In *International Ozone Association Joint Congress*, International UV Association.

Savoye, P., Janex, M.L. and Lazarova, V., 2001. "Wastewater disinfection by low-pressure UV and ozone: a design approach based on water quality." *Water Science and Technology* 43(10), 163-171.

Scheible O. K., Casey M. C. and Forndran A. (1985) “Ultraviolet disinfection of wastewaters from secondary effluent and combined sewer overflows.” Report No. EPA/600/2-86/005. *US Environmental Protection Agency*, National Technical Information Service, Springfield, VA.

Schulz, C.R. and Bellamy, W.D., 2000. "The role of mixing in ozone dissolution systems." *Ozone-Science & Engineering* 22(4), 329-350.

Severin, B.F., Suidan, M.T. and Engelbrecht, R.S., 1983. "Kinetic modeling of U.V. disinfection of water." *Water Research* 17(11), 1669-1678.

Sharpless, C.M. and Linden, K.G., 2001. "DV photolysis of nitrate: Effects of natural organic matter and dissolved inorganic carbon and implications for UV water disinfection." *Environmental Science & Technology* 35(14), 2949-2955.

Shen, C.Y., Fang, S.Y., Bergstrom, D.E. and Blatchley, E.R., 2005. "(E)-5-[2-(Methoxycarbonyl)ethenyl]-cytidine as a chemical actinometer for germicidal UV radiation." *Environmental Science & Technology* 39(10), 3826-3832.

Shi, L.L., Liu, Y.Z. and Wan, J.J., 2010. "Influence of wall proximity on characteristics of wake behind a square cylinder: PIV measurements and POD analysis." *Experimental Thermal and Fluid Science* 34(1), 28-36.

Shin, G.A., Linden, K.G., Arrowood, M.J. and Sobsey, M.D., 2001. "Low-pressure UV inactivation and DNA repair potential of Cryptosporidium parvum oocysts." *Applied and Environmental Microbiology* 67(7), 3029-3032.

Shin, G.A. and Sobsey, M.D., 2008. "Inactivation of norovirus by chlorine disinfection of water." *Water Research* 42(17), 4562-4568.

Singha, S. and Sinhamahapatra, K.P., 2010. Flow past a circular cylinder between parallel walls at low Reynolds numbers. Ocean Engineering 37 (8-9), 757-769.

Singha, A., Shinneeb, A.M. and Balachandar, R., 2009. "PIV-POD Investigation of the Wake of a Sharp-Edged Flat Bluff Body Immersed in a Shallow Channel Flow." *Journal of Fluids Engineering-Transactions of the Asme* 131(2), 12.

Sirovich, L., 1987. "Turbulence and the dynamics of coherent structures .1. Coherent structures." *Quarterly of Applied Mathematics* 45(3), 561-571.

Sirovich, L., Ball, K.S. and Keefe, L.R., 1990. "Plane-waves and structures in turbulent channel flow." *Physics of Fluids a-Fluid Dynamics* 2(12), 2217-2226.

Snyder, S.A., Wert, E.C., Lei, H., Westerhoff, P. and Yoon, Y., 2007. *Removal of ECDs and Pharmaceuticals in Drinking and Reuse Treatment Processes*, Water Research Foundation, Denver, CO

Sommer, R., Cabaj, A. and Haider, T., 1996. "Microbicidal effect of reflected UV radiation in devices for water disinfection." *Water Science and Technology* 34(7-8), 173-177.

Sommer, R., Cabaj, A., Pribil, W. and Haider, T., 1997. "Influence of lamp intensity and water transmittance on the UV disinfection of water." *Water Science and Technology* 35(11-12), 113-118.

Sozzi, D.A. and Taghipour, F., 2005. "Experimental investigation of flow field in annular ultraviolet reactors using particle image velocimetry (PIV)." *Industrial & Engineering Chemistry Research* 44(26), 9979-9988.

Sozzi, D.A. and Taghipour, F., 2006. "Computational and experimental study of annular photo-reactor hydrodynamics." *International Journal of Heat and Fluid Flow* 27(6), 1043-1053.

Sozzi, D.A. and Taghipour, F., 2006. "UV reactor performance modeling by Eulerian and Lagrangian methods." *Environmental Science & Technology* 40(5), 1609-1615.

Strouhal, V, 1878. "Uber eine besondere Art der Tonerregung." *Annals of Physics* 241(10), 216-251.

Suidan, M.T. and Severin, B.F., 1986. "Light-intensity models for annular UV disinfection reactors." *Aiche Journal* 32(11), 1902-1909.

Taghipour, F. and Sozzi, A., 2005. "Modeling and design of ultraviolet reactors for disinfection by-product precursor removal." *Desalination* 176(1-3), 71-80.

Tang, G., Adu-Sarkodie, K., Kim, D., Kim, J.H., Teefy, S., Shukairy, H.M. and Marinas, B.J., 2005. "Modeling Cryptosporidium parvum oocyst inactivation and bromate formation in a full-scale ozone contactor." *Environmental Science & Technology* 39(23), 9343-9350.

Tian X.D., 2003. "3DLIF and its applications to studies of the near filed mixing in wastewater discharges." Dissertation, *Georgia Institute of Technology*.

Tian, X.D. and Roberts, P.J.W., 2003. "A 3D LIF system for turbulent buoyant jet flows." *Experiments in Fluids* 35(6), 636-647.

Tian, X.D. and Roberts, P.J.W., 2008. "Mixing in Water Storage Tanks. I: No Buoyancy Effects." *Journal of Environmental Engineering-Asce* 134(12), 974-985.

Tian, X.D. and Roberts, P.J.W., 2008. "Mixing in Water Storage Tanks. II: With Buoyancy Effects." *Journal of Environmental Engineering-Asce* 134(12), 986-995.

Tian, X.D., Roberts, P.J.W. and Daviero, G.J., 2004. "Marine wastewater discharges from multiport diffusers. I: Unstratified stationary water." *Journal of Hydraulic Engineering-Asce* 130(12), 1137-1146.

Tian, X.D., Roberts, P.J.W. and Daviero, G.J., 2004. "Marine wastewater discharges from multiport diffusers. II: Unstratified flowing water." *Journal of Hydraulic Engineering-Asce* 130(12), 1147-1155.

Vancruyningen, I., Lozano, A. and Hanson, R.K., 1990. "Quantitative imaging of concentration by planar laser-induced fluorescence." *Experiments in Fluids* 10(1), 41-49.

Venturi, D., 2006. "On proper orthogonal decomposition of randomly perturbed fields with applications to flow past a cylinder and natural convection over a horizontal plate." *Journal of Fluid Mechanics* 559, 215-254.

Versteeg, H.K. and W. Malalasekera. 2007. *An Introduction to Computational Fluid Dynamics: The Finite Volume Method*. Upper Saddle River: Prentice Hall.

Volman, D.H. and Chen, J.C., 1959. "The photochemical decomposition of hydrogen peroxide in aqueous solutions of allyl alcohol at 2537-A." *Journal of the American Chemical Society* 81(16), 4141-4144.

Walker , D. A., 1987. "A fluorescence technique for measurement of concentration in mixing fluids." J. Phys. E: Sci. Instrum., 20, 217 – 224.

Water Environment Federation, 1996. *Wastewater Disinfection Manual of Practice FD-10*, Alexandria, VA.

Webster, D.R., Roberts, P.J.W. and Ra'ad, L., 2001. "Simultaneous DPTV/PLIF measurements of a turbulent jet." *Experiments in Fluids* 30(1), 65-72.

Wille, R., 1960. "Karman vortex streets." Advances in Applied Mechanics 6, 273-287.

Williamson, C.H.K., 1996. "Vortex dynamics in the cylinder wake." *Annual Review of Fluid Mechanics* 28 477-539.

Wols, B.A., Hofman, J.A.M.H., Beerendonk, E.F., Uijttewaal, W.S.J. and van Dijk, J.C., 2011. "A systematic approach for the design of UV reactors using computational fluid dynamics." *Aiche Journal* 57(1), 193-207.

Wols, B.A., Shao, L., Uijttewaal, W.S.J., Hofman, J.A.M.H., Rietveld, L.C. and van Dijk, J.C., 2010a. "Evaluation of experimental techniques to validate numerical computations of the hydraulics inside a UV bench-scale reactor." *Chemical Engineering Science* 65(15), 4491-4502.

Wols, B.A., Uijttewaal, W.S.J., Hofman, J.A.M.H., Rietveld, L.C. and van Dijk, J.C., 2010b. "The weaknesses of a k–ε model compared to a large-eddy simulation for the prediction of UV dose distributions and disinfection." *Chemical Engineering Journal* 162(2), 528-536.

Wright, S.J., 1977. "Mean behavior of buoyant jets in a crossflow." *Journal of the Hydraulics Division*, Vol. 103(HY5), 499-513.

Wright, H.B. and Lawryshyn, Y.A., 2000. "An assessment of the bioassay concept for UV reactor validation." *Proc. Wat. Env. Specialty Conf. on Disinfection*, New Orleans, Louisiana, USA, 15–18 March.

USEPA, 2006. Ultraviolet Disinfection Guidance Manual for the Final Long Term 2

Enhanced Surface Water Treatment Rule. United States Environmental Protection Agency EPA 815-R-06-007.

Younis, B.A. and Yang, T.H., 2011. "Prediction of the effects of vortex shedding on UV disinfection efficiency." *Journal of Water Supply Research and Technology-Aqua* 60(3), 147-158.

Younis, B.A. and Yang, T.H., 2010. "Computational modeling of ultraviolet disinfection." *Water Science and Technology* 62(8), 1872-1878.

Zdravkovich, M. M. 1997. *Flow around circular cylinders Vol 1: Fundamentals*. New York: Oxford Science Publications.

Zhao, X., Alpert, S.M. and Ducoste, J.J., 2009. "Assessing the Impact of Upstream Hydraulics on the Dose Distribution of Ultraviolet Reactors Using Fluorescence Microspheres and Computational Fluid Dynamics." *Environmental Engineering Science* 26(5), 947-959.

VITA

Varun Gandhi was born in Umm al-Quwain, United Arab Emirates, on November 28, 1985. He received his B.S. degree in Civil Engineering with a focus in Environmental and his M.S. degrees in Environmental Engineering from the Department of Civil and Environmental Engineering at Georgia Institute of Technology, Atlanta, GA, in 2007 and 2011, respectively. He worked as an intern at Brown and Caldwell, Atlanta, GA in summer 2007, between his B.S. and M.S. degrees. Beginning in the fall of 2007, Varun became a graduate research assistant in the Department of Civil and Environmental Engineering at Georgia Institute of Technology. His research was focused on the development of a technique using LIF to analyze and optimize ultraviolet reactors used in disinfection of drinking water.